AWARD NUMBER: W81XWH-13-1-0151

TITLE: Nano-siRNA Particles and Combination Therapies for Ovarian Tumor Targeting

PRINCIPAL INVESTIGATOR: Paula T. Hammond

CONTRACTING ORGANIZATION: Massachusetts Institute of Technology
Cambridge, MA 02139

REPORT DATE: August 2014

TYPE OF REPORT: Annual

PREPARED FOR: U.S. Army Medical Research and Materiel Command
Fort Detrick, Maryland 21702-5012

REPORT DOCUMENTATION PAGE

Form Approved
OMB No. 0704-0188

1. REPORT DATE	2. REPORT TYPE	3. DATES COVERED
August 2014	Annual	7/22/13-7/21/14

4. TITLE AND SUBTITLE
Nano-siRNA Particles and Combination Therapies for Ovarian Tumor Targeting

5a. CONTRACT NUMBER

5b. GRANT NUMBER
W81XWH-13-0151

5c. PROGRAM ELEMENT NUMBER

6. AUTHOR(S)
Paula T. Hammond

E-Mail: Hammond@mit.edu

5d. PROJECT NUMBER

5e. TASK NUMBER

5f. WORK UNIT NUMBER

7. PERFORMING ORGANIZATION NAME(S) AND ADDRESS(ES)
Massachusetts Institute of Technology
Cambridge, MA 02139

8. PERFORMING ORGANIZATION REPORT NUMBER

9. SPONSORING / MONITORING AGENCY NAME(S) AND ADDRESS(ES)
U.S. Army Medical Research and Materiel Command
Fort Detrick, Maryland 21702-5012

10. SPONSOR/MONITOR'S ACRONYM(S)

11. SPONSOR/MONITOR'S REPORT NUMBER(S)

12. DISTRIBUTION / AVAILABILITY STATEMENT
Approved for Public Release; Distribution Unlimited

13. SUPPLEMENTARY NOTES

14. ABSTRACT

See Next Page

15. SUBJECT TERMS None Provided

16. SECURITY CLASSIFICATION OF:			17. LIMITATION OF ABSTRACT	18. NUMBER OF PAGES	19a. NAME OF RESPONSIBLE PERSON
a. REPORT	b. ABSTRACT	c. THIS PAGE			USAMRMC
U	U	U	UU	101	19b. TELEPHONE NUMBER *(include area code)*

ABSTRACT

New therapies based on RNA interference (RNAi) show promise for the treatment of ovarian cancer, however, the packaging and delivery of these medicines to tumor sites remains a challenge that has hindered their clinical use. We have been developing new strategies to generate and assemble nanoparticles for RNAi-based therapy with enhanced stability to improve tumor delivery. Using a unique method for making RNA called rolling circle transcription, we have generated novel siRNA-containing structures. These RNA structures consist of long, repeating siRNA sequences termed concatemeric siRNA (csiRNA) along with sponge-like particles that contain both RNA and inorganic nanocrystals. By combining these materials with different polymers we obtain stable nanoparticles that show prolonged blood circulation, accumulate in tumors, and can silence gene expression in cancer cells. Our current work investigates the use of these nanoparticles to target genes that have been implicated in the progression of ovarian cancer. We have demonstrated the ability to incorporate sequences for more than one siRNA, thus enabling knockdown of multiple genes using the same construct, and we are now investigating efficacy in vitro and in vivo against oncogenic targets in ovarian cancer. New approaches to combination therapy that we are developing use the strategy of staged release of two or more chemotherapeutics from a singular targeted nanoparticle, preceded by the release of siRNA that knocks down genes enabling resistance to the chemotherapy agents. This is accomplished by building a nanoparticle layer-by-layer, starting with a core that contains a chemotherapy drug relevant to ovarian cancer, such as cisplatin; then a second therapeutic is introduced in the outer layers of the particle such as an inhibitor that can lower or impede the function of tumor cells, or siRNA molecules that can turn off a survival gene used by resistant tumor cell types to avoid attack by chemotherapy treatment. We have been partnering with clinicians and scientists at Dana-Farber Cancer Institute and at the Massachusetts General Hospital to identify, determine and implement combinations key to ovarian cancer in these unique nanoparticle platforms. Ovarian cancers, particularly those of the high-grade serous subtype (96%), are characterized by mutations in the gene encoding the tumor suppressor protein, p53. In a recent collaboration at the Koch Institute at MIT, we identified a novel downstream signal effector in a MAPK stress response pathway – activated in response to platinum chemotherapy – whose loss is synthetically lethal in ovarian cancer cells that lack functional p53. To exploit this new vulnerability, we've engineered a series of lipid-like peptide co-polymers that self-assemble into nanoscale drug carriers that efficiently package and deliver small interfering RNA (siRNA) and platinum chemotherapeutics specifically to ovarian cancer cells.

Table of Contents

Page

Nano-siRNA Particles and Combination Therapies for Ovarian Tumor Targeting
OCRP Teal Innovator Statement of Work

PI: Paula T. Hammond, Department of Chemical Engineering
Koch Institute of Integrative Cancer Research
Massachusetts Institute of Technology

INTRODUCTION:

One of the key issues in epithelial ovarian cancer is the low clinical response to chemotherapy, and the high drug resistance found in the majority of patients who experience relapse[1,2]. These issues can be addressed with intelligent approaches to combination therapies that address the molecular pathways involved in drug resistance using gene regulation; siRNA is a particularly promising approach that has not yet reached clinical translation due to issues of delivery. Challenges include the ability to effectively condense, encapsulate and protect small charged nucleic acids, and the need to gain highly selective molecular targeting[3]. We propose new modular polymer systems that can generate targeted siRNA in a new stable and highly potent form using safe polymeric systems in place of viruses, which are known to yield undesirable side-effects. Key to these nanomaterial systems is the ability to "program-in" to a single delivery system specific combinations of chemotherapy drugs with siRNA and molecular inhibitors shown to be effective in ovarian cancer, thus providing the opportunity for highly synergistic couplings of therapeutics delivered in a safe and effective manner. This goal will be accomplished using the biologically intuitive design of nanoparticles using three key innovations, which are examined in Specific Aims 1 through 3:

1) The use of a new and highly effective means of RNAi polymerization and self-assembly to load high quantities of microRNA or siRNA sequences specifically targeting pathways to cell drug resistance[4-6] into condensed nanoparticles in a form that protects the siRNA from degradation, and releases it to the cell in high yield;

2) The design of "sheddable layers" on nanoparticle surfaces for synergistic combination drug therapy using modular chemical linkages to enable the tumor microenvironment pH or other tumor cell-triggered sequential release of siRNA, followed by inhibitors and chemotherapy drugs from the nanoparticles;

3) The presentation of ligand on nanoparticle surfaces in cluster arrangements that enable optimization of ligand presentation at low overall ligand levels and maximized tumor cell selectivity.

These concepts can be integrated to generate highly functional LbL nanoparticle systems specifically tuned to release drug in the ovarian tumor microenvironment, and designed with therapeutic combinations selected to address the challenges of ovarian cancer inhibition and drug resistance.

KEYWORDS: siRNA delivery, targeted nanoparticle, combination therapy, self-assembly, cancer nanotechnology,

OVERALL PROJECT SUMMARY:

Specific Aim 1: Self-packaging siRNA

Aim 1 Current Objectives: To address the barriers of RNA delivery, we have reported for the first time the polymerization of RNAi sequences in a form that folds into its own pre-packaged structure for delivery[7]. We use a means of synthesizing polymeric siRNA termed rolling circle

transcription (RCT) with a polymerase to yield large macromolecular species that consist of RNAi targeting sequences separated by RNA sequences that are rapidly cleaved by Dicer molecules in the cytosol (see Figure 1a). These RNA structures consist of long, repeating siRNA sequences, termed concatemeric siRNA (csiRNA), contained within self-assembled sponge-like particles templated from inorganic nanocrystals, or isolated in polymeric form. By combining these materials with different polymers we obtain stable nanoparticles that show prolonged blood circulation, accumulate in tumors, and can silence gene expression in cancer cells. The sponge-like microporous particles we refer to as RNAi microsponges (RNAi MS) each contain many thousands of copies of siRNA in a single unit (see Figure 1b). When a layer of a polycation is adsorbed onto the RNAi microsponges, they are compacted to positively charged nanoparticles that can deliver up to orders of magnitude higher amounts of siRNA than a traditional commercial lipid-based cationic vehicle (Figure 1c). The RNAi can also be removed from the microsponge template and isolated; these large chain concatenated siRNA (csiRNA) can be assembled with block copolymers or other polymeric complexes to also derive unique RNAi carrier systems in which the siRNA is preserved in a more stable form, and may exhibit modified biodistribution that can be favorable to tumor accumulation and sustained transfection within tumors. We hypothesize that each of these resulting self-assembled systems enable the delivery of a much higher amount of siRNA using a significantly lowered dose, thus improving siRNA knock-down efficacy while greatly increasing safety.

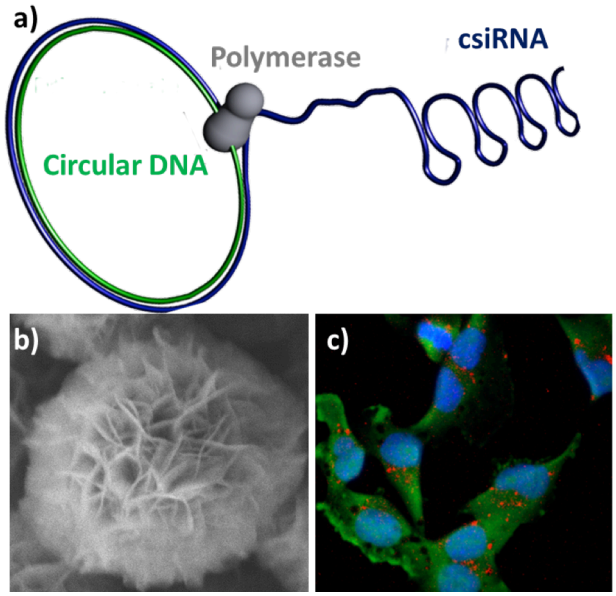

Figure 1. Novel approaches for delivering siRNA to ovarian cancer cells. (a) Cartoon representing the rolling circle transcription method for making concatemeric siRNA (csiRNA). (b) Scanning electron micrograph of an RNA microsponge particle formed during the rolling circle transcription reaction (particle is ~ 2 μm). (c) Confocal fluorescence microscope image showing ovarian cancer cells that have taken up RNA-containing nanoparticles (red).

The use of key discovered genetic targets for ovarian cancer (OC) will be coupled with this powerful new delivery platform through collaborations with Dr. Michael Birrer, M.D., PhD, who has participated in large scale studies of genome expression in ovarian cancer that have identified key genetic subgroups associated with high grade serous tumors[8], including those characteristic of drug resistant phenotypes of recurrent ovarian cancer. Two or more specific siRNA or micro-RNA sequences that silence or regulate these genes will be selected and incorporated into the RNAi microsponge (RNAi MS) to address resistant tumors. Because the sponge platform can be designed to incorporate 2, 3 or more siRNA sequences, unique combinations of siRNA will also be explored. Our efforts investigate the use of these nanoparticles to target genes that have been implicated in the progression of ovarian cancer, including MAGP2 and FGF18. We have selected FGF18 in place of previously considered IKKβ, as the FGF18 gene is now viewed by our collaborator, Dr. Michael Birrer, as the more promising target for oncological effect and possible synergy with MAGP2; however, in future work we may also explore or other pathways that may prove effective oncological targets based on our earlier results and any new information about ovarian cancer genetic pathways.

Aim 1 Results, Progress, and Accomplishments with Discussion:

1.1 Develop and test single target/component RNAi MS for OC.

We chose MAGP2 sequences for single genetic target evaluation in OC. New RNAi MS was successfully designed and synthesized for targeting MAGP2 in OC. The cellular uptake of RNAi MS for MAGP2 target was tested on three different OC cell lines including CAOV3, UCI101, and OVCAR8 with the varied RNAi MS concentrations and different types of outer layering polymers (*e.g.*, PEI, PLL, PLA). The transfection of these systems will be confirmed *in vitro* and quantified using qRT-PCR prior to moving on to *in vivo* testing. Control experiments will be carried out with single component RNAi-MS systems and traditional transfection reagents such as lipofectamine.

Size tuning of nanoparticles: Several studies have demonstrated the importance of size in the tumor accumulation of nanoparticles. It is critical to achieve the appropriate size range of particles to take advantage of the enhanced permeability and retention (EPR) effect. We discovered that the size of the condensed RNAi polyplex nanoparticles generated from the MS could be tuned by controlling the initial MS size, which can be varied with the RCR enzymatic reaction time. Thus far we have noted that the nanoparticles generated scale with the MS size by a factor of 1/10. The sizes of the condensed nanoparticles range from 50 nm to 200 nm, based on their initial MS core diameter ranging from 500 nm to 2000 nm. We expect that this size tuning strategy can facilitate efficient intracellular uptake and improve accumulation in OC tumor regions through systemic administration of the appropriately sized nanoparticles.

Investigation of csiRNA derived from single component RNAi MS and csiRNA co-assembly with self-assembling copolymers

Assembling pure csiRNA that can be obtained directly from the RNAi MS with self-assembling block copolymers or other polyelectrolyte systems offers an alternative route for delivering RNAi therapies from the RNAi MS systems. We isolated pure csiRNA from RNAi MS by nanofiltration after dissolving the magnesium pyrophosphate lattice structure from the RNA microsponges with EDTA; after optimizing the RCT reaction, we obtain a high yield of csiRNA (mg scale) with an average molecular weight of 240 kDa, or ~20 monomeric siRNA equivalents. We postulated that the large size of csiRNA would facilitate its assembly with polymers. As a proof of concept to study csiRNA assembly, we selected $PEG_{5k}PLL_{30}$, a commercially available, biocompatible block copolymer with a positively charged polypeptide block that binds and condenses negatively charged nucleic acids and a water soluble neutral polyethylene oxide block that acts as a stealth

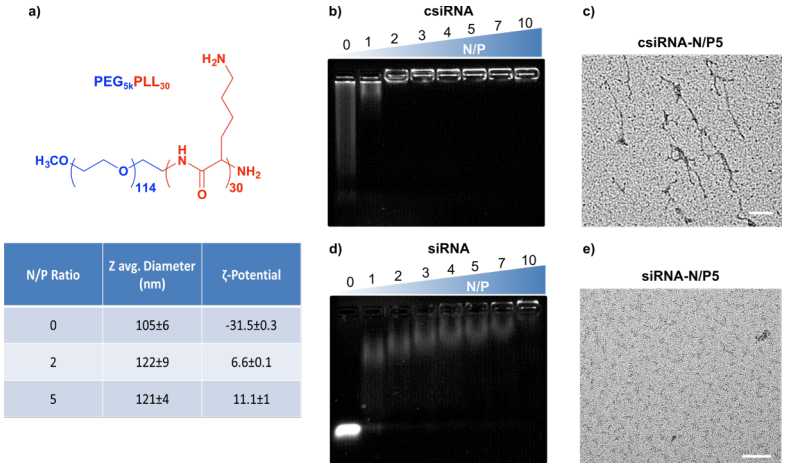

N/P Ratio	Z avg. Diameter (nm)	ζ-Potential
0	105±6	-31.5±0.3
2	122±9	6.6±0.1
5	121±4	11.1±1

Figure 2. Complexation of csiRNA and siRNA with $PEG_{5k}PLL_{30}$. a) Chemical structure for the $PEG_{5K}PLL_{30}$ polymer and table showing size and ζ-potential for selected csiRNA samples. b,d) Gel shift assay for titrations of csiRNA (top) and siRNA (bottom) with $PEG_{5k}PLL_{30}$ (1.5% agarose, TBE). Complexes were allowed to equilibrate in PBS prior to loading on gel. c) TEM image of csiRNA-N/P5 complexes and e) siRNA-N/P5 complexes (scale bars = 50 nm).

layer to stabilize particles in the blood stream (Figure 2a). PEG-PLL is a commercial block copolymer that has shown some promise for gene delivery. In our recent studies, we found that $PEG_{5k}PLL_{30}$ binds csiRNA more readily than monomeric siRNA: complete charge neutralization occurs at an N/P ratio of ~2 for csiRNA, compared to an N/P ratio of ~10 for monomeric siRNA (Figure 2b,d). The csiRNA- $PEG_{5k}PLL_{30}$ complexes have hydrodynamic radii of ca. 120 nm by DLS while TEM reveals a filamentous particle structure (Figure 2c). In contrast, even at high N/P ratios (i.e., 5-10), monomeric siRNA does not form detectable nanoparticles when complexed to the same polymer (Figure 2e). The csiRNA- $PEG_{5k}PLL_{30}$ complexes appear stable in human serum for several hours; between 24-110 h, nucleases gradually break down the polymeric csiRNA into smaller fragments, the smallest of which is the single 21 bp band (Figure 3) that corresponds to a single strand unit of siRNA. As a result, csiRNA-polymer complexes might act as slow-releasing siRNA depots in circulation.

The greater length of the csiRNA can provide better stability to polyplexes compared to those formed from siRNA. The initial polymer chosen for co-assembly with csiRNA, the PEG-PLL block copolymer, is useful to obtain early results in these systems. However, more compatible systems that break down following delivery or that are bio-resorbable will be helpful in the translation of these approaches, and the need to design for selective uptake by tumor cells remains; furthermore, the high loading of siRNA that is released over extended timeframes offers promise that might be best realized with copolymers that further facilitate disassembly and endosomal escape. We are seeking further improvements in csiRNA polyplex serum stability, targeting, transfection efficiency, and compatibility using biodegradable polycation selection and an LbL approach. We have found that poly-L-arginine in particular can provide stable complexation and cell-penetrating abilities. Incorporation of poly-L-histidine to aid endosomal release will be tested as well. Coating the csiRNA polyplex with a hydrophilic layer such as hyaluronic acid or a folate-functionalized PEG block copolymer can enhance blood circulation time and tumor cell uptake.

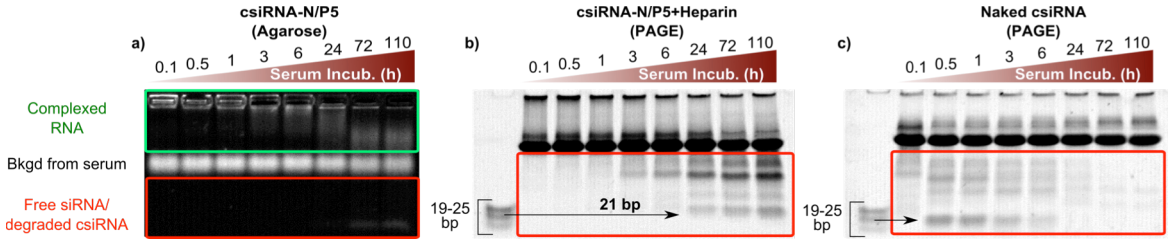

Figure 3. csiRNA is protected in 50% serum when complexed to $PEG_{5k}PLL_{30}$. a) csiRNA-N/P5 complexes show a gradual gel shift over the course of 110 h indicating slow decomposition of the complexes, however, little free RNA is detected even up to 110 h. (1.5% agarose); b) Heparin was used to break apart csiRNA-N/P5 complexes prior to loading onto a 15% PAGE gel, revealing a gradual increase in small RNA fragments over time, including the 21 bp fragment; c) PAGE of naked csiRNA following the same serum treatment shows a similar degradation pattern that develops over a much shorter time course.

The csiRNA may also afford more stable and efficient encapsulation than siRNA in electrostatically assembled layer-by-layer carrier systems. We will incorporate csiRNA layers into LbL nanoparticles, which may increase RNA loading per particle and thereby gene silencing efficiency. Our previous work has identified poly-L-arginine as a successful polycationic component in LbL nanoparticles for gene knockdown by siRNA. We will examine different nanoparticle cores, including quantum dots for in vivo imaging and biodegradable nanoparticles such as PLGA nanoparticles. Encapsulation of the csiRNA into the latter will also be investigated as a potential improved delivery system over siRNA-encapsulated biodegradable nanoparticles.

IACUC Approval. All animal experiments have been carried out in accordance with: (a) DOD Instruction 3216.01, "Use of Animals in DOD Programs"; (b) US Army Regulation 40-33, "The Care and Use of Laboratory Animals in DOD Programs"; (c) Animal Welfare Regulations (CFR Title 9, Chapter 1, Subchapter A, Parts 1-3), protocol OC120504 entitled, "Copolymer Micelles as New Targeted Drug Delivery Systems," IACUC protocol number 0812-078-15 is approved by the USAMRMC Animal Care and Use Review Office (ACURO) for the use of mice and will remain so until its modification, expiration or cancellation. This protocol was approved by the Massachusetts Institute of Technology, Cambridge IACUC, October 23rd, 2013.

1.2 Develop and test a multi-sequence RNAi MS targeting multiple OC pathways.

We have recently developed a new modular approach (Multi-RNAi MS) in synthesizing multiple components of csiRNA molecules incorporated delivery system to improve the applicability of RNAi-MS. Key to this multi-RNAi-MS delivery platform is the ability to produce a single delivery agent by assembling multiple functional and structural types of csiRNA molecules within a microsponge structure, thus it enables simultaneous delivery of large amounts of multiple RNA components. This robust engineering approach can be also designed to incorporate two or more csiRNA molecules types with precisely controlled molecule ratios (Figure 4).

Dual component Multi-RNAi MSs were initially made to target two different reporter genes (*e.g.*, GFP and RFP) to facilitate rapid optimization of its design with respect to transfection efficiency. Several thousands copies of multiple csiRNA per particle were successfully generated and safely delivered to cancer cells by the rearrangement of nano-sized complexes structures with biocompatible cationic polymers in order to improve their efficacy, while preserving its unique biological functions.

This development of Multi-RNAi MS will be pursued to enable the delivery of RNAi targeting two or more specific OC pathways at once. For targeting multiple OC pathways, we selected several different genetic sequences, all related to the FGF18 signaling pathway and recommended by the Birrer lab, and successfully synthesized a variety of Multi-RNAi MS systems. We are planning to further examine FGF18-related csiRNA combinations to observe potential additive or synergistic therapeutic effects *in vitro*. In addition, the transfection of these systems are in the process of being confirmed *in vitro* and quantified using qRT-PCR prior to moving forward with *in vivo* testing.

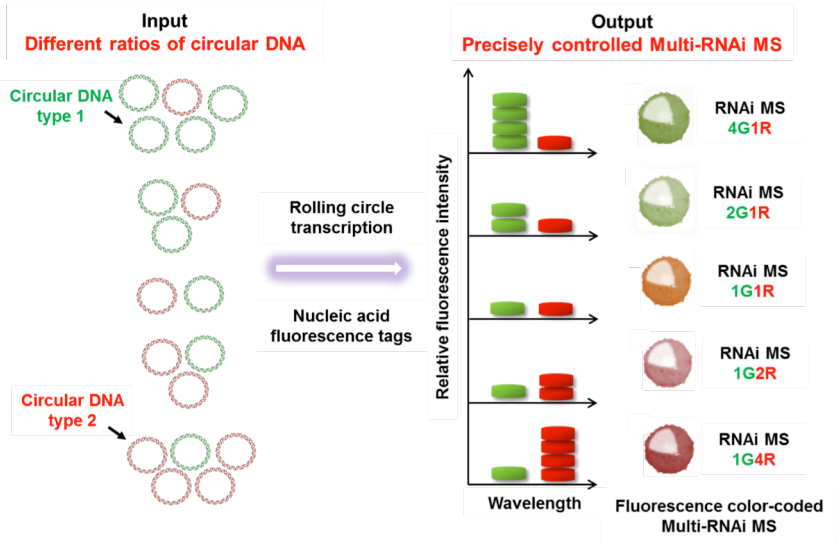

Figure 4. Design of multiple component RNAi microsponges with ratio control approach that allows tuning of the relative amounts of each siRNA sequence.

1.3 Develop and test systemic delivery of RNAi MS and csiRNA via intravenous injection:

Systemic Properties of LbL RNAi MS nanoparticles:

To address the systemic delivery of the RNAi MS system, we further modified the resulting condensed polyplexes generated from the microsponges using layer-by-layer (LbL) assembly to create a condensed nanoparticle with an outer stealth layer that can direct targeting and enable a degree of hydration and charge that lowers uptake of nanoparticles by monocytes and phagocytes in the bloodstream. Key design parameters such as layer components, layer number, and layer order made this platform a valuable option for tuning properties that influence systemic delivery.

We demonstrated that the electrostatically assembled multi-layered nucleic acid delivery system presents enhanced pharmacokinetic stability by manipulating surface chemistry and the number of particle layers. Further modification using this LbL system with Single- or Multi-RNAi MS will be developed and examined for targeting OC. Short regulatory nucleic acids such as antisense oligonucleotides (ODN), composed of a DNA backbone, have a similar function as siRNA for specific target selectivity in gene silencing and have been utilized as one of the promising treatment approaches for cancer. Recently we have developed electrostatically assembled multi-layered DNA-based therapeutic delivery approach for systemic delivery of polymeric ODN by adapting our microsponge system accordingly. [REF-ACS Nano revision] In this study, we have reported a new approach to generate a polymeric form of ODN that is effectively self-assembled into ODN microsponge structures (ODN-MS). In addition, this platform allows the condensation of polymeric ODN from ODN-MS for efficient nucleic acid therapeutic loading and further employs LbL assembly onto the condensed ODN-MS for systemic delivery.

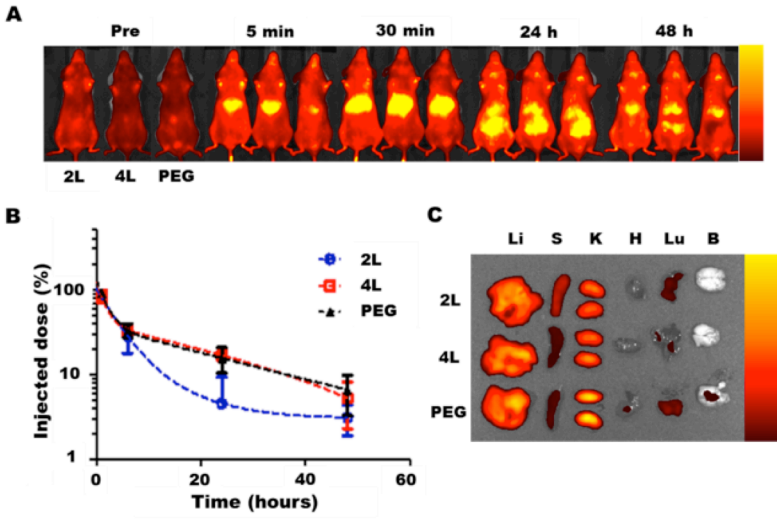

Figure 5. Systemic delivery of LbL-ODN nanoparticles. A) Represenative biodistribution data for differentially layered LbL-ODN-NPs (2L, 4L, and PEG) formulations following IV-administration in BALB/c mice after 5 min, 30 min, 24 h, and 48 h. Data presented with mice imaged ventrally at λex = 640 nm, λem = 700 nm. ODN-MS/PLL/DNA (2L), ODN-MS/PLL/DNA/PEI/DNA (4L), ODN-MS/PLL/DNA/PEI/PEG (PEG). B) Pharmacokinetics of nanoparticle clearance from IV-administered BALB/c mice with various LbL-ODN-NPs formulations - fit with a 2-phase decay model (PRISM®). C) Necropsy was performed at the terminal 48 h time point and presented in order. (Li = liver, S = spleen, K = kidneys, H = heart, Lu = lungs, B = brain).

For both RNAi MS and ODN MS forms of the microsponge system, this platform possesses multi-functionality because of the selection of appropriate functional biomaterials including PLL, DNA, PEI, and PEG. Fine-tuning of their multifunctional properties was achieved for imaging, improved intracellular uptake, controlled *in vivo* stability, and therapeutic efficacy with a negligible cytotoxicity. Importantly this system showed the enhanced pharmacokinetic plasma half-life stability and the appropriate biodistribution for meaningful systemic delivery to targeted tissues by manipulating surface chemistry and the number of particle layers (Figure 5). Overall, these improved biological performances were attributed to the selection of appropriate biomaterial candidates for controlling the surface properties of the ODN nanoparticles, the stability of inherent polymeric ODN, and the use of

stabilizing LbL architectures. Key design parameters such as layer components, layer number, targeting moiety, and layer order will be considered a valuable option for tuning particle properties. To achieve appropriate systemic biodistribution of RNAi MS and improved plasma half-life for systemic delivery to OC tumors, we further engineered the condensed polyplexes generated from the Single RNAi MS using layer-by-layer (LbL) assembly. Further modification using this LbL assembly method with the Multi-RNAi MS described in Aim 1.2 will be examined for targeting OC.

Pharmacokinetics of csiRNA-polymer complexes:

Rapid renal clearance is a major barrier for systemic siRNA delivery. The increased size of csiRNA makes it larger than the renal filtration cutoff, providing a distinct advantage that could allow for prolonged circulation and increased tumor accumulation. We systemically administered fluorescently-labelled siRNA and csiRNA complexed with $PEG_{5k}PLL_{30}$ (N/P = 5) and compared the biodistributions and pharmacokinetics (Figure Z). Necropsy and live animal imaging of mice injected with the siRNA complexes show that by 30 minutes post-injection, the fluorescence signal is localized to the kidneys and bladder, with little signal in other organs, and only 5% of the injected dose remaining in the blood. The csiRNA complexes perform quite differently; they accumulate much more slowly in the kidneys and bladder, show increased accumulation in the liver and spleen, and persist in the blood at least three times longer. This prolonged circulation should in turn translate to improved tumor accumulation via enhanced permeation and retention, which we are now investigating. Further, by designing and synthesizing new PEG-polypeptide polymers with targeting ligands and optimized amino acid compositions, we expect to see highly specific and efficient *in vivo* transfection with csiRNA.

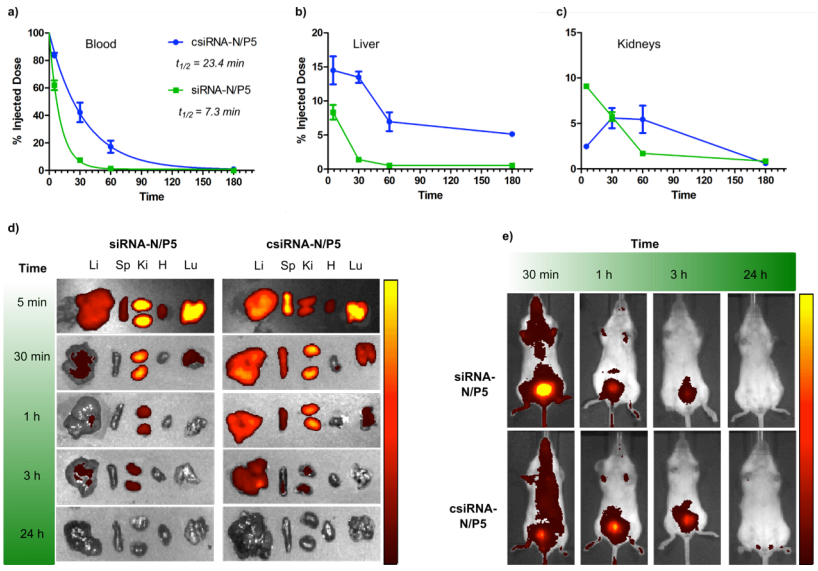

Figure 6. Biodistribution and pharmacokinetics of Cy5-csiRNA- and AF647-siRNA- $PEG_{5k}PLL_{30}$ complexes (N/P = 5) following tail vein injections into Balb/C mice. a-c) RNA quantification based on fluorescence intensity at different time points in blood, liver, and kidneys (*n* = 3). d) Representative images of organs harvested at different time points post-injection. e) Representative whole animal images (ventral side) at different time points post-injection.

Specific Aim 2: Modular LbL Nanoparticles for Temporal Release

Aim 2 Current Objective: By alternating polycationic and anionic species, we can use the Layer-by-Layer (LbL) method as a means of layered encapsulation of drugs on a nanoparticle core to enable delivery of additional therapeutics and targeting from the outer layers of the particle. The particle core can be a) a degradable polymeric or liposomal nanoparticle containing small molecule chemotherapy drugs for OC such as carboplatin, cisplatin or paclitaxel or b) an RNAi MS or ODN MS as described in Aim 1.3.

In Aim 2, we focus on (a); the LbL layers contain a specific RNAi sequence, thus enabling the delivery of synergistic sequences of multiple siRNA that work together, in combination with the small molecule chemotherapy drug contained inside the nanoparticle core. The objective of Aim 2 is to generate LbL nanoparticles containing chemotherapy drugs appropriate to OC in the core, with siRNA releasing layers formed around the nanoparticle core, and an external "stealth" layer that can facilitate systemic delivery and tumor targeting. The LbL nanoparticle approach is based on the concept of combination therapeutics in which siRNA is used to block specific survival pathways, followed by delivery of a chemotherapy drug that can then effect tumor cell death. The siRNA targets are specifically selected to take advantage of genetic pathways characteristic of advanced serous OC. We have selected chemotherapy drugs that induce DNA damage, and are of well-established use in OC.

Dr. Joyce Liu and Dr. Ronny Drapkin of the Dana-Farber Cancer Institute serve as the collaborators/unpaid consultants in this Aim to provide a clinical perspective and guidance in pre-clinical studies of specific combination drug/siRNA sets for targeting OC, and in the use of appropriate animal models to test these systems. The main focus of the Drapkin lab in the past few years has been deciphering the pathogenesis pathways of aggressive serous tumors; hence, his expertise is in the development/establishment of novel model systems that incorporate the fallopian tube (FT) as the true cell of origin for serous carcinomas.

Aim 2 Results, Progress, and Accomplishments with Discussion:

2.1 Modulation of release of chemotherapy drugs from nanoparticle cores coated with LbL membrane layers. Double strand DNA breaks (DSBs) are most deleterious to cells and if insufficiently repaired can result in genomic instability, and apoptosis[9]. To maintain genomic integrity, cells have evolved a tightly coordinated DNA damage repair (aka DNA damage response or DDR) pathway. Depending on the type of damage lesion, a number of different repair pathways are deployed. Homologous recombination (HR) or non-homologous end joining (NHEJ) is deployed for double-strand break repairs; and mismatch repairs, nucleotide excision repair and base excision repair for single strand breaks (SSBs)[10,11]. The genes *BRCA1*, *BRCA2 and poly ADP-ribose polymerase 1 and 2 (PARP1/2)* play a key role in maintenance of DNA integrity.

PARP1, a DNA repair enzyme inhibition results in accumulation of SSBs, which in proliferating cells collapses to generate DSBs when it encounters replication forks[12]. These DSBs need to be repaired via HR by BRCA1/2 proteins. Serous OC, which accounts for 70% of epithelial OC cases, harbors loss-of-function of *BRCA1* or *BRCA2* genes (BRCAness phenotype); hence these tumor cells are unable to repair DSBs, leading to genomic instability and eventual selective cell death. This phenomenon of loss-of-function *BRCA* genes in combination with inactivation/silencing of the PARP protein leads to exquisite cell death often referred to in literature as synthetic lethality[13].

To elicit the best potential synergy and the highest therapeutic efficacy at the lowest cytotoxicity, we will use the platinum based DNA damage agent, Cisplatin, in a combination therapy with the PARP inhibitors (PARPi), Olaparib (AZD2281) and BMN 673[14] which are already in advanced clinical trials[10,15,16]. These free drug combinations will first be screened in COV362, OVCAR4 and OVISE cells. The IC50 values will then be used to formulate liposome-based LbL for *in vivo* treatment of serous OC. These four cell lines were selected based on our current molecular profiling with Western blots of OC lines (see **Figure 7a,b**).

A wide panel screening of the key gene products altered in serous OC cell lines was completed using western blot. We decided not to use SKOV3 in our studies due to two recent publications[17,18] which are based on genomic characterization to profile OC cell lines most suitable for modeling high-grade serous OC. The western blot data will be used to help select the cell lines suitable for the cisplatin/PARPi combination and the appropriate targeting moiety to be attached to the outer layer of the LbL nanoparticles to achieve the highest selectivity of cancer cells *in vivo.*

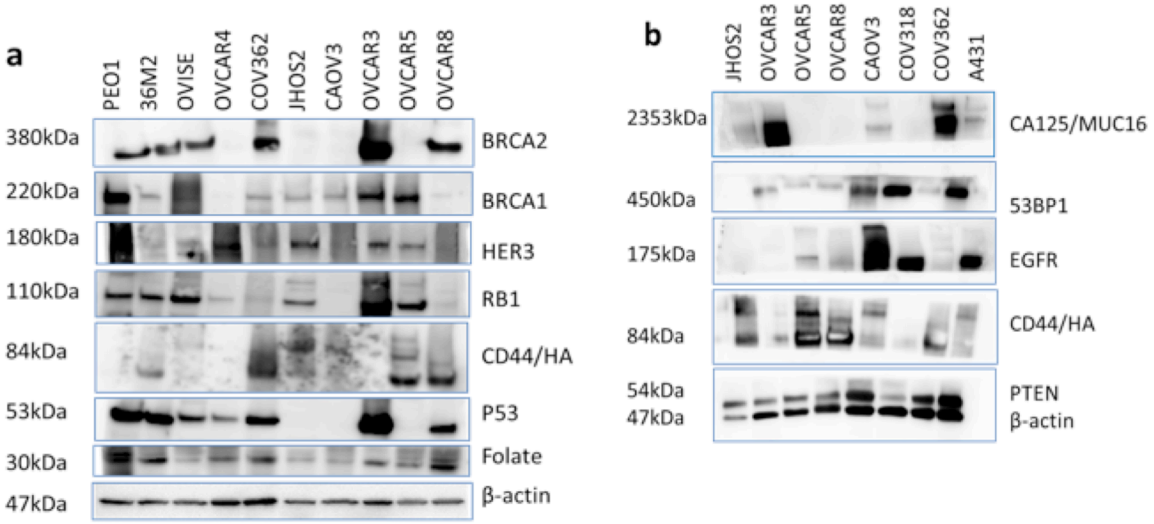

Figure 7: Western blot data showing expression profile of key biomarkers altered in high grade serous OC cell lines that are believed to contribute to the OC pathogenesis. Less than 10 passage number of each cell line was cultured and protein nuclear and cytoplasmic protein extracted. 40µg of each protein lysate was separated on SDS-PAGE and probed with anti-BRCA1,anti-BRCA2, anti- HER3,anti-RB1,anti-CD44, anti-P53 and anti-folate receptor antibody(**a**) and anti-CA125,anti-53BP1, anti-EGFR and anti-PTEN (**b**). β-actin was used as loading control and anti-rabbit IgG HRP link antibody used to detect protein bands using ECL chemiluminescence detection reagent on 400 Image Quant imager.

Combinations of the PARP inhibitors with Cisplatin is currently underway. This study is being carried out in COV362, OVCAR4 and OVISE (control) cell lines to determine the synergistic efficacy for each cell line. The IC50 value of each drug will be used to load the respective drugs into liposomes layered with PLL-Cy5.5 and surface functionalized with the appropriate molecular targeting moiety i.e HA (targeting CD44), Folate (targeting folate receptor) and an HA-Folate conjugate. DCC and NHS chemistry is currently being used to synthesis the HA-folate-PLL conjugate.

Confocal immunofluorescence assay is being used to evaluate inhibition of HR and formation of DSBs nuclear foci by combination drug treatment in COV362, OVCAR4 and OVISE using the following antibodies, Rabbit polyclonal anti-phosphorylated ɣ-H2A, anti-RAD51, anti-PARP1, anti-p53. Preliminary data show increased accumulation of ɣ-H2A, anti-RAD51nuclei foci in COV362 and OVISE cell line after 24hr treatment with 10, 20 and 50µM with Cisplatin and Rucaparib. COV362, OVCAR8, OVCAR4 and OVISE cell lines were titrated with 10, 20, $40x10^6$ of each cell type in SCID mice to determine the appropriate cell number required for implantation and formation of robust *in vivo* tumors prior to treatment with liposome nanoparticles. Preliminary data show that these 4 cell lines form robust subcutaneous OC

tumors that can be used in animal studies. COV362 ($20x10^6$), OVCAR4 ($20X10^6$), OVCAR8 ($10X10^6$) and OVISE ($40X10^6$) in two weeks attained the size of 80-120mm^3.

Specific Aim 3: A New Approach to OC Molecular Targeting

Aim 3 Current Objective: Several studies of OC biomarkers suggest that there are specific cell surface receptors that are upregulated in ovarian tumors that can be used as molecular targets for therapeutic delivery. Results in our lab indicate for the first time that systems with optimized 3D clustering of ligand groups can lead to significantly higher intracellular uptake, as presented in a simple tumor model. Our early work used the folate receptor, which is overexpressed in many ovarian tumor cell lines; however, the systems can be tailored for individualized medicine approaches using different ovarian tumor surface biomarkers, including short peptides or antibody fragments selected to bind to specific receptors[19-21]. Higher order oligomer formation of epidermal growth factor receptor has been studied by many research groups [22]. Recent results from Liu, Livingston and coworkers have shown that ErbB3 receptor plays a significant role in tyrosine kinase signaling and tumor growth in OC primary tumors. The use of controlled multivalent interactions to bind these receptors in a manner that inhibits kinase signaling can lead to significant down-regulation of kinase signaling as well as enhanced uptake of the chemotherapy-loaded nanoparticles, thus providing a dual synergistic mechanism for tumor treatment that could significantly change the nature of targeted tumor treatments by blocking cell growth, inhibiting resistance and killing tumor cells with greatly enhanced efficacy and specificity. The objective of this work is thus to a) use a synthetic polypeptide based block copolymer system to design nanoparticles with high efficacy in siRNA encapsulation and release, while b) furthering the design of the hydrated "exterior" block to enable the presentation of ligand-clusters on the surfaces of the resulting assembled polymer nanocarriers via the use of linear-linear and linear-dendritic block copolymers. The approach will include the design of dendritic macromolecules that are functionalized with the EGF protein or a corresponding short peptide that binds EGF and/or the Neuregulin 1b peptide domain. We will examine components of these block copolymer systems as modular elements that can be combined for optimal targeting of OC tumors and siRNA efficacy. Unpaid collaborators and consultants in this project include Michael Yaffe of the Koch Institute, MIT.

3.1 Synthesis and characterization of new synthetic polypeptide conjugates for siRNA encapsulation and development of linear and dendritic copolymer synthetic systems at a varying degree of conjugation.

Peptide Block Copolymer for optimized siRNA encapsulation and release:
Drugging Metastatic and Locally-Disseminated Solid Tumors Using RNAi Combination Chemotherapy

Synthetic lethality is a therapeutic strategy where the loss of either of two genes, alone, is non-toxic, while loss of both, simultaneously, results in rapid cell death. This strategy can be difficult to achieve using traditional drug carriers because, ideally, it requires efficient delivery of both oligonucleotides and front-line chemotherapeutics. Ovarian cancers, particularly

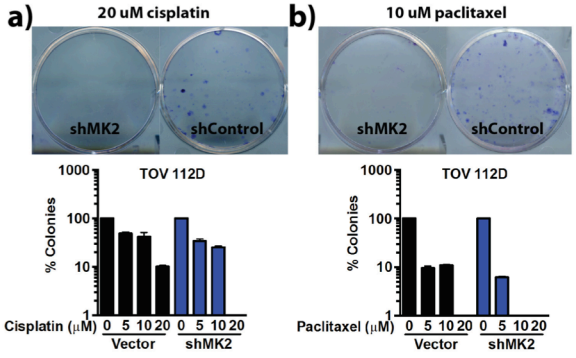

Figure 10. Loss of MK2 in high-grade serous ovarian cancer cells sensitizes towards platinum and taxane therapy.

those of the high-grade serous subtype[23] (96%), are characterized by mutations in the gene encoding the tumor suppressor protein, p53. Lung adenocarcinomas[24] (46%) and squamous cell carcinomas[25] (81%) are likewise characterized by mutations in this key tumor suppressor.

In collaboration with the Yaffe lab, also at MIT, we identified a novel downstream signal effector in the p38 MAPK stress response pathway – activated in response to platinum chemotherapy – whose loss is synthetically lethal in both lung[26,27] and ovarian cancer cells that lack functional p53 (**Figure 1**). To exploit this new vulnerability, we have engineered a series of lipid-like polypeptide (LLP) co-polymers that self-assemble into nanoscale drug carriers that efficiently package and deliver small interfering RNA (siRNA) and platinum chemotherapeutics specifically to cancer cells. Small interfering RNA delivered to cells with functional p53 is non-toxic, while potent cell killing is observed in lung and ovarian tumor cells treated with platinum or taxane chemotherapy. These biodegradable nanotechnologies not only protect the siRNA from degradation during circulation, but also improve the fraction delivered to the tumor, augmenting potential treatment response and minimizing dose-limiting toxic effects. 80% of ovarian cancer patients are diagnosed with late-stage disease (FIGO Stage III and IV), where the tumor has disseminated within and beyond the peritoneal cavity, respectively.[28] A majority of lung cancer patients (57%) are likewise diagnosed with metastatic disease. Safe and effective treatment strategies are urgently needed to combat the poor prognoses of these terrible diseases.

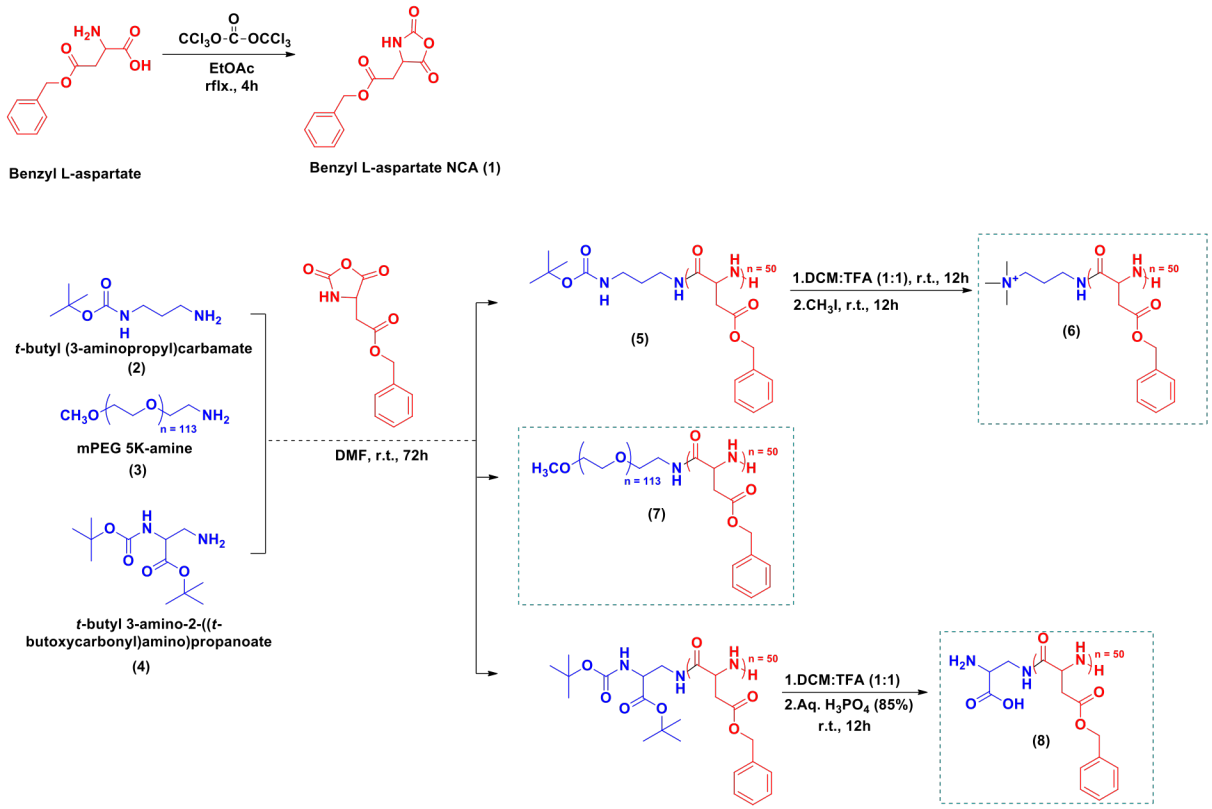

Scheme 1: Synthetic route towards polypeptide-based homopolymer and block copolymer with self-assembly property. The structure of the final products (6-8) are highlighted.

To generate self-assembled polypeptide-based nanocarriers, we have synthesized a set of homopolymer and block copolymer candidates **(6-8, Scheme 1)** using N-carboxyanhydride (NCA) mediated anionic ring-opening polymerization of side-chain protected amino acid. We

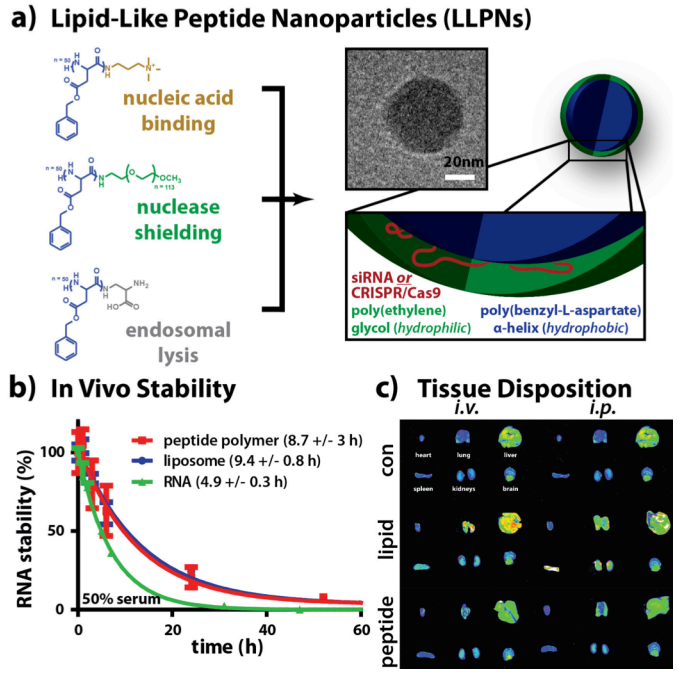

Figure 11. Lipid-like peptides (LLPs) self-assemble into nanoscale carriers for tumor-targeted delivery of siRNA and CRISPR/Cas9. a) LLP components bind nucleic acids, protecting them from nucleases, and facilitating cytosolic entry following tumor-targeted delivery. LLP nanoparticles (LLPNs) are sub-100 nm in diameter as imaged by cryogenic transmission electron microscopy (cryo-TEM). b) LLPNs improve the *in vivo* stability of 22-mer RNA >two-fold, equivalent to traditional lipid carriers, and (c) decrease off-target delivery to MPS organs.

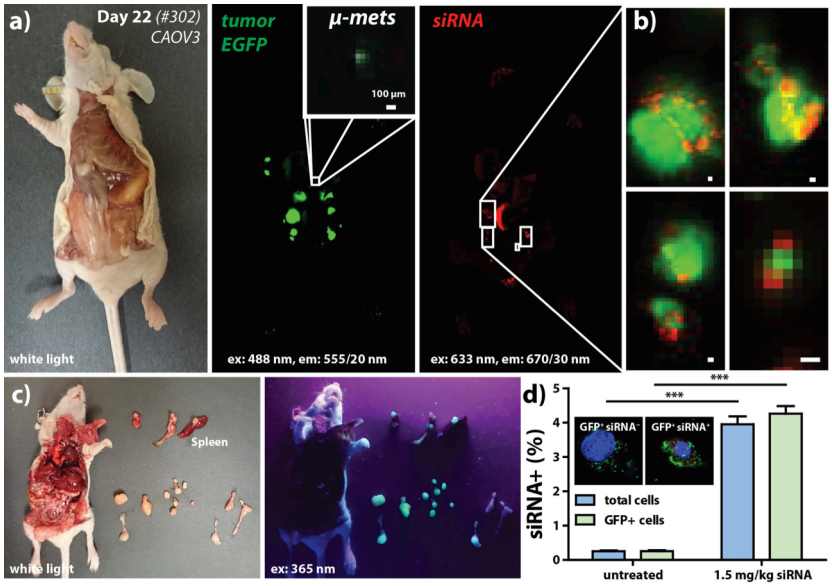

Figure 12. Lipid-like peptide nanoparticles deliver siRNA to mouse models of Stage III ovarian cancer. a) Immunodeficient NCR nude mice with intraperitoneally disseminated xenografts at 22 days post implantation. Following intreperitoneal LLP nanoparticle delivery of fluorescently labeled siRNA (24 h), in situ fluorescence imaging of tumors (green) and siRNA (red) indicate (b) significant siRNA/tumor colocalization at both micrometastes and larger tumors. c) Fluorescence-guided surgical resection and (d) subsequent fluorescence microscopy and flow cytometry of the dissociated tumors indicates high *in vivo* siRNA transfection efficiency, >4% of totoal burden after a single 1.5 mg/kg siRNA dose. Scale bars are 100 μm.

have selected this controlled polymerization route since the reaction process is well-documented to yield synthetic analogs to biocompatible natural polypeptides with programmable function[29,30]. As nucleophilic initiators, *t*-butyl (3-aminopropyl) carbamate **(2)**, α-methoxy-ω-amino-poly (ethylene glycol) **(3)** and *t*-butyl 3-amino-2-((*t*-butoxycarbonyl) amino) propanoate **(4)** has been used to introduce regio-selective placement of anionic and cationic charges along the polymer backbone of the final product. As a general synthetic route, benzyl L-aspartate was first decarboxylated to its highly reactive carboxyanhydride **(1)** using triphosgene, and the resultant aspartate NCA was polymerized using the initiators **(2-4)** in a protic solvent under inert atmosphere. Orthogonal deprotection strategy was carried out on product molecules to remove the protective groups without affecting the structural integrity or the molecular weight of the synthesized polymers. We envisioned that, owing to hydrophobic interactions, the benzyl protected aspartate block will self-assemble into a nanoscale aggregate in aqueous environment, extending the charged hydrophilic groups (i.e. ionizable amine functional groups and PEGs) towards the exterior, hence forming nanostructures amenable to hierarchical modification through electrostatic complexation with siRNA.

Our novel LLPs self-assemble into sub-100nm nanoparticles (**Figure 11a**) in the presence of 21-23-mer siRNA. *In vitro*, LLP nanoparticles outperform high-efficiency commercial transfection reagents (e.g. RNAiMAX) in silencing

MK2 mRNA, a key signal effector of p38 MAPK signaling in ovarian cancer cells which mediates DNA damage repair at platinum-induced double strand breaks; . *Iin vivo*, LLP nanoparticles protect siRNA from nuclease degradation by endo- and exonucleases, abundantly present in human serum (**Figure 11b**), equal to or better than that traditional lipid-based carriers. LLP nanoparticles also target fluorescently-labeled siRNA delivery (**Figure 11c**) to tumor cells by the size-dependent enhanced permeability and retention (EPR) effect. We have observed the effective delivery of fluorescent 22-mer siRNA to GFP-expressing lung and ovarian tumor metastases *in vivo* (**Figure 12**) following systemic delivery, where we can detect siRNA/tumor co-localization using *in situ* fluorescence imaging, as well as efficient intracellular siRNA delivery by both and flow automated cell sorting (FACS) and by confocal fluorescence microscopy of dissociated, GFP-positive tumor cells.. We observe that ca. 4% of total tumor burden contains high levels of siRNA after a single 1.5 mg/kg siRNA dose. Active (ligand-directed) nanoparticle delivery approaches, Pharmacokinetics/dynamics investigations, and tumor remediation studies are currently ongoing.

Synthesis of linear-dendritic synthetic polypeptide block copolymers for Neu functionalization.

Murine EGF will be used, which has only one free amino group because it does not contain lysine side chain as in the human EGF. It is widely known that the conjugation through amino group does not affect its binding affinity or signaling ability. Conjugation of Neuregulin peptide functionalized dendrimers will also be completed (Neu-Dndr).

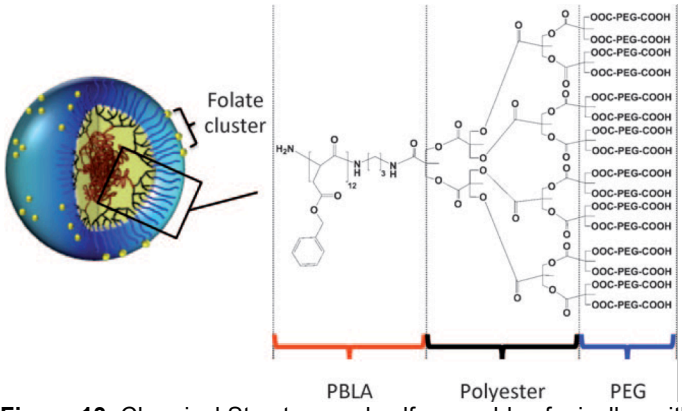

Figure 13. Chemical Structure and self-assembly of micelles with folate clusters on the surface.

In our previous work, we have utilized folate functionalized dendrimers to form micelles that present clustered folate on the surface (Figure 5). The dendrimer is composed of hydrophobic linear polypeptide to which a generation four polyester dendron is attached and hydrophilic 16 short polyethylene glycol (PEG) branches. Using folate receptor over-expressed KB cells, we have demonstrated that folate clustering can significantly enhance the intracellular uptake of the nanoparticles both *in vitro* and *in vivo*, thus leading to a more effective drug delivery system.

In this aim, we continue using the aforementioned dendrimer platform to investigate the clustering effect of other ligands. As neuregulin was known to bind to ErbB3, herein we use the active binding site of Neuregulin as the targeting peptide and conjugate t o our dendrimer platform. Using NCA ring-opening polymerization, we constructed the hydrophobic PBLA terminated with one azide group. In the next step, the generation 4 dendron was conjugated to the azide group of PBLA via click chemistry. The 16 short hydrophilic PEG chains were attached to the dendrons using N,N'-diisopropylcarbodiimide (DIC) coupling method. The obtained dendrimer was further functionalized with norbornene before the tetrazine-norbornene ligation. Tetrazine functionalized neureguline peptide is provided by

Imperiali group. Considering the molecular weight of Neuregulin peptide and steric hindrance, partial ligation to the dendrimer is anticipated.

3.2 In vitro examination of binding affinities of neuregulin functionalized nanoparticles will be examined as a function of neuregulin cluster size and density. Binding avidities will be determined using fluorescence measurements of these nanoparticles and the effect of different cluster size on binding will be compared. We expect to see the maximum binding affinity at which the degree of clustering is comparable to the receptor oligomer. Furthermore signal stimulation including AKT phosphorylation, ERK phosphorylation, and ErbB3 phosphorylationin in the presence of neuregulin ligand cluster functionalized nanoparticles will be examined to test whether the multivalence of neuregulin can inhibit the ErbB3-Neuregulin downstream signaling.

OCRP Ambassador: As the Teal Innovator Awardee, I have chosen to engage with the National Ovarian Cancer Coalition (NOCC) through its national and local chapter. By using the MIT Koch Institute as a platform, and working with these organizations, I have organized an Ovarian Cancer Symposium for survivors and advocates and the general public that will address and showcase the role of new technologies in addressing ovarian cancer, as well as provide a panel of experts to discuss the challenges and new developments designed to help treat disease. This symposium will take place in September, 2014. The workshop can be used to inform the public about the importance of funding research for ovarian cancer, and contribute to raising support and the profile of ovarian cancer.

I spent half of my sabbatical year in 2013 working with collaborators at Dana Farber to launch this program, while participating in research meetings and symposia with a focus on ovarian cancer to establish new connections with both clinical researchers and patients of ovarian cancer to broaden our work with new clinical perspectives.

KEY RESEARCH ACCOMPLISHMENTS:

- Demonstration of the ability to incorporate multiple sequences of RNAi into a single nanoparticle system. Because this approach ensures that each cell receives the appropriate amount of silencing across a range of pathways, this capability will allow the targeting of multiple survival pathways of an ovarian cancer tumor cell, thus blocking resistance and more effectively and efficiently achieving synthetic lethality with the use of RNAi.
- A new understanding of the RNAi MS system enables us to work both directly with the microsponge particles to convert them into condensed nanoparticles of csiRNA, or to extract the long chain csiRNA out of the microsponge structures first, to enable their self-assembly with block copolymers to form nanoparticles. This capability gives us a broader means of packaging and delivering these systems while retaining the unique advantages of the csiRNA in both cases.
- Studies of the circulation of the csiRNA generated by the RCT process suggest that it accumulates much more slowly in the kidneys and bladder than regular short sequences of siRNA. It shows increased accumulation in the liver and spleen, and much longer blood half-life by at least a factor of 3. This prolonged circulation, which has not been studied previously, should in turn translate to improved tumor accumulation via enhanced permeation and retention.

- Development of a dual responsive outer targeting layer for LbL nanoparticles that provides long blood circulation times and effective targeting of tumors based on a) nanoparticle size; b) hypoxic tumor environments and c) molecular ligand targeting via the CD44 receptor. This concept of multi-targeting and tumor responsive function is one that can be applied across a broad range of nanoparticle systems for enhanced tumor targeting and selectivity.
- Development of a dual treatment for ovarian cancer that targets MAPK2 and the DNA damage response pathway through siRNA against MK2 and cisplatin.

CONCLUSIONS

At the close of the first year of funding, we have made significant progress in the development of three key siRNA delivery platforms that offer unique advantages in addressing ovarian cancer.

We have found that the RNAi MS platform can be packaged by direct modification or by extraction of the csiRNA from the sponge structures, thus providing a broader range of methods for the packaging of these systems. Furthermore, we find that the csiRNA created in this platform exhibits unique and potentially highly advantageous biodistribution and plasma half-life and may enable very long term suppression of certain oncogenic signatures. Future work includes further investigation of packaging methods for these systems that will enable the most optimal siRNA transfection, and the testing of single and new multi-RNAi systems that contain OC specific oncogenic siRNA targets in tumor models to examine potential remediation.

We have developed LbL nanoparticle systems designed specifically to delivery a chemotherapy drug for DNA damage from its interior, and siRNA that can block genes that promote or enable cell survival in the presence of the drug from its exterior. Our collaborations have led to appropriate siRNA targets and cell lines for this work, as well as the generation of liposomes that contain the cisplatin and PARP inhibitor combinations. Future work will involve examining the efficacy of the combination chemotherapy nanoparticles, in particular when using LbL stealth targeting outer layers also developed during this grant period. Further work on the delivery of siRNA with the designated targets will be examined independently to determine efficacy in these systems, and siRNA/chemotherapy combinations will be verified in vitro, in preparation for in vivo testing in future.

Our synthetic polypeptide linear and linear-dendritic block copolymer platforms are currently being synthesized, and early results with a new lipid-like polypeptide system indicates high amounts of siRNA transfection in a Stage III ovarian tumor model. In our collaboration with the Yaffe lab, we have found a new siRNA target, that in combination with cisplatin, shows promising potential as a potent treatment using the polypeptide block copolymer platform for dual delivery.

PUBLICATIONS, ABSTRACTS AND PRESENTATIONS:

Journal Articles:

Dreaden, E.C., Morton, S.W.; Shopsowitz, K.E., Choi, J.H.; Deng, Z.J.; Cho, N.-J.; Hammond, P.T., Bimodal Tumor-Targeting From Microenvironment Responsive Hyaluronan Layer-by-Layer (LbL) Nanoparticles. *submitted to ACS Nano.*

Shopsowitz, K.E.; Roh, Y.H.; Deng, Z.J.; Morton, S.W., Hammond, P.T., RNAi Microsponges Form through Self-Assembly of the Organic and Inorganic Products of Transcription. *Small* **2014**, *10*, 1623-1633.

Roh, Y. H., Lee, J. B., Shopsowitz, K. E., Dreaden, E. C., Morton, S. W., Poon, Z., Hong, J., Yamin, I., Bonner, D. K., Hammond, P. T. Layer-by-Layer Assembled Antisense DNA Microsponge Particles for Efficient Delivery of Cancer Therapeutics. *ACS Nano*, *In revision* (nn-2014-02596b.R1)

Presentations:
Dreaden, E.C.; Morton, S.W.; Deng, J.; Hammond, P.T.; Layer-by-Layer Nanoparticles: Rational Delivery of Rational Drug Combinations. Fall Meeting of the Materials Research Society. 2013, Dec 1-6, Boston, MA.

Dreaden, E.C.; Morton, S.W.; Deng, J.; Hammond, P.T.; LbL Nanoparticles for Combination Cancer Therapies: Receptor Targeting and Microenvironment Response. Annual Meeting of Biomedical Engineering Society. 2013, Sept 25-28, Seattle, WA. (podium talk)

Dreaden, E.C.; Morton, S.W.; Deng, J.; Shopsowitz, K.E., Hammond, P.T.; Layer-by-Layer (LbL) Nanoparticles for Active Targeting of Tumor-Initiating and Drug-Resistant Breast Carcinoma. 2013 Dana-Farber Cancer Biology Departmental Retreat. 2013, July 26, Boston, MA.

Dreaden, E.C.; Morton, S.W.; Deng, J.; Shopsowitz, K.E., Hammond, P.T.; Active Targeting of Triple-Negative Breast Tumors Using Hypoxia-Responsive Layer-by-Layer Nanoparticles. Gordon Research Conference on Cancer Nanotechnology. 2013, July 14-19, West Dover, VT.

Shopsowitz, K.E.; Morton, S.W.; Dreaden, E.C; Hammond, P.T; Self-Assembled Nanoparticles of Enzymatically Generated Polymeric siRNA. Annual Meeting of Biomedical Engineering Society. 2013, Sept 25-28, Seattle, WA. (poster)

INVENTIONS, PATENTS AND LICENSES:

Dreaden, E.C.; Hammond, P.T.; 2014 April. Nanotechnologies for Tumor-Targeted Horizontal Blockade of MAPK and PI3K. Pending.

Dreaden, E.C.; Hammond, P.T.; 2014 April. Multimodal Tumor-Targeting Polyelectrolyte Drug Carriers. Pending.

REPORTABLE OUTCOMES:

- New means of synthesizing and packaging siRNA using rolling circle transcription to generate polymeric forms of siRNA – concatenated siRNA or csiRNA – in forms that enable single or multiple silencing of genes.
- Development of a new combination therapy approach to advanced serous ovarian cancer by addressing MK2 with cisplatin with promising in vitro results using targeted polypeptide copolymer carriers.
- New dynamically responsive outer stealth layer for ovarian cancer that can use hypoxic tumor environment as well as molecular targeting with ligands such as folate to greatly enhance uptake of nanoparticles by tumors.

OTHER ACHIEVEMENTS:

- P.T. Hammond, recipient, Alpha Chi Sigma Award, American Institute of Chemical Engineering (AIChE), to be received November 2014
- P.T. Hammond, Elected Fellow of American Academy of Arts and Sciences, October 2013
- P.T. Hammond, recipient, AIChE Stine Award in Materials Science, November 2013
- P.T. Hammond, Vice Chair, Gordon Conference on Drug Carriers, August 2014
- E.C. Dreaden, NIH Ruth L Kirschstein Postdoctoral Fellowship (F32), 2013-2015
- E.C. Dreaden, Koch Institute Image Award, MIT, 2014-2015
- E.C. Dreaden, Co-Chair, BMES 2013 Symposia: 'Nanotechnologies for Cancer Detection and Treatment' 2013

REFERENCES:

(1) Marchetti, C.; Pisano, C.; Facchini, G.; Bruni, G. S.; Magazzino, F. P.; Losito, S.; Pignata, S. *Expert Review of Anticancer Therapy* **2010**, *10*, 47.

(2) Metzger, O.; Moulin, C.; D'Hondt, V. *Current Opinion in Oncology* **2010**, *22*, 513.

(3) Pecot, C. V.; Calin, G. A.; Coleman, R. L.; Lopez-Berestein, G.; Sood, A. K. *Nature Reviews Cancer* **2011**, *11*, 59.

(4) Benoit, D. S. W.; Henry, S. M.; Shubin, A. D.; Hoffman, A. S.; Stayton, P. S. *Molecular Pharmaceutics* **2010**, *7*, 442.

(5) Goldberg, M. S.; Xing, D. Y.; Ren, Y.; Orsulic, S.; Bhatia, S. N.; Sharp, P. A. *Proceedings of the National Academy of Sciences of the United States of America* **2011**, *108*, 745.

(6) Vivas-Mejia, P. E.; Rodriguez-Aguayo, C.; Han, H. D.; Shahzad, M. M. K.; Valiyeva, F.; Shibayama, M.; Chavez-Reyes, A.; Sood, A. K.; Lopez-Berestein, G. *Clinical Cancer Research* **2011**, *17*, 3716.

(7) Lee, J. B.; Hong, J.; Bonner, D. K.; Poon, Z.; Hammond, P. T. *Nature Materials* **2012**, *11*, 316.

(8) Engler, D. A.; Gupta, S.; Growdon, W. B.; Drapkin, R. I.; Nitta, M.; Sergent, P. A.; Allred, S. F.; Gross, J.; Deavers, M. T.; Kuo, W. L.; Karlan, B. Y.; Rueda, B. R.; Orsulic, S.; Gershenson, D. M.; Birrer, M. J.; Gray, J. W.; Mohapatra, G. *Plos One* **2012**, *7*.

(9) Vilenchik, M. M.; Knudson, A. G. *Proc Natl Acad Sci U S A* **2003**, *100*, 12871.

(10) Jekimovs, C.; Bolderson, E.; Suraweera, A.; Adams, M.; O'Byrne, K. J.; Richard, D. J. *Frontiers in oncology* **2014**, *4*, 86.

(11) Chapman, J. R.; Taylor, M. R.; Boulton, S. J. *Mol Cell* **2012**, *47*, 497.

(12) Yu, S. W.; Wang, H.; Poitras, M. F.; Coombs, C.; Bowers, W. J.; Federoff, H. J.; Poirier, G. G.; Dawson, T. M.; Dawson, V. L. *Science* **2002**, *297*, 259.

(13) Clark, C. C.; Weitzel, J. N.; O'Connor, T. R. *Mol Cancer Ther* **2012**, *11*, 1948.

(14) Shen, Y.; Rehman, F. L.; Feng, Y.; Boshuizen, J.; Bajrami, I.; Elliott, R.; Wang, B.; Lord, C. J.; Post, L. E.; Ashworth, A. *Clin Cancer Res* **2013**, *19*, 5003.

(15) Reinbolt, R. E.; Hays, J. L. *Frontiers in oncology* **2013**, *3*, 237.

(16) Hosoya, N.; Miyagawa, K. *Cancer Sci* **2014**, *105*, 370.

(17) Anglesio, M. S.; Wiegand, K. C.; Melnyk, N.; Chow, C.; Salamanca, C.; Prentice, L. M.; Senz, J.; Yang, W.; Spillman, M. A.; Cochrane, D. R.; Shumansky, K.; Shah, S. P.; Kalloger, S. E.; Huntsman, D. G. *PLoS One* **2013**, *8*.

(18) Domcke, S.; Sinha, R.; Levine, D. A.; Sander, C.; Schultz, N. *Nature communications* **2013**, *4*, 2126.

(19) Zeineldin, R.; Muller, C. Y.; Stack, M. S.; Hudson, L. G. *Journal of Oncology* **2010**, *2010*.
(20) Sheng, Q.; Liu, J. *British Journal of Cancer* **2011**, *104*, 1241.
(21) Tsujioka, H.; Yotsumoto, F.; Hikita, S.; Ueda, T.; Kuroki, M.; Miyamoto, S. *Current Opinion in Obstetrics & Gynecology* **2011**, *23*, 24.
(22) Gadella, T. W., Jr.; Jovin, T. M. *J Cell Biol* **1995**, *129*, 1543.
(23) Cancer Genome Atlas Research, N. *Nature* **2011**, *474*, 609.
(24) The Cancer Genome Atlas Research, N. *Nature* **2014**, *advance online publication*.
(25) The Cancer Genome Atlas Research, N. *Nature* **2012**, *489*, 519.
(26) Reinhardt, H. C.; Aslanian, A. S.; Lees, J. A.; Yaffe, M. B. *Cancer Cell* **2007**, *11*, 175.
(27) Morandell, S.; Reinhardt, H. C.; Cannell, I. G.; Kim, J. S.; Ruf, D. M.; Mitra, T.; Couvillon, A. D.; Jacks, T.; Yaffe, M. B. *Cell Reports* **2013**, *5*, 868.
(28) Vang, R.; Shih, I. M.; Kurman, R. J. *Adv. Anat. Pathol.* **2009**, *16*, 267.
(29) Patterson, J.; Martino, M. M.; Hubbell, J. A. *Mater. Today* **2010**.
(30) Deming, T. J. *Prog. Polymer Sci.* **2007**, *32*, 858.

APPENDICES:

Contents include manuscript drafts for:

Dreaden, E.C., Morton, S.W.; Shopsowitz, K.E., Choi, J.H.; Deng, Z.J.; Cho, N.-J.; Hammond, P.T., Bimodal Tumor-Targeting From Microenvironment Responsive Hyaluronan Layer-by-Layer (LbL) Nanoparticles. *submitted to ACS Nano.*

Roh, Y. H., Lee, J. B., Shopsowitz, K. E., Dreaden, E. C., Morton, S. W., Poon, Z., Hong, J., Yamin, I., Bonner, D. K., Hammond, P. T. Layer-by-Layer Assembled Antisense DNA Microsponge Particles for Efficient Delivery of Cancer Therapeutics. *ACS Nano*, *In revision*.

Layer-by-Layer Assembled Antisense DNA Microsponge Particles for Efficient Delivery of Cancer Therapeutics

Young Hoon Roh[+], Jong Bum Lee[+], Kevin E. Shopsowitz, Erik C. Dreaden, Stephen W. Morton, Zhiyong Poon, Jinkee Hong, Inbar Yamin, Daniel K. Bonner, and Paula T. Hammond*

Abstract

Antisense oligonucleotides can be employed as a potential approach to effectively treat cancer. However, the inherent instability and inefficient systemic delivery methods for antisense therapeutics remain major challenges to their clinical application. Here, we present a new class of polymerized oligonucleotides (ODNs) that self-assemble during their formation through an enzymatic elongation method (rolling circle replication) to generate a composite nucleic acid/magnesium pyrophosphate sponge-like microstructure, or DNA microsponge, yielding high molecular weight nucleic acid product. In addition, this densely-packed ODN microsponge structure can be further condensed to generate polyelectrolyte complexes with a favorable size for cellular uptake by displacing magnesium pyrophosphate crystals from the microsponge structure. Additional layers are applied to generate a blood-stable and multifunctional nanoparticle *via* the Layer-by-Layer (LbL) assembly technique. By taking advantage of DNA nanotechnology and LbL assembly, functionalized DNA nanostructures were utilized to provide extremely high numbers of repeated ODN copies for efficient antisense therapy. Moreover, we show that this novel formulation significantly improves nucleic acid drug/carrier stability during *in vivo* biodistribution. These polymeric ODN systems can be designed to serve as a potent means of delivering stable and large quantities of ODN therapeutics systemically for cancer treatment to tumor cells at significantly lower toxicity than traditional synthetic vectors, thus enabling a therapeutic window suitable for clinical translation.

Keywords: DNA nanotechnology • Layer-by-Layer • Cancer • Multifunctionality • Antisense therapy • DNA oligonucleotide • DNA delivery

One of the major issues for the use of nucleic acids as active therapeutics for a broad range of cancers, infectious disease and other disorders is the safe and successful targeted delivery to specific organs upon systemic administration. We have reported a new approach to generating a polymeric form of small interfering RNA (siRNA) that are effectively self-assembled into RNAi microsponge structures that can provide dense concentrations of siRNA ultimately accessible within nanoparticles with orders of magnitude lower concentrations of potentially toxic polycation[1] and described the mechanism of self-assembly and structure of these microsponges.[2] Along with RNAi, similar delivery challenges exist for other important forms of short regulatory nucleic acids like antisense oligonucleotides (ODN) which have a DNA backbone, and we seek to adapt these methods accordingly. Furthermore, it is necessary to introduce further modification of the self-assembled particles derived from these microsponges to achieve systems with appropriate biodistribution and plasma half-life for meaningful delivery to targeted tissues.

Recently antisense therapy has been introduced as one of the promising treatment approaches for cancer because of its specific target selectivity in gene silencing, an improved understanding of molecular mechanisms in specific tumor types, and the recent identification of therapeutic target genes which were traditionally recognized as "undruggable".[3–7] When binding takes place, the bound ODN/RNA hybrids serve as substrates for enzyme-activated degradation (*e.g.*, RNase H) or physical blockage, resulting in the inhibition of translation of their target sequences. Despite the powerful therapeutic potential of ODNs, improved physico-chemical properties of ODN backbones (*e.g.*, specificity and stability), and efficient systemic delivery strategies are important prerequisites for its clinical application in cancer. Several useful chemical modifications of ODN backbones have been reported to achieve improved resistance to nuclease digestion and prolonged *in vivo* half-life.[8–11] In addition, for efficient antisense therapy to be clinically realized, major challenges must be addressed to achieve desirable therapeutic windows, such as ensuring lower toxicity from delivery agents and the use of lower quantities of packaging agents so as to provide high amounts of active ODN drug loading per carrier and improved stability in systemic circulation.[12,13] In addition, the

uptake of nanocarriers *via* endocytic pathways, its intracellular trafficking and effective endosomal escape, and the safe release of ODN drugs from nanocarriers to functional targets in the cytoplasm and nucleus should also be considered.[14–18] In order to deliver ODN therapeutics into a specific target area, rational design of nanoparticles is required based on particle size, surface chemistry, composition, shape, chemical functionality, and mechanism of action.[19]

An important aspect of DNA nanotechnology is the ability to engage molecular recognition and intrinsically define structural features with nanometer precision,[20–23] which facilitates the employment of useful strategies to construct functionalized DNA nanostructures for their use in biomedical applications.[24,25] Recently, several types of self-assembled functional DNA nanostructures, composed of relatively short oligonucleotides have been engineered for sensing, bioimaging, and drug delivery.[26–30] In particular, **r**olling **c**ircle **r**eplication (**RCR**) has been introduced as a powerful method for nucleic acid synthesis.[31] This process of nucleic acid replication is particularly favorable for the production of long repeated strands of nucleic acids in a stable form and at low cost. We have used **r**olling **c**ircle **t**ranscription (**RCT**) to create self-assembled RNAi microsponge structures[1] and more recently, the development of DNA hydrogels by using **r**olling **c**ircle **a**mplification (**RCA**) has been reported.[32] Both of these examples clearly demonstrate the power of RCR in nucleic acid nanotechnology. Key to our approach is the generation of concatenated or polymeric forms of nucleic acids that can be broken down in cells by a native intracellular enzyme, Dicer, to short oligonucleotide sequences relevant to gene silencing.

The resulting condensed polyplexes generated from the microsponges can be directly modified using the versatile approach of layer-by-layer (LbL) assembly,[33,34] for which key design parameters such as layer components, layer number, and layer order, make this platform a valuable option for tuning the properties in therapeutic nanoparticle delivery systems.[35–40] Delivery vehicles fabricated *via* LbL assembly can carry multiple functional components, precisely control the release of therapeutic drugs, and facilitate improved biodistribution of the drug-containing nanoparticle system. Various types of LbL nanoparticle delivery systems have been reported to facilitate cellular uptake,

improve both drug and carrier pharmacokinetics, and enhance molecular targeting capability.[41–48]

RESULTS AND DISCUSSION

As illustrated in **Fig 1**, we have developed a concatenated DNA-based LbL-assembled nanoparticle delivery platform. Using RCA, we initially generated self-assembled composite DNA microsponge structures containing ODN's in the form of long single-stranded oligonucleotide (ssDNA) polymers that each contain several thousands of repeated ODN copies complementary to a selected target sequence for antisense therapy. The DNA microsponges were then structurally disrupted by adding cationic polymers and salts, which displace the magnesium pyrophosphate crystals[2] that make up the scaffold of the microsponge; this process leads to the formation of nano-sized complexes. Using this approach, we employed a long polymeric ODN as the core region and applied additional outer-layer shells *via* LbL assembly. By rational design and selection of biomaterials, we incorporated multiple functional moieties in each layer compartment. In addition, these LbL assembled polymeric ODN structures demonstrated higher resistance to nuclease digestion, prolonged *in vivo* half-lives, and controlled release to overcome the inherent difficulties in their delivery.

Antisense DNA microsponge particles

To generate antisense particles that can self-assemble into organized microstructures, we first designed and prepared a linear ssDNA encoding complementary sequences of ODN (**see Supplementary Table S1**). As a proof of concept for biological function, we incorporated DNA sequences complementary to anti-luciferase ODN. The linear ssDNA strand (91 bases) was then hybridized with a primer ssDNA (22 bases), which was partially complementary to both ends of the linear DNA, to form a circular DNA. The nick inside the circular DNA was connected by enzyme ligation with a T4 DNA ligase. Gel electrophoresis was performed to demonstrate the synthesis of circular DNA from the linear DNA structure (**see Supplementary Fig S1**). A distinct band shift between circular and linear DNA was observed, indicating the successful assembly of circular DNA. In the RCA process, this engineered circular DNA was used as a template

for generating repeated polymeric ODN sequences. The reaction was carried out with high circular DNA concentrations (300 nM) in the presence of DNA polymerase and allowed to proceed for ~24 h at room temperature. Spherulitic sponge-like structures were formed consisting of a magnesium pyrophosphate crystalline phase that acts as a template for high loadings of polymeric ODN, for which each polymer strand contains approximately 1700 tandem repeats of anti-luciferase ODN. To prepare more uniform particles, the reaction solution was sonicated until the products were well dispersed. The morphology and structure of the RCA product was further studied using various microscopy techniques. Scanning electron microscopy (SEM) images showed that the ODN composite microparticles were uniformly sized (~2 μm), exhibited sponge-like porosity, and were spheroidal in shape (**Fig. 2A-B**). Due to their morphology and biological function, we refer to the resultant particles as oligodeoxynucleotide antisense microsponge particles (**ODN-MS**). In addition, transmission electron microscopy (TEM) images indicated that this structure was hierarchical, composed of multilayers of thin sheets that are further organized into a branched spherulitic structure. In the higher magnification TEM images, the two compartments are clearly visualized, including the multi-layers of thin sheets and the highly branched structure inside the particle (**Fig 2C-D**). Because of the presence of magnesium pyrophosphate, the structure of the ODN-MS was readily visualized without metal staining, unlike typical DNA TEM imaging. Morphological characteristics of the ODN-MS were further analyzed using fluorescence and confocal microscopy to clearly visualize the distribution of DNA in the microsponges. In fluorescence microscopy analysis, the existence of ssDNA in these particles was indicated by staining with SYBR II, a DNA-specific dye, which exhibits green fluorescence only when it binds with ssDNA. Based on these observations, we confirmed that the generated DNA product existed in ssDNA form in the microsponge structure (**see Supplementary Fig. 2).** Interestingly, a ring-shaped distribution of DNA was noticed in confocal microscopy images, indicating the highly localized presence of ssDNA at the edges of the particle surface. In this observation, we used both SYBR II staining after the microsponge structure formation and Cyanine 5-dUTP labeling during the RCA reaction, which results in bright red and green fluorescence, respectively (**Fig. 2E-F and Supplementary Fig. 2**).

We have demonstrated that ODN-MS consists of two different components. Here, one pyrophosphate anion (PPi) was produced from each nucleotide triphosphate during enzymatic nucleic acid polymerization by RCA. The resulting PPi product was bound by Mg^{2+} ions in the reaction buffer to form insoluble magnesium pyrophosphate (Mg_2PPi). To determine the structure of the ODN-MS, scanning transmission electron microscopy (STEM)-based energy dispersive X-ray spectroscopy (EDX) mapping was carried out to analyze the elemental composition of the ODN-MSs (**Supplementary Fig. 3**). Based on EDX, carbon (C) indicative of the presence of DNA, was found to be distributed in both the inner and outer particle regions. Similarly, magnesium (Mg), oxygen (O), and phosphorus (P) from $Mg_2P_2O_7$ were uniformly distributed throughout the particle. Point analysis of ODN-MSs using SEM-based EDX further supported the presence of carbon, oxygen, magnesium, and phosphorus, respectively, indicating a mixture of DNA and $Mg_2P_2O_7$ within the ODN-MSs (**Supplementary Fig. 4**). To better understand the crystallization of ODN-MSs during RCA, we used powder X-ray diffraction (PXRD) to analyze their crystallinity (**Supplementary Fig. 5**). The diffraction pattern matched well with the magnesium pyrophosphate phase $Mg_2P_2O_7{\cdot}3.5H_2O$. Taken together with the overall morphological and structural analysis of ODN-MSs, these supporting results suggest that the ODN-MSs generated during the RCA reaction are composed of DNA/inorganic composite materials, including densely packaged polymeric ODN and inorganic magnesium pyrophosphate crystals, similar to our observations for siRNA microsponges.[2]

We found that ODN strands from microsponges generated using the RCA approach were an unusually high molecular weight polymer structure. To confirm this notion, DNA microsponges were first prepared from circular DNA templates by RCA processes. These microsponges were then treated with EDTA to chelate Mg^{2+}. The subsequent DNA products were further analyzed using SEM and gel electrophoresis to characterize the polymeric size of DNA. SEM images indicated that the structure of ODN-MS was completely disrupted by the additional EDTA treatment (50 mM) facilitating the direct comparison of polymeric structures from particles (**Fig 3A**). Gel image showed that polymeric DNA was observed to run at a higher position on the gel indicating an extremely large product greater than 150 kb, corresponding to

approximately 43 million Da (**Fig 3B**).[49] Here, we confirmed that the generated DNA structures from the microsponge system were very long polymeric structures, which correspond to the number of ODN repeating units. Based on the molecular weight analysis, several thousand (~1700) ODN repeats, each of which have the specifically programmed target function of the ODN sequence, could be generated during the RCA process and incorporated into the ODN-MSs. In order to further examine the size of the incorporated DNA polymer into microsponges during the DNA synthesis process, we conducted a time course study of polymerized DNA products during varied RCA reaction times. At each reaction time point, ODN-MSs were isolated and DNA polymer sizes were compared by gel electrophoresis after disruption of the particles by EDTA. Based on the results from gel electrophoresis, high molecular weight DNA polymers were rapidly generated and incorporated even in the initial stages of microsponge formation (roughly equivalent to the 8 h RCA reaction) (**Supplementary Fig. 6 and Lane 2,4,6**); these sizes are significantly greater than those observed for the siRNA systems.[1,2] We performed a fluorescence-based measurement to quantify DNA loading in the ODN-MSs (**See Supplementary Information**). DNA loading within the microsponge was approximately 12.5 ± 1.8 wt%; overall we postulate that the localized loading of DNA at the edge of the particle may be due to the higher molecular weight of the ssDNA.

We demonstrated that the long chain polymeric ODN generated from the microsponge system exhibited dramatically improved serum and nuclease stability, presumably due to the protective effect of its polymerized form. We used an ssDNA quantification assay and gel electrophoresis to confirm this finding by evaluating the stability of the isolated polymeric ODN structure from microsponge under the harsh conditions of high serum (50%) and DNase (3 units/μL) concentrations, respectively. Serum stability results indicated that the polymeric ODN structure showed a significantly improved intrinsic stability compared to a standard short ODN (~22 bases). The amount of short ODN decreased with increasing serum incubation time (50% loss within 3 h). However, the polymeric ODN structure was extremely well protected from serum treatment during the 3 days of incubation (**Fig 3C and Supplementary Fig. 5**), and essentially maintained its large size. Furthermore the treatment of short ODNs with DNase caused them to fully degrade, leaving them undetectable by gel electrophoresis

(within ~15 min). In contrast, although some damage was observed under these harsh enzymatic conditions and long incubation times (3 days), the polymeric ODNs were significantly more resistant to DNase enzyme degradation (**Fig 3D and Supplementary Fig. 7**). To further explore the systemic delivery of the polymeric ODN, we performed an *in vivo* pharmacokinetics study in NCr nude mice. Mice were injected *via* the tail vein with Cy5 dye-labeled polymeric or short ODNs and compared using whole-animal and blood fluorescence imaging to understand the biodistribution and blood half-life and stability of these systems. Rapid clearance for short ODN was observed, as evident by a significant bladder signal (circled, 73% injected dose, based on bladder radiant efficiency signal relative to the total integrated fluorescence recovered) present as early as 5 min, while comparatively no bladder signal was evident for the polymeric ODN up to 30 min, validating the avoidance of renal filtration by polymeric ODN due to size (**Fig 3E**). Overall, the isolated polymeric ODN from microsponges was significantly protected from serum and enzyme degradation, and reduced *in vivo* renal clearance.

Polymeric ODN packaging by condensation

For achieving desirable cellular and systemic ODN delivery efficiency, it is essential to obtain favorable sizes and appropriate surface properties with compact ODN structures. In our approach, the ODN-MS structures were disrupted and the DNA product encapsulated in an additional process (i.e. a condensation step) to control morphology, charge, particle size, and surface structure. We further investigated the mechanism of this polymeric DNA packaging process during polycation condensation starting from the DNA/inorganic composite microsponge particles (**ODN-MS**). As we demonstrated previously, the microsponge can be easily broken down from its original structure by sequestering Mg^{2+} using chelating agents such as EDTA. In place of EDTA, we used cationic polymers (*e.g.*, poly-L-lysine: PLL) to act as a condensing agent for DNA. ODN-MS has a highly negative surface charge (-37.14 ± 1.46 mV) due to the presence of DNA and a relatively larger size (~1800 nm). The positively charged PLL binds readily with ODN-MS by electrostatic interactions, forming complex structures above a certain threshold concentration with the composite structure. Following this condensation step, ODN-MS transforms into a highly compact sized structure facilitating polymeric ODN

drug loading. We realized that the major parameter required for this condensation process is the initial reaction concentration of the positively charged polymeric condensing agent in the presence of salts (**Supplementary Table 2**). To find out the optimal conditions for condensation, PLL concentration was varied from 0.1 - 5 mg/mL. The morphology of the condensed ODN-MS products was compared with initial ODN-MSs using various microscopic techniques. SEM images showed that ODN-MS microstructures change their morphology during condensation depending on the concentration of the polycation. At intermediate concentrations of PLL (1.5 mg/mL), the particles decreased in size (approximately 1 μm) and became less porous than the initial ODN-MS structure (**Fig 4A-B**); however, we observed the formation of nano-sized complexes as the PLL concentration was increased (3 mg/mL, N/P = 0.5) (**Fig 4C**). We further examined the condensed structures by carrying out confocal microscopy with a dual-labeled fluorescence system (polymeric ODN: green color and PLL: red color) to observe the progression from microsponge to polyelectrolyte complexation. Confocal microscopy images were consistent with observations by SEM, which indicated that the initial microsponge structure decreased in size and formed condensed structures (**Fig 4D-G**). There was no change in the ODN-MSs at low PLL concentrations (below 0.4 mg/mL) in terms of the particle size and surface charge. PLL appears partially adsorbed to the ODN-MSs at intermediate concentrations of PLL (between 0.4 - 0.8 mg/mL). The shift of particle surface charge from -37.2 ± 1.5 mV (ODN-MS) to +4.6 ± 5.2 mV (ODN-MS/PLL) after exposure to 0.8 mg/mL PLL concentration supports the presence of PLL in the particles (**Fig. 4H-I**). Interestingly, at an intermediate concentration of PLL (1.5 mg/mL), we observed that the ODN-MSs shrunk from ~2 μm to approximately 1 μm, and that PLL was highly localized around the surface of ODN-MSs. This was indicated by a red hue (corresponding to PLL) that surrounds the green colored regions corresponding to polymeric ODN. At certain thresholds of PLL concentration (3 mg/mL), these structures form nano-sized polyplex structures composed of both PLL and polymeric ODN molecules, which are observed as yellow in color (corresponding to a merged color from both polymeric ODN and PLL). At this PLL concentration, we observed successful polymeric ODN-loading into polyplexes following the reconfiguration of the ODN-MSs. Following the condensation process, particles were isolated from free polycation in

solution by dialysis. The ODN particles derived from the condensing process were further investigated by dynamic light scattering (DLS) and zeta (ζ)-potential analysis (**Fig 4H-I**). As shown in Fig. 4H, the size of complex particles significantly decreased to 212.5 ± 15.6 nm after the condensing process. The average size of the original ODN-MSs was approximately 1800 nm ± 196.1 nm. ζ-potential also helped in the verification of the self-assembly of PLL with polymeric ODN. The change of particle surface charge from -37.2 ± 1.5 mV (ODN-MS) to +32.4 ± 1.6 mV (ODN-MS/PLL) indicated the successful complexation of polymeric ODN with PLL (**Fig. 4I**). Our results also suggest that the outer surfaces of the particle were saturated at 3 mg/mL of PLL solution because a significant increase in ζ-potential was not observed at higher concentrations of PLL. We performed elemental analysis for further investigation of the polymeric ODN packaging process using SEM-based EDX. Large differences between the relative amounts of O, Mg, and P were observed after condensation along with dramatically increased relative amounts of C and N, which suggests the successful release of magnesium pyrophosphate and the incorporation of polymer (PLL) during condensation (**Supplementary Fig. 4**). Here O, Mg, and P represent the presence of magnesium pyrophosphate ($Mg_2P_2O_7$•$3.5H_2O$). In addition, both C and N indicate the presence of the polymer-based condensing agent (*e.g.*, PLL). Further characterization of DNA packaging before and after condensation was carried out using powder XRD (PXRD). Specifically, the diffraction pattern of the ODN-MSs after condensation did not indicate the presence of magnesium pyrophosphate crystals in the particle (**Supplementary Fig. 5**); instead we observed a large broad peak consistent with amorphous polymer. These results demonstrate that PLL is capable of triggering the release of magnesium pyrophosphate from the ODN-MSs during condensation with the DNA product.

Overall, we found that the ODN-MS rearranges to form smaller nanoparticle complexes at certain threshold concentrations of polycation during condensation. This was attributed to electrostatic interactions and physical agitation along with the release of magnesium pyrophosphate crystals. In conventional ODN complexation approaches with polymers or lipids, the amount of ODN per particle is very limited due to the low surface charge and relative rigidity of short ODNs, making their encapsulation especially challenging. In contrast, this new approach uses a unique nucleic acid packaging process,

generating highly stabilized and densely packed complexes due to the physico-chemical properties of the structured microsponge such as a high localized surface charge density, and large surface area presenting localized concentrations of ODN with the improved condensation energetics and thermodynamic driving forces of polymeric ODN compared to rigid short ODN structures.[50] We believe that this process also allows a large amount of ODN encapsulation due to the localization of the negatively charged polymeric DNA on the microsponge surfaces, which facilitates polycation complexation of nucleic acids at higher concentrations relative to solution complexation.[51]

Properties of layer-by-layer assembled antisense DNA microsponge particles

By first layering with PLL to condense the polymeric antisense DNA, we can achieve a favorable size for cellular uptake, while maintaining a highly concentrated polymeric ODN nanoparticle core for enhanced drug delivery. Additional functional moieties can be incorporated onto these structures *via* LbL assembly to create an outer shell around the core, including the incorporation of polyions that provide the appropriate charge and hydration to achieve desirable biodistribution, and the introduction of targeting moieties. In order to use the power of DNA as a generic layering material in an LbL system, we used a short length of synthetic ssDNA (30 bases) for the second layer. Owing to the high positive charge density of the PLL/ODN core nanoparticles, a negatively charged short ssDNA structure was readily adsorbed onto the particles through electrostatic interaction. The resulting DNA-layered PLL/ODN particle (referred to as ODN-MS/PLL/DNA) was then assembled again with linear polyethylenimine (PEI), which is an effective endosomal escape agent,[52] as the third layer (referred to as ODN-MS/PLL/DNA/PEI). The particle surface charge (ζ-potential) and hydrodynamic size (DLS) of LbL-ODN particles were characterized. The particle surface charge was inverted during each layering step, indicating that the additional layer was constructed in a stepwise fashion followed by alternating electrostatic interactions. Initially, the ODN-MSs were layered at 3 mg/mL PLL, resulting in a positive surface charge (+32.4 ± 1.6 mV). These positively charged particles were used for *in vitro* studies in which the charge facilitates cell entry; whereas, *in vivo* experiments used a final neutral PEG outer layer for blood stream stability and to create a stable stealth layer. The assembly of short

ssDNA strands onto the PLL/ODN particle was successfully achieved by electrostatic adsorption, resulting in a shift in ζ-potential to -23.0 ± 1.4 mV (**Fig. 5A**). Similarly, a positive ζ- potential from the ODN-MS/PLL/DNA/PEI verified PEI self-assembly onto the ODN-MS/PLL/DNA particles (**Fig. 5A**). The size of the ODN-MS/PLL/DNA/PEI particles was 223 ± 8.6 nm in diameter following deposition of three layers onto the ODN-MSs (**Fig. 5B**). Based on their sizes and structures, we termed these nanoscale and polymer-layered particles as LbL-ODN nanoparticles (**LbL-ODN-NPs**). These LbL-ODN-NPs were further examined using SEM and TEM. Images of ODN-MS/PLL/DNA/PEI also show well dispersed particles with a diameter of ~200 nm, which is compatible with the DLS results (**Fig. 5C-E**). In comparison to earlier LbL-based DNA encapsulation papers[53,54] we find that: 1) the ODN-MS system can incorporate a polymeric form of functional DNA (extremely large amounts of functional ODN unit per molecules) rather than just plasmid DNA, 2) improve therapeutic nucleic acid loading efficiencies, 3) can be adapted to undergo particle size changes from micro- to nanometer in scale during condensation for favorable biological applications (*e.g.*, drug delivery).

Intracellular and *in vivo* delivery of layer-by-layer assembled antisense DNA microsponge particles

In the next step, we analyzed the biological functions of LbL-ODN-NPs in terms of intracellular delivery and polymeric ODN drug delivery efficiency. To evaluate the genetic function of polymeric ODN, we performed *in vitro* investigation of the cellular uptake, knockdown efficiency, and cell viability. In order to investigate the efficacy of polymeric ODN delivery *in vitro*, we prepared various types of Cy5-labeled LbL-ODN-NPs by varying multilayer number and corresponding surface charge. The synthesized nanoparticles were transfected into cancer cells (*e.g.*, SKOV3) to observe the extent of cellular uptake. Confocal microscopy results indicated that LbL-ODN-NPs were successfully delivered into the cells (3 h, complete medium) (**Fig 6A**). Moreover, cellular uptake of ODN-MS/PLL/DNA/PEI particles in SKOV3 cells was qualitatively greater than that of the uncondensed ODN-MS, suggesting that their larger size and net negative surface charge inhibits efficient transfection. Cellular uptake was attributed to ATP-mediated endocytosis because very low fluorescence signal was observed within the cells

following incubation at 4°C. We further investigated the cellular uptake of LbL-ODN-NPs by measuring fluorescence intensity of dye-labeled particles using flow cytometry (FACS) (**Fig 6B**). Similar trends in cellular uptake were observed from FACS, validating the confocal microscopy observations. Particles with a positively charged outer surface layer (both ODN-MS/PLL/DNA/PEI and ODN-MS/PLL) exhibited greater cellular uptake, as anticipated, due to charge interactions and nonspecific cell uptake. Moreover, these architectures formed stable structures after four successive layers (ODN-MS/PLL/DNA/PEI) and exhibited significant uptake because of the intrinsic polycationic properties of PEI (**Supplementary Fig. 8**). These results suggest that employment of appropriate layer numbers and selection of biomaterials play a key role in LbL-ODN-NP cellular delivery. We also performed *in vitro* gene knockdown to examine the therapeutic efficiency of LbL-ODN-NPs (*e.g.*, ODN-MS/PLL/DNA/PEI). As a proof of concept, we chose firefly luciferase as a genetic target of interest. Measurement of the luciferase intensity after transfection indicated a substantial inhibition of gene expression (45.7 ± 6.8 %) due to the silencing effect of polymeric ODN from ODN-MS/PLL/DNA/PEI (**Fig. 6C**). Compared to conventional lipid-based transfection strategies (*e.g.*, lipofectamine), knockdown from polymeric ODN showed ~50 fold improved efficiency relative to knockdown from ODN with lipofectamine in terms of the treated ODN concentration. Cell viability after treatment with ODN-MS/PLL/DNA/PEI was also measured by the MTT assay, indicating low toxicity particles (**Supplementary Fig. 9**). We expect that polymeric ODN delivery after LbL assembly will result in improved therapy due to augmented nuclease stability, high drug loading, efficient delivery, and low cytotoxicity.

Owing to the rapid clearance of short ODN with a short plasma half-life *in vivo* (less than ~5 min), it is highly important to establish improved *in vivo* stability of ODN. Assessment of LbL as a means to stabilize ODN was performed by fluorescent modification of the polycationic component (PLL) of the film with a near-infrared dye (Cy5.5) to generate dye-labeled LbL-ODN-NPs, specifically ODN-MS/PLL-Cy5.5/DNA (2L) and ODN-MS/PLL-Cy5.5/DNA/PEI/DNA (4L) nanoparticles were constructed to examine the biodistribution of particles with net negative charge based on the non-specific synthetic DNA outer layer. For a more general outer stealth layer using a well-reported neutral protective hydrophilic polymer in circulation, polyethylene glycol

(PEG)[55] was also incorporated in the final layer of LbL-ODN-NPs using a block copolymer with a negative charged polymer and PEG (*e.g.*, PEG-b-poly-L-glutamic acid), referred to ODN-MS/PLL/DNA/PEI/PEG (PEG). The biological performance of these systems was compared in immune-proficient BALB/c mice by whole-animal fluorescence imaging up to 48 h after IV injection. As shown in Figure 3E, the structure of the ODN alone was not suitable for *in vivo* drug delivery due to the rapid clearance of this therapeutic. The ODN-MS/PLL/DNA/PEI/DNA (4L) showed improved biological performance relative to nanoparticles with ODN-MS/PLL/DNA (2L) (**Fig. 6D and Supplementary Fig. 10**). The ODN-MS/PLL/DNA/PEI/PEG (PEG) nanoparticles also showed longer blood circulation persistence with additional layering and steric stabilization by PEG. Both the 4L and PEG constructs from this study were observed to be good packaging systems for the polymeric ODN construct. The results from *in vivo* fluorescence recovery from live-animal bleeds for blood circulation determination were further substantiated by tissue necropsy (**Supplementary Fig. 10**). Reduced renal clearance was also observed with additional outer layers (4L and PEG) implying the protective effect of the polymeric ODN molecule cores due to the presence of additional layers for extended circulation profiles. Moreover these LbL-ODN-NPs showed a significantly prolonged and a broad range of controlled plasma half-life in comparison to the currently used chemically modified ODNs (*e.g.*, the phosphorothioate (PS) linkages in ODNs and the 2'-*O*-methoxyethyl (MOE) modified ODNs: less than 2~4 h compared to the LbL-ODN-NPs 19~25 h.[3,56] In addition different biodistribution tendencies were obtained when compared to the layered particles (Supplementary Fig. 10). We monitored the accumulation of the engineered LbL-ODN-NPs in five major organs by *ex vivo* fluorescence images at 24 h post-injection. The kidney and liver were the primary organs of LbL-ODN-NPs accumulation, however these compounds were also distributed widely throughout the body. A certain level of quantified fluorescence signal from liver (~22% ID/g) was also detected within 24 h after LbL-ODN-NPs systemic injection. This system compares similarly to other reported nanoparticle systems with regard to biodistribution and liver accumulation, including LbL particles[43,45] and pegylated liposome.[57] Furthermore, we emphasize that the DNA-based LbL-assembled nanoparticle system (*e.g.*, ODN-MS/PLL/DNA/PEI/DNA) can be used in systemic delivery applications

because of its improved stability for longer periods of time *in vivo*. Taken together, these improved biological performances were attributed to the selection of appropriate biomaterial candidates for tuning the surface properties of the ODN nanoparticles, the stability of inherent polymeric ODN, and the use of stabilizing LbL architectures. Further modification of the outer layers can be achieved for specific tumor types using targeting moieties, as we have shown with other LbL nanoparticle systems.[43,45,58,59]

CONCLUSIONS

Our work on DNA-based LbL-ODN nanoparticle systems is unique in terms of the use of polymeric DNA as a therapeutic agent, LbL assembly, and functionalization. This study successfully demonstrates the synthesis of DNA-based microsponge particles that contain highly concentrated polymeric nucleic acids (*e.g.,* ODN) and magnesium pyrophosphate crystals. Furthermore, this report demonstrates specific condensation processes to package large amounts of polymeric ODN within a nanoparticle core. Unlike conventional ODN-loading process with lipids and polymers, ODN-MSs require an additional procedure to disrupt their inorganic structure and reassemble into nano-sized polycation complexes. This new approach allows the encapsulation of polymeric DNA-based molecules such as ODN for therapeutic purposes for efficient drug loading and delivery. Moreover, by employing LbL assembly onto the condensed ODN-MSs, fine-tuning of their multifunctional properties can be achieved for imaging, and tunable surface charge, resulting in an improved intracellular uptake and therapeutic efficacy with a negligible cytotoxicity. This platform possesses multi-functionality because of the selection of appropriate biomaterials, which include PLL, DNA, PEI, and PEG. In addition, this electrostatically assembled multi-layered nucleic acid delivery system provides enhanced pharmacokinetic stability by manipulating surface chemistry and the number of particle layers, allowing for efficient systemic delivery. Because the layering of LbL-ODN-NPs system can be modularly and precisely controlled, further modification of the particles multi-functionality is possible for other applications by rationally combining biofunctional polyelectrolytes along with DNA. Our group is extensively investigating further systemic applications in cancer therapy and their efficacy towards specific diseases and tumor targets. This DNA-based modular

platform approach offers the promise of a potent delivery method for nucleic acid therapeutics for cancer treatment.

METHODS

Circular DNA template design

The circularized ssDNA was used as a template for RCA. To prepare oligonucleotide sequences, linear ssDNA (91 bases) was designed to be comprised of a sequence complementary to the antisense sequence (red color in Fig S1 indicates a region for firefly luciferase targeting), a sequence complementary to the primer ssDNA sequence (blue color in Fig S1 indicates two hybridization regions with primer ssDNA), and a linker sequence (black color in Fig S1). The primer ssDNA contains two hybridization regions with linear ssDNA (one portion with 16 bases at the 5' end and another portion with 6 bases at the 3' end).

Preparation of circular DNA template

Phosphorylated linear ssDNA (91 bases, 500 nM) containing two complementary sequence regions with a primer ssDNA strand (22 bases) was annealed to form circular DNA template. Two ssDNA strands were hybridized with an equal molar ratio by heating at 95°C for 2 min and cooling down to 24°C gradually over 1 hour. The nick between the circular DNA was chemically connected by T4 DNA ligase (1 unit/μl) in the ligase buffer (30 mM Tris-HCl, pH 7.8, 10 mM $MgCl_2$, 10 mM DTT, 1 mM ATP) followed by the incubation at 24°C for 4 h.

Synthesis of antisense DNA microsponge

To construct antisense DNA microsponge (ODN-MS), circular DNAs (300 nM) were mixed with *ϕ29* DNA polymerase (5 units/μl) and deoxyribonucleotide tri-phosphate (2 mM) in the reaction buffer (40 mM Tris-HCl (pH 7.5), 50 mM KCl, 10 mM $MgCl_2$, 5 mM $(NH4)_2SO_4$, and 4 mM dithiothreitol), and then allowed to proceed at 24°C for 24 h for the RCA process. To synthesize the fluorescently-modified ODN-MS, Cyanine 5-UTP was additionally added to final concentration of 0.5 mM during the RCA reaction. For the polymeric ODN staining in ODN-MS, ssDNA-specific dye (SYBR II)

was used after particle generation by following the manufacturer's instruction. The resultant product was sonicated and pipetted multiple times until the particle products were well dispersed. The solution was then centrifuged at 8000 rpm for 5 min to collect the ODN-MS product. DNase-free water was used for additional washing steps to eliminate the reagents of RCA.

Gel electrophoresis

The molecular weight of polymeric DNAs and the stability of polymeric DNAs were characterized by gel electrophoresis. Agarose and TB buffer were mixed to a specific percent (0.5-2 %) according to a weight of agarose/volume of buffer ratio (wt/vol). Mixture was heated in microwave for 1 min and then GelRed™ gel stain was added. The solution was immediately poured into rack and allowed to solidify for 20 min. The solidified gel in rack was transferred to gel running apparatus which was filled with TB buffer. DNA samples were prepared with a bromophenol blue containing gel loading dye by following the manufacturer's protocol (New England Biolabs, Ipswich, MA) and then loaded into gel. Gel electrophoresis was conducted at 70 (V/cm) for 60-80 (min). Gel images were visualized using UV transilluminator (Bio-Rad, Hercules, CA).

Measurement of the polymeric DNA concentration

Polymeric DNA structures were prepared by the addition of EDTA (50 mM), a strong Mg^{2+} scavenger, because of the disruption of polymeric DNA/inorganic composite structures of ODN-MS. The concentration of polymeric ssDNA and short ssDNA (ODN control) were measured according to manufacturer's instructions for Quant-iT™ OliGreen® ssDNA Assay Kit (Life Technologies, Carlsbad, CA). Briefly polymeric DNA or standard solution (10 µl) were mixed well with Quant-iT OliGreen® ssDNA reagent (190 µl) by pipetting. Then the mixtures were placed into a Corning® Clear Flat Bottom 96-wells plate and incubated for 5 min at 24°C. Fluorescence (λex = 480 nm, λem = 520 nm) was measured using a fluorescence microplate reader (Tecan Infinite® 200 PRO). The concentration of polymeric DNAs was determined by comparing with an ODN standard curve of fluorescence intensity versus concentration.

Stability experiments of polymeric DNA structures

The DNA stability in serum and enzyme was analyzed by measuring the band intensities of each polymeric DNA/short DNA band in agarose gel electrophoresis. To perform serum stability test, 150 ng of polymeric DNA structures and short DNAs were incubated with 50% human serum for 3 days, 2 days, 1 day, 12 h, and 3 h. Samples were loaded into 2% agarose gel along with untreated samples of 50, 100, and 150 ng amounts as reference. Gel electrophoresis was performed at 70V for 60 min. To perform DNase stability test, 150 ng polymeric DNA structures and short DNAs were incubated with DNase (3 units/μL) and reaction buffer. Samples were incubated for 3 days, 2 days, 1 day, 12 h, 3 h, 2 h, 90 min, 60 min, and 30 min. Samples were loaded into 2% gel along with untreated samples of 50, 100, and 150 ng amounts as reference. Gel electrophoresis was conducted at 70V for 60 min. Image J densiometry analysis was processed to calculate the degradation amount (wt %) of polymeric DNA/short ssDNA.

To perform *in vivo* pharmacokinetics study, Cy5 dye-labeled polymeric ssDNA and short ssDNA were prepared. Female NCr nude mice were treated with Cy5 dye-labeled polymeric ssDNA or Cy5 labeled short ssDNA. Fluorescence intensity (λex = 640 nm, λem = 700 nm) of dye-labeled DNA was measured from *in vivo* imaging systems (Xenogen IVIS® Imaging System 200, Caliper Life Sciences, Hopkinton, MA).

Characterization of ODN-MSs and LbL-ODN-NPs

Scanning electron microscopy (JEOL JSM-6700F, JSM-6070, and JSM-6060) was utilized to obtain high-resolution digital images of the ODN-MSs, condensed nanoparticles, and LbL-ODN-NPs. Samples were prepared by placing aqueous suspensions onto silicon wafers. Images were acquired without an additional metal coating at an accelerating voltage of 2 kV.

Transmission electron microscopy (JEOL 2010 and 2000FX) was utilized to observe the internal structure of the ODN-MSs and LbL-ODN-NPs. Images were obtained at an accelerating voltage of 200 kV.

Fluorescent microscopy (Zeiss AxioSkop 2 MAT) and confocal microscopy (Nikon 1AR Spectral Scanning Confocal Microscope) were used to confirm the presence of polymeric ssDNA product in the ODN-MSs generated by the RCA. After particles

formation through RCA, the ODN-MSs were stained with the ssDNA-specific dye (SYBR II) by following the company's instruction (Lonza, Walkersville, MD). Green-fluorescently stained ODN-MSs were then observed by fluorescent microscopy. Another DNA visualization method was used by adding fluorescently-labeled deoxyribonucleotide (Cyanine 5-dUTP or Fluorescein) during RCA process. Confocal microscopy was then utilized to visualize the localization of DNA within microsponges. The progression of condensation was also monitored by confocal microscopy. To prepare dual-labeled fluorescence system for this observation, Fluorescein-12-dUTP (corresponding to green color) was used to construct dye-labeled ODN-MSs during RCA synthesis. Cyanine 5.5 (corresponding to red color) conjugated poly-L-lysine (PLL) (Mw 25000 g/mol) was prepared by following the previously published protocols.[45] The progression from microsponge to polyelectrolyte complexation was observed *via* confocal microscopy at varied concentrations of dye-PLL.

The elemental composition of the ODN-MS microstructures and the condensed nanoparticles were investigated in detail using scanning transmission electron microscopy (JEOL 2010F) equipped with an analytical scanning imaging device (ASID) and an INCA energy dispersive X-ray spectroscopy (EDX) detector. Elemental mapping was carried out using a 1 nm probe.

Powder X-ray diffraction (PXRD) was used to analyze the crystalline structure of ODN-MSs and condensed nanoparticles. Samples for PXRD were prepared by placing aqueous suspensions onto copper (Cu) tapes. Data collection proceeds were achieved using a Rigaku rotating anode X-Ray powder diffractometers. PXRD patterns were recorded from 5 to 40° 2Θ in a parallel beam configuration fitted with a 9 kW rotating anode copper source.

Condensation and layer-by-layer assembly on ODN-MS

The condensation process of ODN-MS is properly applied to improve the delivery efficiency of polymeric DNA. The cationic polymers including PLL or PEI can be used as polymeric condensing agents by means of strong ionic interactions with negatively charged ODN-MS. To find out the optimal conditions for condensation, the polymer stock solution (*e.g.*, PLL, Mw 25000 g/mol, 5.0 mg/ml) was added into the ODN-MS

solution at varied concentrations (0.1 - 5 mg/mL). Then the mixtures were gently mixed for 4 h. Access amount of free polymer in the supernatant was discarded by following the centrifugation at 12000 rpm for 5 min. The condensed particles were then resuspended in PBS solution and repeated washing steps twice.

For assembly of the additional layering, the variety of polymer stock solution such as PEI (Mw 25000 g/mol, 5.0 mg/ml), ssDNA (Mw 8000 g/mol, 5.0 mg/ml), and PEG-PGA (Mw 13000 g/mol, 5.0 mg/ml) were prepared separately. The condensed particles were mixed with each polymer stock solution and then allowed 4 h gentle mixing. Access amount of unreacted free polymer in the supernatant was removed by following the centrifugation at 12000 rpm for 5 min. The resultant layered particles were then resuspended in PBS solution and allowed an additional washing. This layering step could be repeated until the pre-defined layering numbers of LbL-ODN-NPs were achieved.

Characterization of LbL-ODN-NPs

Dynamic Light Scattering (DLS) and Zeta Potential

The surface charge and size of ODN-MSs and LbL-ODN-NPs were measured using zeta-potential and dynamic light scattering (DLS) instruments (Malvern Nano-ZS90 zetasizer, Westborough, MA). The particles were diluted in Milli-Q water and three measurements were performed per each sample at 24°C.

Intracellular uptake study

Cellular uptake of LbL-MS-NPs and ODN-MS was examined by confocal microscopy and flow cytometry. SKOV3 cells (1 x 10^5 cells) in suspension media were seeded in CELLview glas bottom dish (Greiner Bio-One GmbH, Germany) per well and maintained for 24 h. The Cy5.5 fluorescently labeled LbL-ODN-NPs or ODN-MS was added in each well in the presence of DPBS (Life Technologies, Carlsbad, CA) and then incubated for 3 h at 37°C or 4°C. At the end period of incubation, cells were washed three times with PBS and fixed with 4% paraformaldehyde. For fluorescence imaging, cells were permeabilized in 0.1% Triton X100 for 10 min and stained Alexa Fluor 488-phalloidin (Invitrogen, Carlsbad, California) and nuclei were stained with DAPI (40,6-

diamidino-2-phenylindole). An antifade reagent (Invitrogen, Carlsbad, California) was added according to the manufacturer's protocol. Fluorescent images of the cells were acquired using confocal microscope (Nikon 1AR Spectral Scanning Confocal Microscope, Melville, NY).

The quantity of uptake was obtained by flow cytometry. SKOV3 cells (2 x 10^4 cells) in suspension media were seeded in a 96-well plate and maintained for 24 h. The Cy5.5 fluorescently labeled LbL-ODN-NPs or ODN-MS (100 μg/mL) was treated in each well in the presence of DPBS (Life Technologies, Carlsbad, CA) and then incubated for various periods of times at 37°C. The cell-associated fluorescence was determined by flow cytometer (BD LSRFortessa™) equipped with a BD™ high throughput sampler (HTS) for the 96-well plate format and analyzed by BD FACSDiva™ software (BD Biosciences, Franklin Lakes, NJ).

***In vitro* knockdown experiments and cell proliferation assays**

SKOV3-LUC/SKOV3 cells were used in *in vitro* knockdown evaluation and cell proliferation assay. Cells were maintained in growth media consisting of Minimum Essential Media-Alpha (MEM-α), 10% fetal bovine serum (FBS), and 1% penicillin–streptomycin. Stable both firefly and renilla luciferase-overexpressing SKOV3 cells were prepared using lentivirus vectors according to the manufacturer's protocols (Cell Biolabs, San Diego, CA).

For sample preparations, the antisense strand of firefly luciferase sequences were obtained from Ambion (Austin, TX). ODN-MSs and LbL-ODN-NPs were prepared as aforementioned procedures. The samples were diluted in DPBS (Life Technologies, Carlsbad, CA) to 10 μL final volumes for each ODN amount. The amounts of ODN-MSs and LbL-ODN-NPs were normalized to the concentration of ODN loading. A single-stranded ODN control (~22 bases) with the conventional transfection reagent (i.e. lipofectamine®, Invitrogen, Carlsbad, CA) was used as a positive control. As suggested by the company, the 1:3 ratio (w/v) of a single-stranded ODN / lipofectamine (ODN/Lipo) was used to form liposome. SKOV3 cells (2 x 10^4) were seeded in each well of a 96-wells plate and maintained. After 24 h, the MEM-α media was replaced with DPBS. The cells were treated with prepared ODN samples (10 μL) of ODN-MSs, LbL-

ODN-NPs, and ODN/Lipo at varied ODN amounts were treated to the cells and then gently mixed. The cells were incubated in the controlled-temperature at 37 °C with 5% CO_2 incubator for 4 h. After 4 h of transfection DPBS was replaced with MEM-α. Both knockdown and cell proliferation evaluations were carried out after 48 h additional incubation.

For firefly luciferase silencing evaluation, the luciferase assay was performed using the Dual-Glo Luciferase Assay Kit (Promega, Madison, WI) as the kit's protocol and luminescence was measured using a microplate reader (Tecan Infinite® 200 PRO). Transfections were conducted in quadruplicate. The level of firefly luciferase silencing (%) from each sample was obtained by comparing the luminescence value from *renilla luciferase*.

The cell proliferation was evaluated using CCK-8 kit (Dojindo Molecular Technologies, Rockville, MD) following the manufacturer's protocols. Briefly, CCK-8 reagent solution (10 μL) was directly added to the each well of the plate and then the plate was incubated for 1 h at 37°C. The amount of a water-soluble formazan (a yellowcolored product) was determined by the absorbance value at 450 nm using a microplate reader (Tecan Infinite® 200 PRO). The cell proliferation (%) of each sample was determined using the absorbance value of a prepared calibration curve that contains given numbers of viable cells (untreated control).

***In vivo* biodistribution experiments**

Female NCr and BALB/c nude mice (4-6 weeks old, Taconic, Hudson, NY) were used for biodistribution experiments. Mice fed on the alfalfa-free special diet (AIN-93M Maintenance Purified Diet from TestDiet®) for a week before and during experimentation to reduce the body autofluorescence level. All animal care and *in vivo* experimental procedures were performed following institutionally approved protocols and regulations (MIT Department of Comparative Medicine and NIH Principles of Laboratory Animal Care).

Biodistribution of LbL-ODN-NPs clearance was investigated in BALB/c nude mice *via* intravenous administration (*e.g.*, tail vein injection). The Cy 5.5-labeled LbL-ODN-NPs suspended in PBS were administered at the ODN concentration of 1.0 mg/kg

in 0.1mL injection volume. Whole-animal fluorescence images are obtained ventrally at the preassigned time points using IVIS® whole-animal imaging system with Living Image® software (Xenogen, Caliper Instruments) to measure the circulation serum half-life of the control ssDNA, polymeric DNA, and LbL-ODN-NPs. Imaging and circulation data were captured using fluorescent overlay (λex = 640 nm, λem = 700 nm) and fitted with a 2-phase decay model (PRISM®) with both slow and fast half-lives presented. For blood circulation persistence analysis of LbL-ODN-NPs, the existence of particles in blood was quantified with the Licor Odyssey system by measuring percent fluorescence recovery from collected blood samples taken after IV administration.

Statistical analysis

All data represent mean values with standard deviation (SD) from three independent measurements. Statistical analysis between different treatments was processed by a Student's *t* test. Statistical significance was assigned for $p < 0.05$ (95% confidence level).

Supporting Information Available: Additional results, materials, methods, and DNA nanostructure design schematic and oligonucleotide sequences are available as Supporting Information. This material is available free of charge *via* the internet at http://pubs.acs.org.

Acknowledgment

We gratefully acknowledge the funding of this work from the DoD OCRP Teal Innovator Award. We thank the MIT Koch Institute Swanson Biotechnology Center, which is supported by the Koch Institute Core Grant P30-CA14051 from the NCI, for the use of facilities, and specifically the microscopy and the flow cytometry cores. This work made use of the MIT MRSEC Shared Experimental Facilities supported by the National Science Foundation under award number DMR-0819762. K.E.S. thanks a National Sciences and Engineering Research Council (NSERC) postdoctoral fellowship. E.C.D. acknowledges postdoctoral fellowship support from the NIH (Kirschstein NRSA 1F32EB017614-01). S.W.M. thanks a National Science Foundation Graduate Research

Fellowship (NSF GRF). We thank Dr. Mohi Quadir and Dr. Jason Deng for technical support on experiments.

Affiliations

Dr. Y. H. Roh, Prof. J. B. Lee,[++] Dr. K. E. Shopsowitz, Dr. E. C. Dreaden, S. W. Morton, Dr. Z. Poon, Prof. J. Hong, I. Yamin, Dr. D. K. Bonner, and Prof. P. T. Hammond∗

Department of Chemical Engneering, Massachusetts Institute of Technology, Cambridge, MA 02139 (USA)
The Koch Institute for Integrative Cancer Research at MIT, Cambridge, MA 02139 (USA)
[∗] Address correspondence to Hammond@mit.edu
[++] Current Address: Department of Chemical Engineering, University of Seoul, Seoul, 130-743 (South Korea)
[+] These authors contributed equally to this work.

Figure legends

Figure 1. Design of the multifunctional DNA-based layer-by-layer assembled nanoparticle. Schematic illustration of the construction of multifunctional nanoparticle using three important strategies including the synthesis of antisense microsponge particles (**ODN-MS**), condensation process, and layer-by-layer assembly. A self-assembled microsponge-like structure of DNA containing a large amount of periodic antisense oligodeoxynucleotide (ODN) strand in the form of a long polymeric ssDNA was synthesized using rolling circle amplification (RCA) (**Step 1**). During condensation, ODN-MS were totally disrupted and then reconstructed into nano-sized polyplexes by complexation with a selected polymer (**Step 2**). Next, keeping this complexation as the core, additional outer layer shells were formed through Layer-by-Layer (LbL) assembly technique (**Step 3**). Finally, these LbL-ODN nanoparticles (**LbL-ODN-NPs**) possessed multi-functionality due to the power of both functional DNA nanostructure and LbL assembly method.

Figure 2. Structural characterization of antisense microsponge particle A-B) SEM images of ODN-MS. Scale bars indicate 5 μm (**A**) and 1 μm (**B**), respectively. **C-D**) TEM images of ODN-MS observed at low and higher magnification. Scale bars indicate

500 nm (**C**) and 100 nm (**D**), respectively. **E-F**) Confocal microscopy images of ODN-MS, which was functionalized with Cy5-conjugated dUTP during the RCA process (red color). ODN-MS viewed at top point (**E**) and in the middle section (**F**). Scale bars indicate 1 μm.

Figure 3. Characterization of polymeric DNA after extraction from antisense microsponge particle A) SEM images of ODN-MS before and after EDTA treatment. Scale bars indicate 500 nm. **B)** Gel electrophoresis analysis to verify the size of polymeric DNA disrupted by EDTA. Lane 1-2 indicate 1 kb and 5 kb DNA ladder, respectively. **C)** Serum stability of polymeric DNA (top) and short ssDNA (bottom) after a pre-assigned incubation time in a 50% serum medium. **D)** Enzyme stability of polymeric DNA (top) and short ssDNA (bottom) after a pre-assigned incubation time in DNase (3 units/μL) at 37°C. **E)** *In vivo* stability of polymeric DNA and short ssDNA. Biodistribution of polymeric DNA (top) and short ssDNA (bottom) prior to injection followed by 5 and 30 min post-injection in NCr nude. Images are representative of a photograph with fluorescent overlay (λex = 640 nm, λem = 700 nm).

Figure 4. Characterization of polymeric DNA packaging by condensing process A-C) SEM images of ODN-MS before condensing process (**A**) and after condensation with varying concentrations of PLL (**B**-**C**). Scale bars indicate 1 μm. SEM images show the reduced size of condensed nanoparticles with changed morphology. **D-G**) Confocal microscopy images of ODN-MS after condensation with varying concentrations of PLL. Dual labeling was applied in this observation. PLL was functionalized with Cy5 (red color) and DNA was stained with SYBR II, ssDNA specific dyes (green color). Magnification was 60x and scale bars indicate 5 μm. **H**) Size of ODN-MS/PLL at varied concentrations of condensing polymer. **I**) ζ Potential of ODN-MS/PLL at varying concentrations of condensing polymer.

Figure 5. Properties of layer-by-layer assembled antisense microsponge particles. A) ζ Potential of ODN-MS, ODN-MS/PLL, ODN-MS/PLL/DNA, and ODN-MS/PLL/DNA/PEI. **B)** Size of ODN-MS, ODN-MS/PLL, ODN-MS/PLL/DNA, and

ODN-MS/PLL/DNA/PEI. **C-D)** SEM images of ODN-MS (**C**) and ODN-MS/PLL/DNA/PEI (**D**). Scale bars indicate 5 μm and 0.5 μm, respectively. **E)** TEM image of ODN-MS/PLL/DNA/PEI. Scale bar indicates 1 μm.

Figure 6. Intracellular and *in vivo* delivery of layer-by-layer assembled antisense DNA microsponge particles. A) Intracellular delivery of layer-by-layer assembled antisense microsponge particles. Confocal microscopy image of cancer cells (*e.g.*, SKOV3) treated with LbL-ODN-NPs. Nanoparticles were labeled red with Cy5. The actin cytoskeleton was stained green with phalloidin and the nucleus was stained blue with DAPI. Scale bars are 10 μm. **B**) Cellular uptake study of LbL-ODN-NPs in cancer cells (*e.g.*, SKOV3) by using flow cytometry analysis. **C**) The knockdown efficiency of target gene expression for firefly luciferase regulation using LbL-ODN-NPs was examined as a function of concentration *in vitro*. **D)** Pharmacokinetics of nanoparticle clearance from IV-administered BALB/c mice with various LbL-ODN-NPs formulations – fit with a 2-phase decay model (PRISM®). ODN-MS/PLL/DNA (2L), ODN-MS/PLL/DNA/PEI/DNA (4L), ODN-MS/PLL/DNA/PEI/PEG (PEG).

REFERENCES

(1) Lee, J. B.; Hong, J.; Bonner, D. K.; Poon, Z.; Hammond, P. T. Self-Assembled RNA Interference Microsponges for Efficient siRNA Delivery. *Nat. Mater.* **2012**, *11*, 316–322.

(2) Shopsowitz, K. E.; Roh, Y. H.; Deng, Z. J.; Morton, S. W.; Hammond, P. T. RNAi-Microsponges Form through Self-Assembly of the Organic and Inorganic Products of Transcription. *Small* **2013**, 1623–1633.

(3) Gleave, M. E.; Monia, B. P. Antisense Therapy for Cancer. *Nat. Rev. Cancer* **2005**, *5*, 468–479.

(4) Tamm, I.; Dörken, B.; Hartmann, G. Antisense Therapy in Oncology: New Hope for an Old Idea? *Lancet* **2001**, *358*, 489–497.

(5) Bennett, C. F.; Swayze, E. E. RNA Targeting Therapeutics: Molecular Mechanisms of Antisense Oligonucleotides as a Therapeutic Platform. *Annu. Rev. Pharmacol. Toxicol.* **2010**, *50*, 259–293.

(6) Kole, R.; Krainer, A. R.; Altman, S. RNA Therapeutics: Beyond RNA Interference and Antisense Oligonucleotides. *Nat. Rev. Drug Discov.* **2012**, *11*, 125–140.

(7) Crooke, S. T. Progress in Antisense Technology. *Annu. Rev. Med.* **2004**, *55*, 61–95.

(8) Geary, R. S.; Watanabe, T. A.; Truong, L.; Freier, S.; Lesnik, E. A.; Sioufi, N. B.; Sasmor, H.; Manoharan, M.; Levin, A. A. Pharmacokinetic Properties of 2'-O-(2-Methoxyethyl)-Modified Oligonucleotide Analogs in Rats. *J. Pharmacol. Exp. Ther.* **2001**, *296*, 890–897.

(9) Zellweger, T.; Miyake, H.; Cooper, S.; Chi, K.; Conklin, B. S.; Monia, B. P.; Gleave, M. E. Antitumor Activity of Antisense Clusterin Oligonucleotides Is Improved in Vitro and in Vivo by Incorporation of 2'-O-(2-Methoxy)ethyl Chemistry. *J. Pharmacol. Exp. Ther.* **2001**, *298*, 934–940.

(10) Geary, R. S.; Yu, R. Z.; Watanabe, T.; Henry, S. P.; Hardee, G. E.; Chappell, A.; Matson, J.; Sasmor, H.; Cummins, L.; Levin, A. A. Pharmacokinetics of a Tumor Necrosis Factor-A Phosphorothioate 2'-(O-Methoxyethyl) Modified Antisense Oligonucleotide: Comparison Across Species. *Drug Metab. Dispos.* **2003**, *31*, 1419–1428.

(11) Deleavey, G. F.; Watts, J. K.; Damha, M. J. Chemical Modification of siRNA. *Curr. Protoc. Nucleic Acid Chem.* **2009**, *Chapter 16*, Unit 16.3.

(12) Chauhan, V. P.; Jain, R. K. Strategies for Advancing Cancer Nanomedicine. *Nat. Mater.* **2013**, *12*, 958–962.

(13) Hubbell, J. A.; Langer, R. Translating Materials Design to the Clinic. *Nat. Mater.* **2013**, *12*, 963–966.

(14) Luo, D.; Saltzman, W. M. Synthetic DNA Delivery Systems. *Nat. Biotechnol.* **2000**, *18*, 33–37.

(15) Petros, R. A.; DeSimone, J. M. Strategies in the Design of Nanoparticles for Therapeutic Applications. *Nat. Rev. Drug Discov.* **2010**, *9*, 615–627.

(16) Juliano, R.; Bauman, J.; Kang, H.; Ming, X. Biological Barriers to Therapy with Antisense and siRNA Oligonucleotides. *Mol. Pharm.* **2009**, *6*, 686–695.

(17) Peer, D.; Karp, J. M.; Hong, S.; Farokhzad, O. C.; Margalit, R.; Langer, R. Nanocarriers as an Emerging Platform for Cancer Therapy. *Nat. Nanotechnol.* **2007**, *2*, 751–760.

(18) Wang, A. Z.; Langer, R.; Farokhzad, O. C. Nanoparticle Delivery of Cancer Drugs. *Annu. Rev. Med.* **2012**, *63*, 185–198.

(19) Albanese, A.; Tang, P. S.; Chan, W. C. W. The Effect of Nanoparticle Size, Shape, and Surface Chemistry on Biological Systems. *Annu. Rev. Biomed. Eng.* **2012**, *14*, 1–16.

(20) Pinheiro, A. V; Han, D.; Shih, W. M.; Yan, H. Challenges and Opportunities for Structural DNA Nanotechnology. *Nat. Nanotechnol.* **2011**, *6*, 763–772.

(21) Seeman, N. C. DNA in a Material World. *Nature* **2003**, *421*, 427–431.

(22) Feldkamp, U.; Niemeyer, C. M. Rational Design of DNA Nanoarchitectures. *Angew. Chem. Int. Ed. Engl.* **2006**, *45*, 1856–1876.

(23) Aldaye, F. A.; Palmer, A. L.; Sleiman, H. F. Assembling Materials with DNA as the Guide. *Science* **2008**, *321*, 1795–1799.

(24) Roh, Y. H.; Ruiz, R. C. H.; Peng, S.; Lee, J. B.; Luo, D. Engineering DNA-Based Functional Materials. *Chem. Soc. Rev.* **2011**, *40*, 5730–5744.

(25) Wilner, O. I.; Willner, I. Functionalized DNA Nanostructures. *Chem. Rev.* **2012**, *112*, 2528–2556.

(26) Bhatia, D.; Surana, S.; Chakraborty, S.; Koushika, S. P.; Krishnan, Y. A Synthetic Icosahedral DNA-Based Host-Cargo Complex for Functional in Vivo Imaging. *Nat. Commun.* **2011**, *2*, 339.

(27) Walsh, A. S.; Yin, H.; Erben, C. M.; Wood, M. J. A.; Turberfield, A. J. DNA Cage Delivery to Mammalian Cells. *ACS Nano* **2011**, *5*, 5427–5432.

(28) Keum, J.-W.; Ahn, J.-H.; Bermudez, H. Design, Assembly, and Activity of Antisense DNA Nanostructures. *Small* **2011**, *7*, 3529–3535.

(29) Lee, J. B.; Roh, Y. H.; Um, S. H.; Funabashi, H.; Cheng, W.; Cha, J. J.; Kiatwuthinon, P.; Muller, D. A.; Luo, D. Multifunctional Nanoarchitectures from DNA-Based ABC Monomers. *Nat. Nanotechnol.* **2009**, *4*, 430–436.

(30) Lee, H.; Lytton-Jean, A. K. R.; Chen, Y.; Love, K. T.; Park, A. I.; Karagiannis, E. D.; Sehgal, A.; Querbes, W.; Zurenko, C. S.; Jayaraman, M.; *et al.* Molecularly Self-Assembled Nucleic Acid Nanoparticles for Targeted in Vivo siRNA Delivery. *Nat. Nanotechnol.* **2012**, *7*, 389–393.

(31) Drmanac, R.; Sparks, A. B.; Callow, M. J.; Halpern, A. L.; Burns, N. L.; Kermani, B. G.; Carnevali, P.; Nazarenko, I.; Nilsen, G. B.; Yeung, G.; *et al.* Human Genome Sequencing Using Unchained Base Reads on Self-Assembling DNA Nanoarrays. *Science* **2010**, *327*, 78–81.

(32) Lee, J. B.; Peng, S.; Yang, D.; Roh, Y. H.; Funabashi, H.; Park, N.; Rice, E. J.; Chen, L.; Long, R.; Wu, M.; *et al.* A Mechanical Metamaterial Made from a DNA Hydrogel. *Nat. Nanotechnol.* **2012**, *7*, 816–820.

(33) Decher, G. Fuzzy Nanoassemblies: Toward Layered Polymeric Multicomposites. *Science (80-.).* **1997**, *277*, 1232–1237.

(34) Krogman, K. C.; Lowery, J. L.; Zacharia, N. S.; Rutledge, G. C.; Hammond, P. T. Spraying Asymmetry into Functional Membranes Layer-by-Layer. *Nat. Mater.* **2009**, *8*, 512–518.

(35) Schneider, G. F.; Subr, V.; Ulbrich, K.; Decher, G. Multifunctional Cytotoxic Stealth Nanoparticles. A Model Approach with Potential for Cancer Therapy. *Nano Lett.* **2009**, *9*, 636–642.

(36) Hammond, P. T. Form and Function in Multilayer Assembly: New Applications at the Nanoscale. *Adv. Mater.* **2004**, *16*, 1271–1293.

(37) Hammond, P. T. Building Biomedical Materials Layer-by-Layer. *Mater. Today* **2012**, *15*, 196–206.

(38) Becker, A. L.; Johnston, A. P. R.; Caruso, F. Layer-by-Layer-Assembled Capsules and Films for Therapeutic Delivery. *Small* **2010**, *6*, 1836–1852.

(39) Hammond, P. Polyelectrolyte Multilayered Nanoparticles: Using Nanolayers for Controlled and Targeted Systemic Release. *Nanomedicine* **2012**, *7*, 619–622.

(40) Boudou, T.; Crouzier, T.; Ren, K.; Blin, G.; Picart, C. Multiple Functionalities of Polyelectrolyte Multilayer Films: New Biomedical Applications. *Adv. Mater.* **2010**, *22*, 441–467.

(41) Elbakry, A.; Zaky, A.; Liebl, R.; Rachel, R.; Goepferich, A.; Breunig, M. Layer-by-Layer Assembled Gold Nanoparticles for siRNA Delivery. *Nano Lett.* **2009**, *9*, 2059–2064.

(42) Cortez, C.; Tomaskovic-Crook, E.; Johnston, A. P. R.; Radt, B.; Cody, S. H.; Scott, A. M.; Nice, E. C.; Heath, J. K.; Caruso, F. Targeting and Uptake of Multilayered Particles to Colorectal Cancer Cells. *Adv. Mater.* **2006**, *18*, 1998–2003.

(43) Poon, Z.; Lee, J. B.; Morton, S. W.; Hammond, P. T. Controlling in Vivo Stability and Biodistribution in Electrostatically Assembled Nanoparticles for Systemic Delivery. *Nano Lett.* **2011**, *11*, 2096–2103.

(44) Poon, Z.; Chang, D.; Zhao, X.; Hammond, P. T. Layer-by-Layer Nanoparticles with a pH-Sheddable Layer for in Vivo Targeting of Tumor Hypoxia. *ACS Nano* **2011**, *5*, 4284–4292.

(45) Morton, S. W.; Poon, Z.; Hammond, P. T. The Architecture and Biological Performance of Drug-Loaded LbL Nanoparticles. *Biomaterials* **2013**, *34*, 5328–5335.

(46) Sexton, A.; Whitney, P. G.; Chong, S.-F.; Zelikin, A. N.; Johnston, A. P. R.; De Rose, R.; Brooks, A. G.; Caruso, F.; Kent, S. J. A Protective Vaccine Delivery System for in Vivo T Cell Stimulation Using Nanoengineered Polymer Hydrogel Capsules. *ACS Nano* **2009**, *3*, 3391–3400.

(47) Shutava, T. G.; Balkundi, S. S.; Vangala, P.; Steffan, J. J.; Bigelow, R. L.; Cardelli, J. A.; O'Neal, D. P.; Lvov, Y. M. Layer-by-Layer-Coated Gelatin Nanoparticles as a Vehicle for Delivery of Natural Polyphenols. *ACS Nano* **2009**, *3*, 1877–1885.

(48) Saul, J. M.; Wang, C.-H. K.; Ng, C. P.; Pun, S. H. Multilayer Nanocomplexes of Polymer and DNA Exhibit Enhanced Gene Delivery. *Adv. Mater.* **2008**, *20*, 19–25.

(49) Blanco, L.; Bernad, A.; Lazaro, J.; Martin, G.; Garmendia, C.; Salas, M. Highly Efficient DNA Synthesis by the Phage Phi 29 DNA Polymerase. Symmetrical Mode of DNA Replication. *J. Biol. Chem.* **1989**, *264*, 8935–8940.

(50) Luo, D. The Road from Biology to Materials. *Mater. Today* **2003**, *6*, 38–43.

(51) Mok, H.; Lee, S. H.; Park, J. W.; Park, T. G. Multimeric Small Interfering Ribonucleic Acid for Highly Efficient Sequence-Specific Gene Silencing. *Nat. Mater.* **2010**, *9*, 272–278.

(52) Boussif, O.; Lezoualc'h, F.; Zanta, M. A.; Mergny, M. D.; Scherman, D.; Demeneix, B.; Behr, J. P. A Versatile Vector for Gene and Oligonucleotide Transfer into Cells in Culture and in Vivo: Polyethylenimine. *Proc. Natl. Acad. Sci.* **1995**, *92*, 7297–7301.

(53) Trubetskoy, V. S.; Wong, S. C.; Subbotin, V.; Budker, V. G.; Loomis, A.; Hagstrom, J. E.; Wolff, J. A. Recharging Cationic DNA Complexes with Highly Charged Polyanions for in Vitro and in Vivo Gene Delivery. *Gene Ther.* **2003**, *10*, 261–271.

(54) Shchukin, D. G.; Patel, A. A.; Sukhorukov, G. B.; Lvov, Y. M. Nanoassembly of Biodegradable Microcapsules for DNA Encasing. *J. Am. Chem. Soc.* **2004**, *126*, 3374–3375.

(55) Harris, J. M.; Chess, R. B. Effect of Pegylation on Pharmaceuticals. *Nat. Rev. Drug Discov.* **2003**, *2*, 214–221.

(56) Geary, R. S.; Watanabe, T. A.; Truong, L.; Freier, S.; Lesnik, E. A.; Sioufi, N. B.; Sasmor, H.; Manoharan, M.; Levin, A. A. Pharmacokinetic Properties of 2'-O-(2-

Methoxyethyl)-Modified Oligonucleotide Analogs in Rats. *J. Pharmacol. Exp. Ther.* **2001**, *296*, 890–897.

(57) Harrington, K. J.; Rowlinson-Busza, G.; Syrigos, K. N.; Uster, P. S.; Abra, R. M.; Stewart, J. S. Biodistribution and Pharmacokinetics of 111In-DTPA-Labelled Pegylated Liposomes in a Human Tumour Xenograft Model: Implications for Novel Targeting Strategies. *Br. J. Cancer* **2000**, *83*, 232–238.

(58) Morton, S. W.; Shah, N. J.; Quadir, M. A.; Deng, Z. J.; Poon, Z.; Hammond, P. T. Osteotropic Therapy via Targeted Layer-by-Layer Nanoparticles. *Adv. Healthc. Mater.* **2013**.

(59) Deng, Z. J.; Morton, S. W.; Ben-Akiva, E.; Dreaden, E. C.; Shopsowitz, K. E.; Hammond, P. T. Layer-by-Layer Nanoparticles for Systemic Codelivery of an Anticancer Drug and siRNA for Potential Triple-Negative Breast Cancer Treatment. *ACS Nano* **2013**, *7*, 9571–9584.

Figure 1

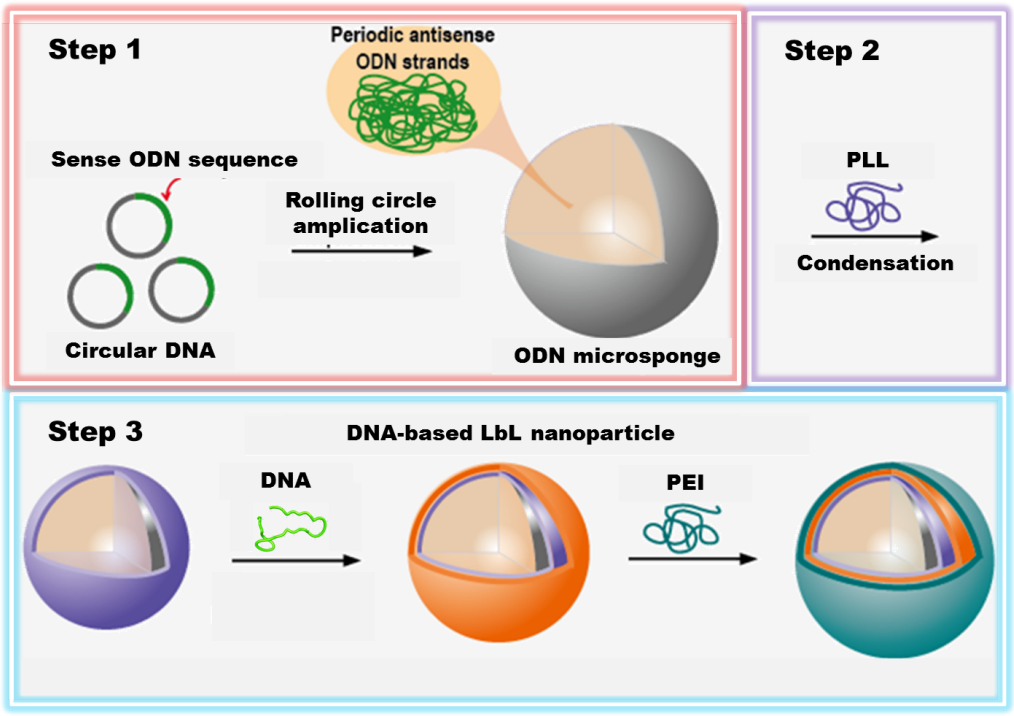
Step 1
Periodic antisense ODN strands
Sense ODN sequence
Rolling circle amplication
Circular DNA
ODN microsponge
Step 2
PLL
Condensation
Step 3
DNA-based LbL nanoparticle
DNA
PEI

Figure 2

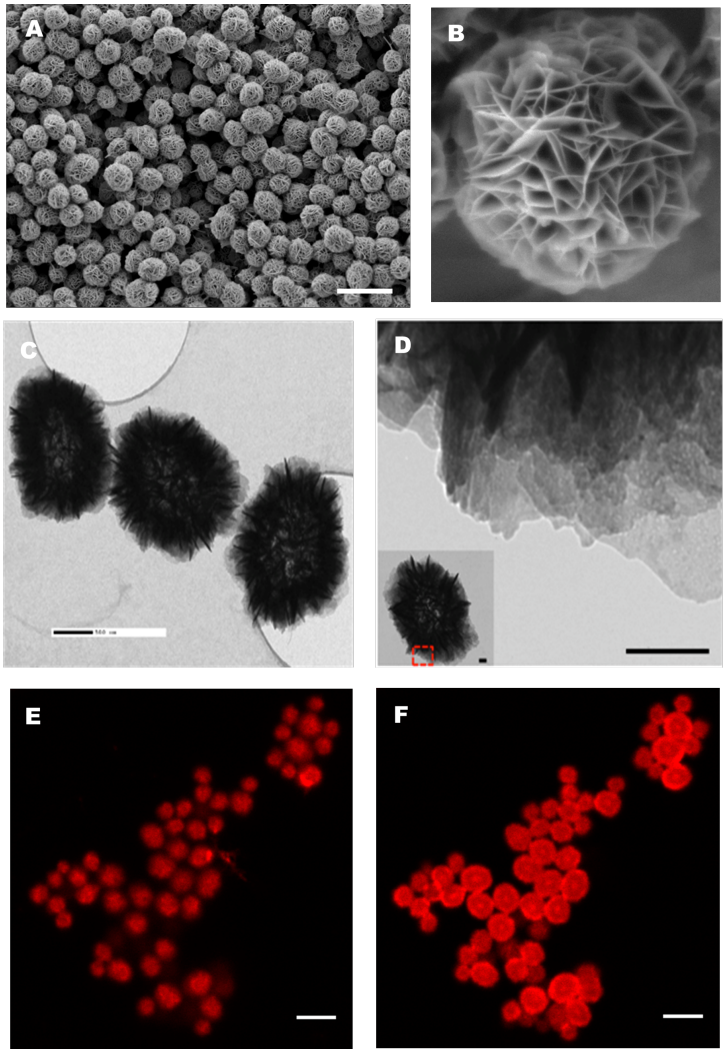

Figure 3

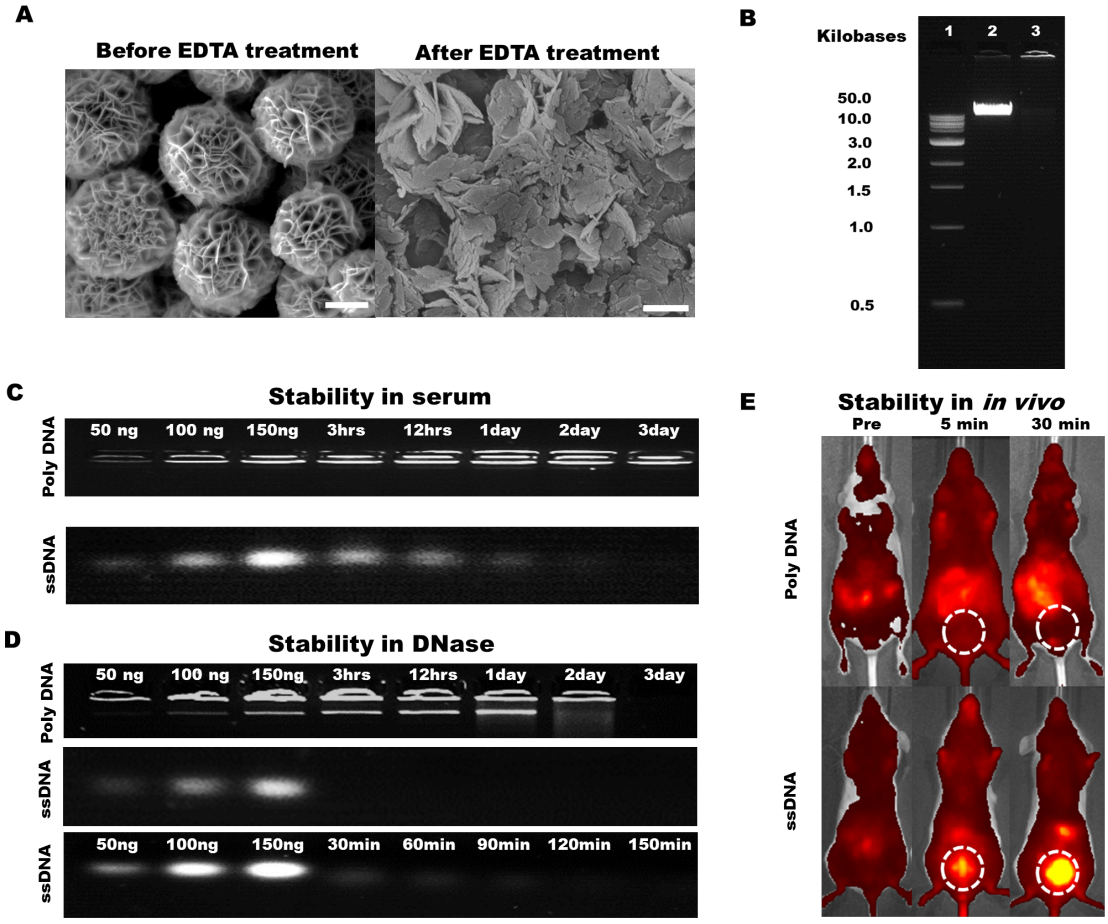
A
Before EDTA treatment
After EDTA treatment
B
Kilobases
1
2
3
50.0
10.0
3.0
2.0
1.5
1.0
0.5
C
Stability in serum
Poly DNA
50 ng
100 ng
150ng
3hrs
12hrs
1day
2day
3day
ssDNA
D
Stability in DNase
Poly DNA
50 ng
100 ng
150ng
3hrs
12hrs
1day
2day
3day
ssDNA
50ng
100ng
150ng
30min
60min
90min
120min
150min
E
Stability in in vivo
Pre
5 min
30 min
Poly DNA
ssDNA

Figure 4

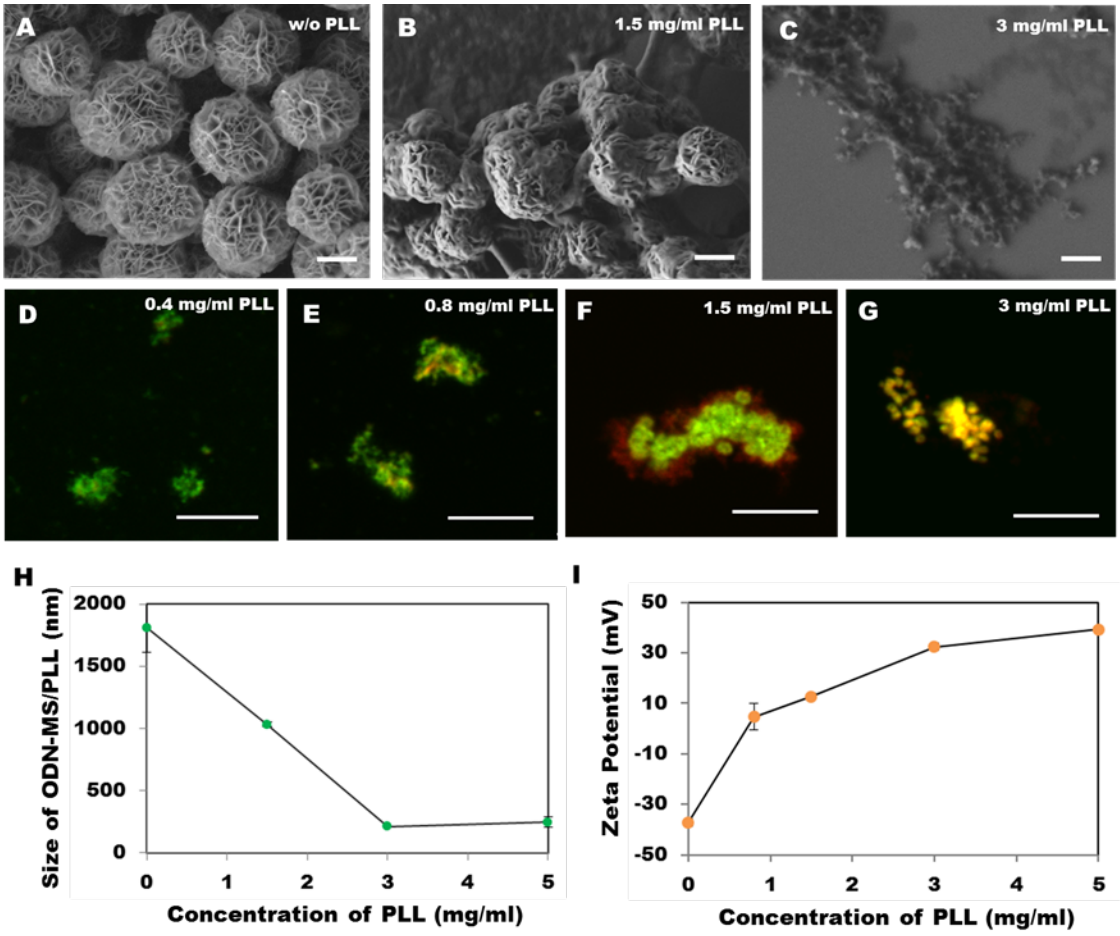
A
w/o PLL
B
1.5 mg/ml PLL
C
3 mg/ml PLL
D
0.4 mg/ml PLL
E
0.8 mg/ml PLL
F
1.5 mg/ml PLL
G
3 mg/ml PLL
H
Size of ODN-MS/PLL (nm)
2000
1500
1000
500
0
0
1
2
3
4
5
Concentration of PLL (mg/ml)
I
Zeta Potential (mV)
50
30
10
-10
-30
-50
0
1
2
3
4
5
Concentration of PLL (mg/ml)

Figure 5

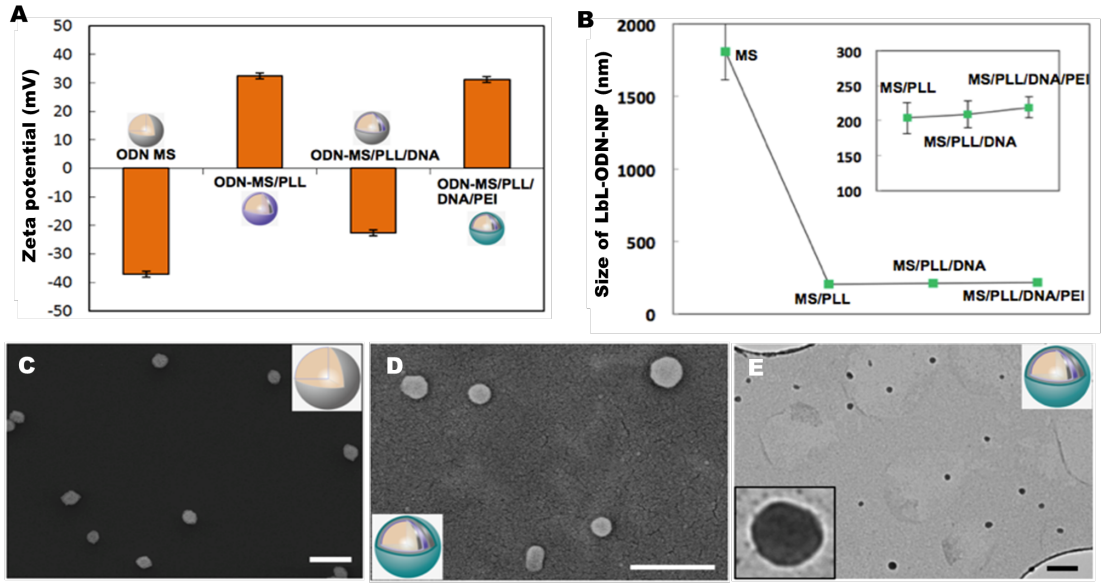
A
Zeta potential (mV)
50
40
30
20
10
0
-10
-20
-30
-40
-50
ODN MS
ODN-MS/PLL
ODN-MS/PLL/DNA
ODN-MS/PLL/ DNA/PEI
B
Size of LbL-ODN-NP (nm)
2000
1500
1000
500
0
MS
MS/PLL
MS/PLL/DNA
MS/PLL/DNA/PEI
300
250
200
150
100
C
D
E

Figure 6

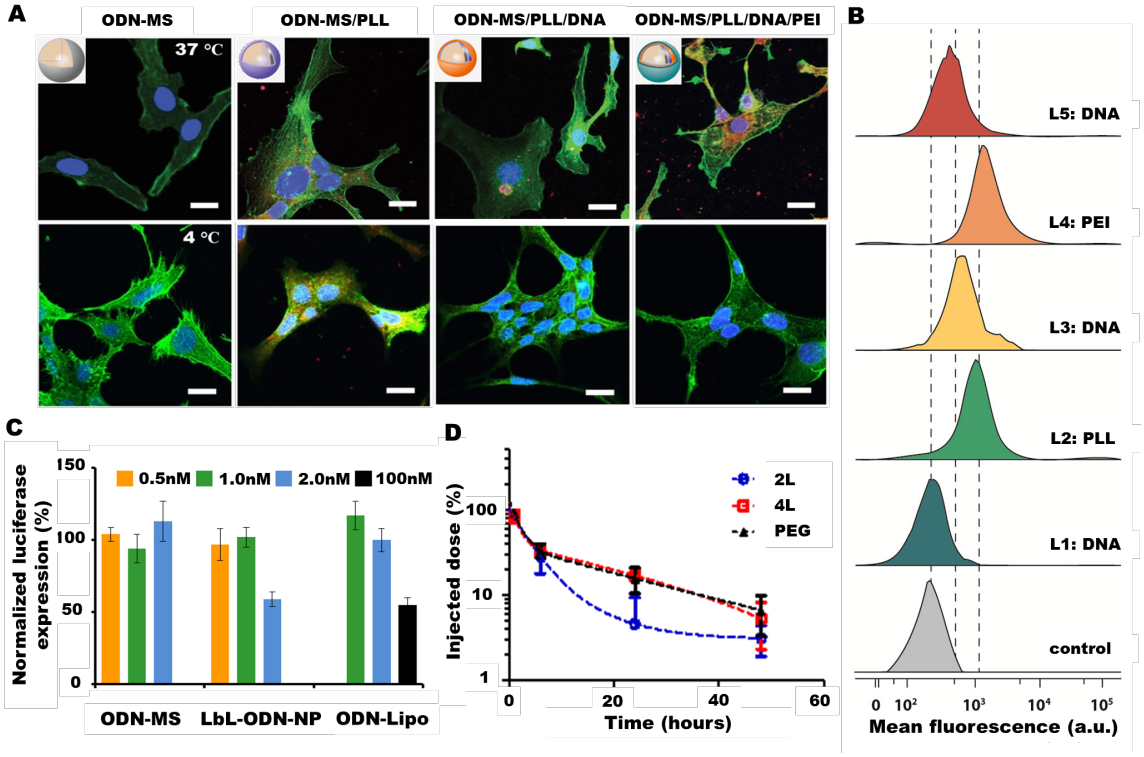
A
ODN-MS
ODN-MS/PLL
ODN-MS/PLL/DNA
ODN-MS/PLL/DNA/PEI
37 °C
4 °C
B
L5: DNA
L4: PEI
L3: DNA
L2: PLL
L1: DNA
control
0 10² 10³ 10⁴ 10⁵
Mean fluorescence (a.u.)
C
Normalized luciferase expression (%)
150
100
50
0
0.5nM 1.0nM 2.0nM 100nM
ODN-MS LbL-ODN-NP ODN-Lipo
D
Injected dose (%)
100
10
1
0 20 40 60
Time (hours)
2L
4L
PEG

TOC

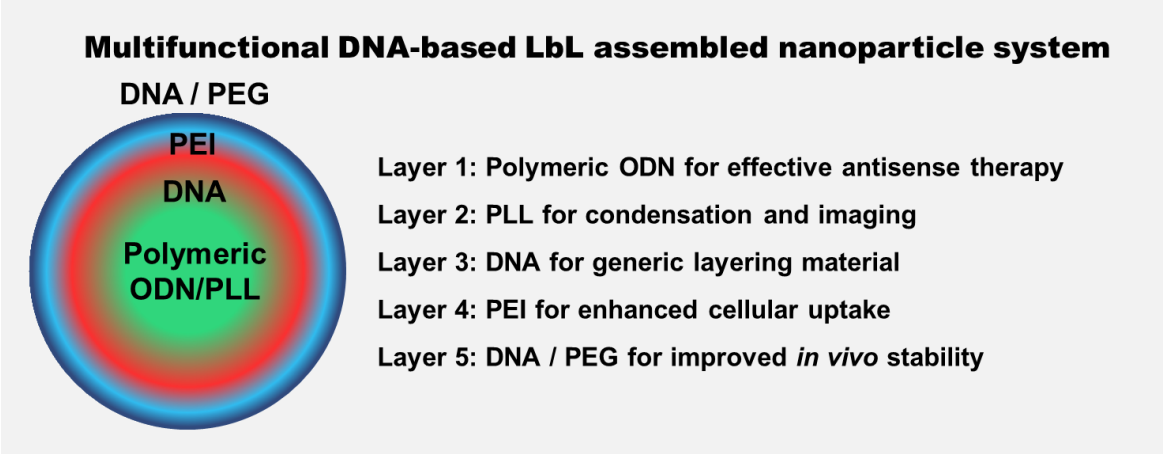
Multifunctional DNA-based LbL assembled nanoparticle system
DNA / PEG
PEI
DNA
Polymeric ODN/PLL
Layer 1: Polymeric ODN for effective antisense therapy
Layer 2: PLL for condensation and imaging
Layer 3: DNA for generic layering material
Layer 4: PEI for enhanced cellular uptake
Layer 5: DNA / PEG for improved *in vivo* stability

Supplementary Information

Layer-by-Layer Assembled Antisense DNA Microsponge Particles for Efficient Delivery of Cancer Therapeutics

Young Hoon Roh, Jong Bum Lee, Kevin E. Shopsowitz, Erik C. Dreaden, Stephen W. Morton, Zhiyong Poon, Jinkee Hong, Inbar Yamin, Daniel K. Bonner, and Paula T. Hammond*

Supplementary Table 1. Oligonucleotide sequences used for antisense DNA microsponge particle synthesis

Strand	Sequence
Linear ssDNA	5'-Phosphate-ATAGTGAGTCGTATTAACGTACCAACCG GCAAGCTGACCCTGAAGTTCACTTGAATCGAAGTAC TCAGCGTAAGTTTAGAGGCATATCCCT-3'
Primer ssDNA	5'-TAATACGACTCACTATAGGGAT-3'

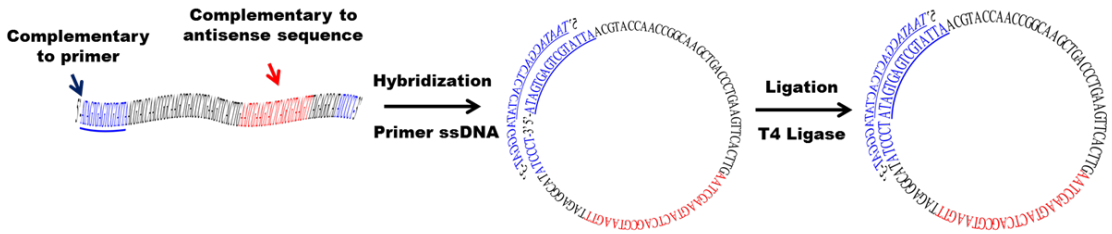

Supplementary Table 2. Reaction parameters for condensation

Parameters	Condensation with salt (0.1 M Na_2HPO_4)	Condensation w/o salt
MW 1000	NO	NO
MW 5000	YES	NO
MW 25000	YES	NO
pH 3.0	NO	NO
pH 7.0	YES	NO
pH 10.0	NO	NO
Temp 24ºC	YES	NO
Temp 37ºC	YES	NO
Temp 50ºC	YES	NO

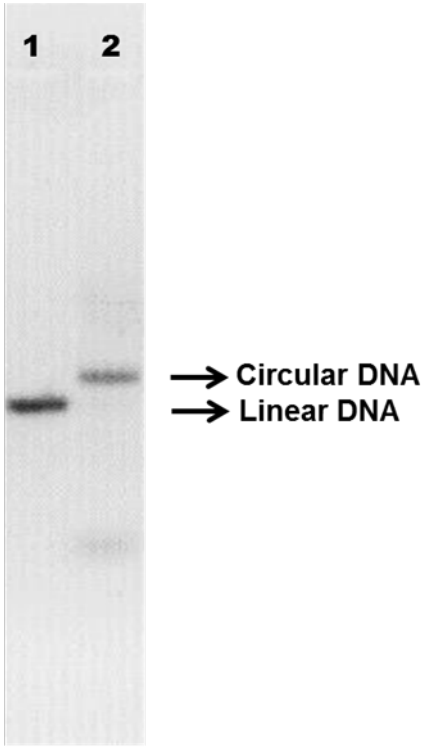

Supplementary Figure 1. Synthesis of circular DNA template. The images of the electrophoretic mobility of linear DNA and circular DNA template used for the synthesis of ODN-MS. A distinct band shift was observed between linear DNA (**Lane 1**) and circular DNA template (**Lane 2**) due to the change in the mobility of the DNA structure.

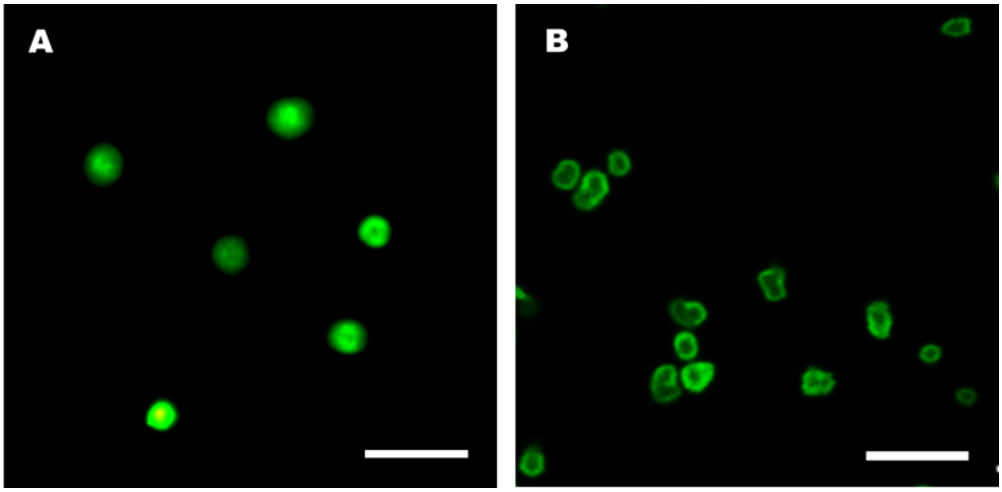

Supplementary Figure 2. Characterization of the morphology of giant antisense microsponge particle. A-B) Fluorescence and confocal microscope images of ODN-MS after staining with SYBR II, an ssDNA specific dye. Scale bars indicate 10 μm.

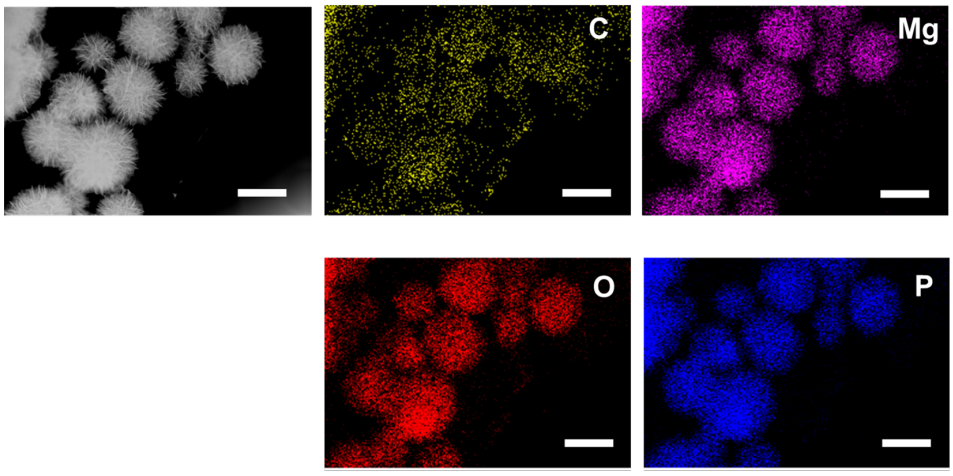

Supplementary Figure 3. Structural characterization of antisense microsponge particle. STEM-based EDX mapping of ODN-MS. Scale bar indicates 500 nm.

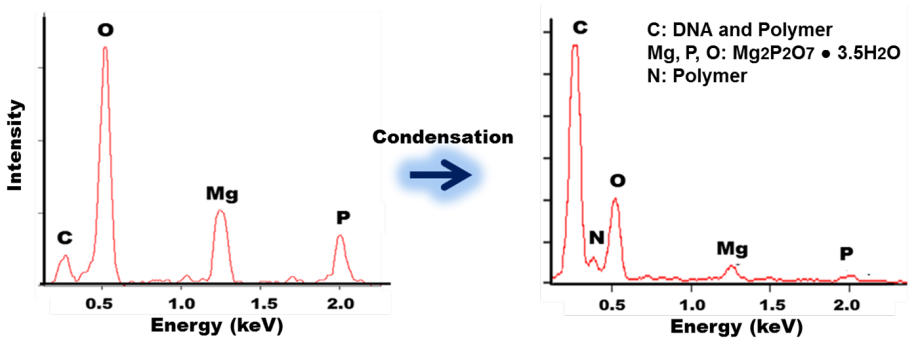

Element	Before Condensing Wt (%)	After Condensing Wt (%)
C	5.5	47.2
O	54.9	33.1
Mg	17.1	2.7
P	22.5	1.1
N	-	15.9

Supplementary Figure 4. Characterization of polymeric ODN packaging during condensing process. EDX spectrum obtained from the point analysis of ODN-MS before and after condensation. Each element weight (%) of ODN-MS is indicated in the Table.

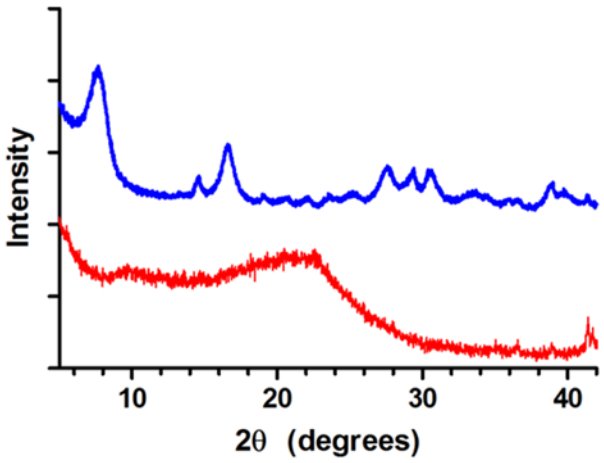

Supplementary Figure 5. Characterization of polymeric ODN packaging during condensing process. PXRD patterns of ODN-MS before condensation and ODN-MS/PLL after condensation.

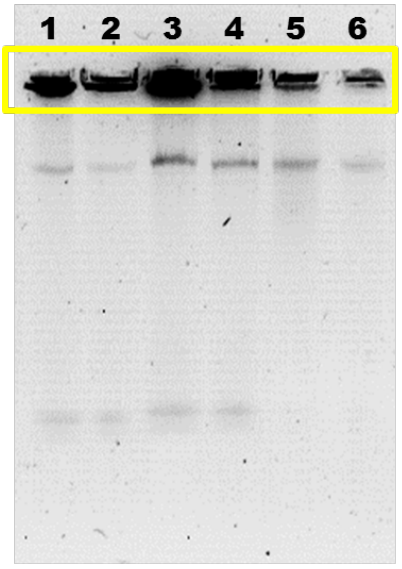

Lane 1 **ODN-MS after 8 hrs RCA reaction**
Lane 2 **Polymeric DNA after EDTA treatment**
Lane 3 **ODN-MS after 12 hrs RCA reaction**
Lane 4 **Polymeric DNA after EDTA treatment**
Lane 5 **ODN-MS after 16 hrs RCA reaction**
Lane 6 **Polymeric DNA after EDTA treatment**

***0.5% Agarose Gel, 70V, 100 min, TB 1X Buffer**

Supplementary Figure 6. Characterization of the sizes of polymeric DNA structures after the generation of microsponges. Gel electrophoresis mobility shift image of ODN-MSs and polymeric DNAs structures disrupted by EDTA at the varied RCA reaction times**.**

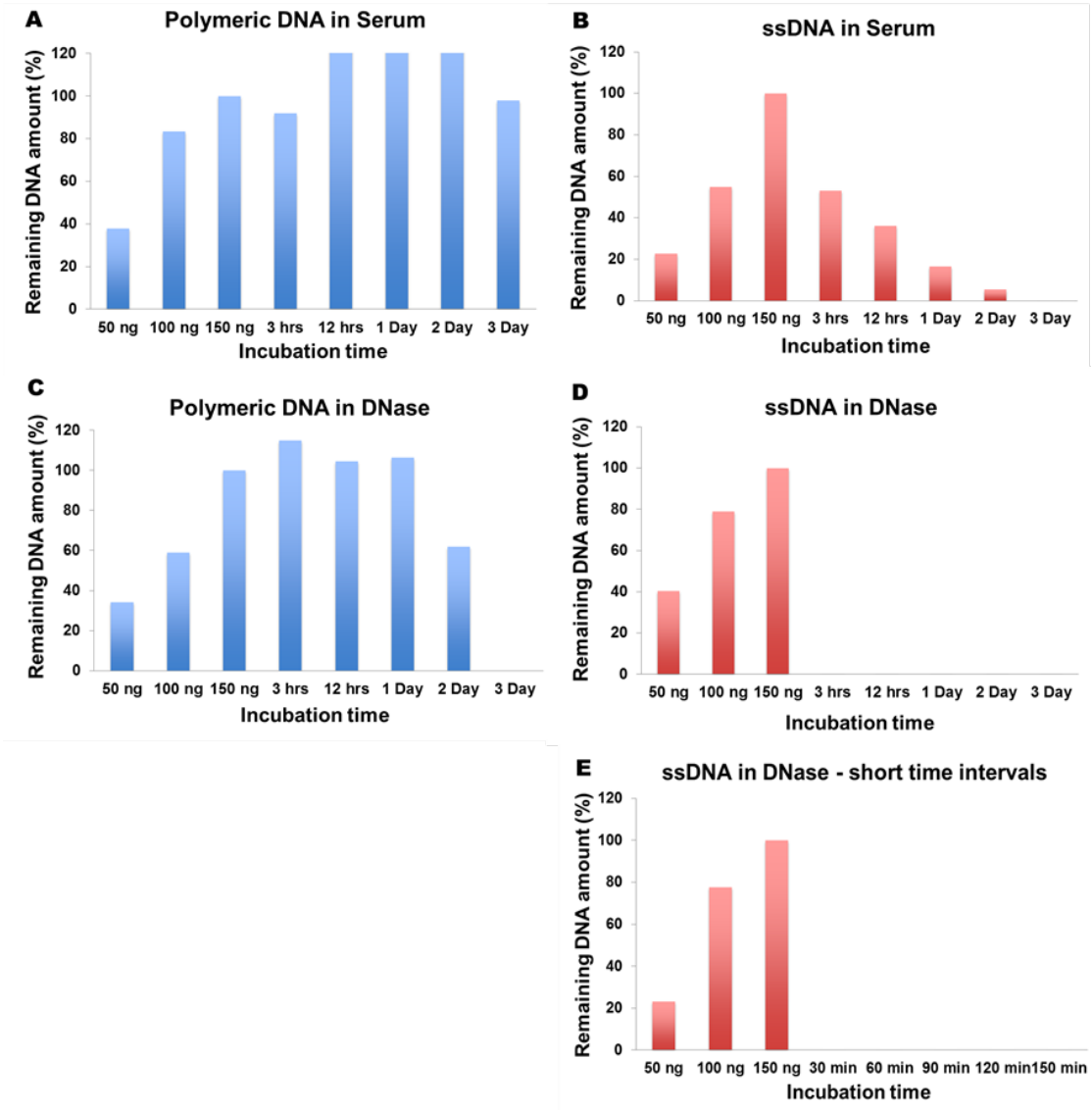

Supplementary Figure 7. Characterization of ssDNA and polymeric DNA structure stability. Stability of short ssDNA and polymeric DNA after a pre-assigned incubation time in serum medium and DNase treatment was further analyzed by Image J analysis after gel electrophoresis (**Ref 1)**.

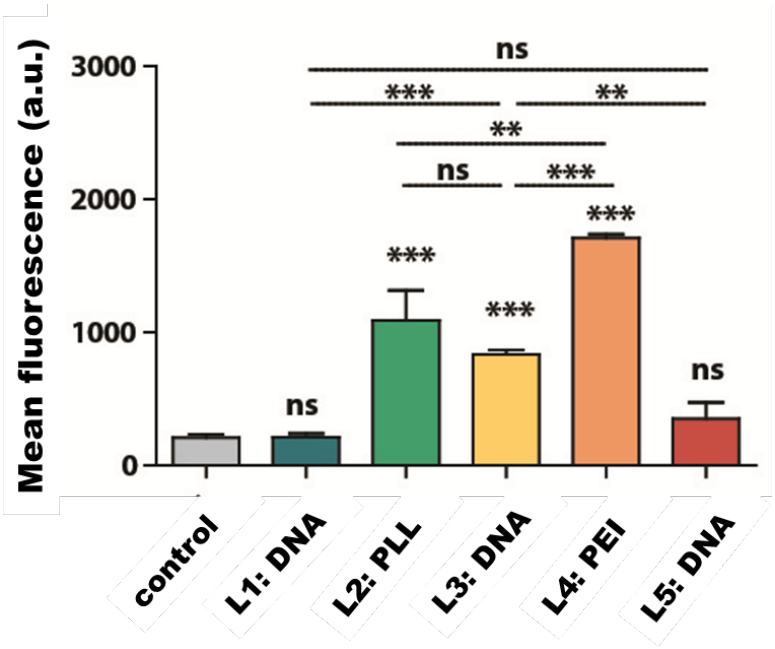

Supplementary Figure 8. Cell uptake of LbL-ODN nanoparticles. Cellular uptake study of LbL-ODN-NPs in cancer cells (e.g. SKOV3) by using flow cytometry analysis.

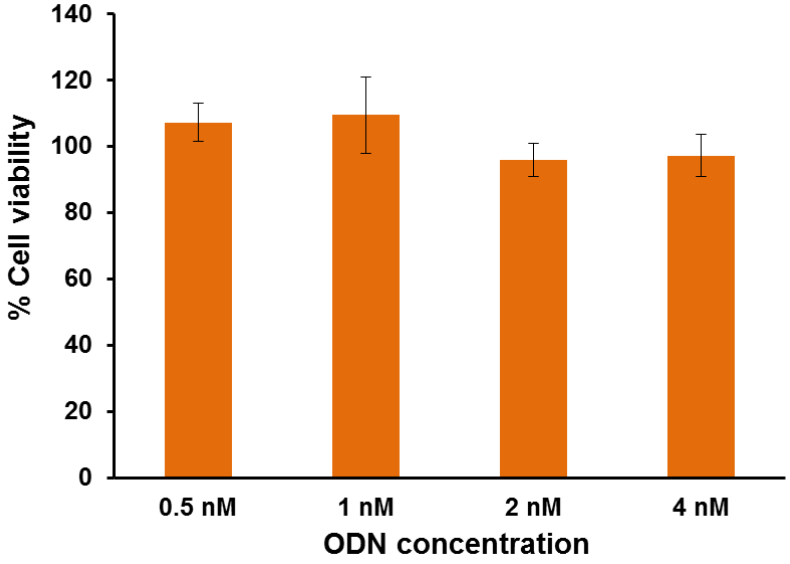

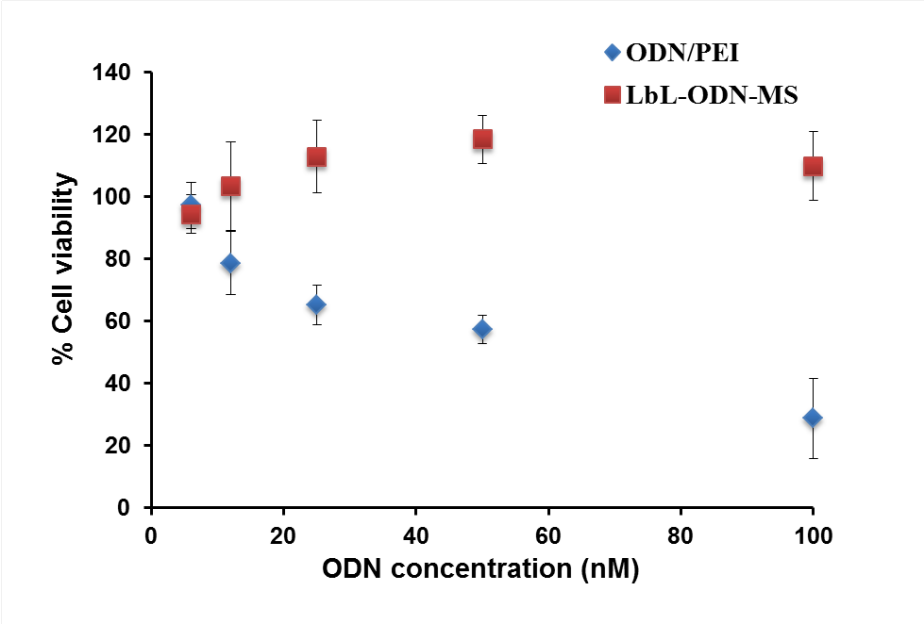

Supplementary Figure 9. Cell viability of LbL-ODN nanoparticles. Viability of SKOV3 cells after 48 h of incubation with varied concentrations of LbL-ODN-NPs as measured by MTT assays. The viability of LbL-ODN-NP system was further compared with the most commonly used polymeric synthetic vectors (*e.g.*, PEI).

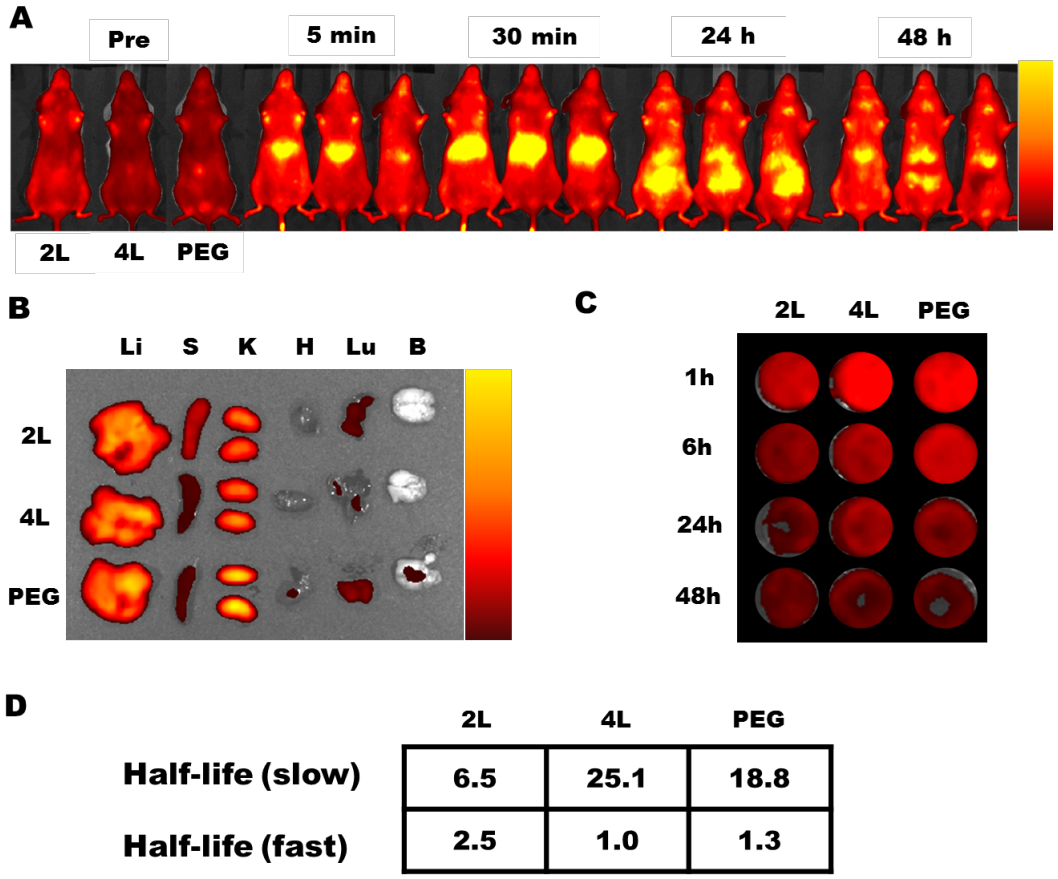

	2L	4L	PEG
Half-life (slow)	6.5	25.1	18.8
Half-life (fast)	2.5	1.0	1.3

Supplementary Figure 10. Systemic delivery of LbL-ODN nanoparticles.

A) Represenative biodistribution data for differentially layered LbL-ODN-NPs (2L, 4L, and PEG) formulations following IV-administration in BALB/c mice after 5 min, 30 min, 24 h, and 48 h. Data presented with mice imaged ventrally at λex = 640 nm, λem = 700 nm. **B)** Necropsy was performed at the terminal 48 h time point and presented in order. (Li = liver, S = spleen, K = kidneys, H = heart, Lu = lungs, B = brain). **C)** Isolated blood samples imaged at λex = 640 nm, λem = 700 nm investigating nanoparticle pharmacokinetics by percent fluorescence recovery following IV administration. Quantification and fit to data shown in Figure 6F in main text. **D)** Half-lives extracted from 2-phase decay shown in tabular format.

General reagents and DNA sequences

The certified DNase free water was used for all experiments. Oligonucleotides were commercially synthesized with PAGE purification and purchased from Integrated DNA Technologies (Coralville, IA). The DNA sequences for the oligonucleotides are listed in Supplementary Table 1. The fluorescein and cyanine labeled analog of deoxyuridine triphosphates (dUTPs) were purchased from PerkinElmer (Waltham, MA). SYBR® Green II Nucleic Acid Gel Stain was obtained from Lonza (Walkersville, MD). T4 DNA ligase, Luciferase assay kits, and the corresponding buffers were purchased from Promega (Madison, WI). DNA polymerase (Phi29) and reagent sets (dNTPs solution mix and reaction buffer) were purchased from Epicentre (Madison, WI). DNA ladders, loading dyes, DNases and the corresponding reaction buffers were purchased from New England Biolabs (Ipswich, MA). Quant-iT™ OliGreen® ssDNA Assay Kit was obtained from life Technologies (Carlsbad, CA). Linear polyethyleneimine (PEI, Mw = 25,000 g/mol) was obtained from Polysciences (Warrington, PA). Poly(ethylene glycol)-b-poly-L-glutamic acid (PEG-PGA, Mw = 13,000 g/mol) was purchased from Alamanda Polymers (Huntsville, AL). All other chemical reagents were purchased from Sigma-Aldrich (St. Louis, MO). SKOV3 human ovarian carcinoma cells were purchased from ATCC (Manassas, VA). Cell culture reagents were purchased from Invitrogen (Carlsbad, CA). Lipofectamine was obtained from Invitrogen (Carlsbad, CA). Cell Counting Kit - 8 (CCK-8) was obtained from Dojindo Molecular Technologies (Rockville, MD).

Calculation of amount of ODN from the generated polymeric DNA

Experimentally, the molecular weight of the generated polymeric DNA from ODN-MS was determined by gel electrophoresis results (See Supplementary Figure 3). The number of repeated active ODN strands in the generated polymeric DNA was calculated as follows:

- RCA product generally produces very long DNA strands = approximately 47 milliion Da
- Molecular weight of ssDNA = (the number of nucleotides x 303.7) + 79

- Total molecular weight of the generated polymeric ssDNA strands = 4.7 x 10^7 Da (g/mol) = 151,465 bases
- Molecular weight of the 91 bases linear ssDNA strands = 27716 Da (g/mole)
- One unit of active ODN strand (21 bases) can be generated from one unit of the linear ssDNA (91 bases)
- Minimum number of repeated active ODN strands from the generated polymeric ODN structure = 151,465 bases / 91 bases = 1665

According to gel electrophoresis results and following the calculations, several thousands (~1665) of the repeated ODN therapeutics can be produced from the generated polymeric DNA.

Evaluation of DNA weight fraction in the microsponge particle

As a method for quantifying the weight fraction (wt %) of DNA in the microsponge particle, we used a fluorescence-based measurement. From thermal gravimetric analysis (Discovery TGA, TA Instruments, New Castle, DE), we first obtained the total mass/volume microsponge particle concentration gravimetrically by drying a provided volume of suspension at 90°C until the weight of ODN-MS became thermally stable. Then this value was compared with the DNA concentration for the same ODN-MS sample using a fluorescence-based ssDNA quantification assay (Quant-iT™ OliGreen® ssDNA Assay Kit, Life Technologies, Carlsbad, CA) following company's protocol. Fluorescence intensity (λex = 480 nm, λem = 520 nm) from DNA was determined using a fluorescence microplate reader (Tecan Infinite® 200 PRO) after EDTA treatment to release the polymeric DNA from ODN-MS. The concentration of polymeric DNAs was determined based on the DNA standard curve of fluorescence intensity versus concentration. DNA weight fraction (%) was calculated by dividing the fluorescence-based DNA concentration by the gravimetric ODN-MS concentration. The DNA quantification measurements were performed on three independent samples. From these measurements, we obtained the DNA loading of 12.5 + 1.8 wt.%.

References

(1). C. D. Georgiou, I. Papapostolou, K. Grintzalis, *Nat. Protoc.* **2009**, 4, 125-131.

Bimodal Tumor-Targeting From Microenvironment Responsive Hyaluronan Layer-by-Layer (LbL) Nanoparticles

Erik C. Dreaden,[†,‡] Stephen W. Morton,[†,‡] Kevin E. Shopsowitz,[†,‡] Jae Hyeok Choi,[§,¶] Zhou J. Deng,[†,‡] Nam-Joon Cho,[§,¶,∥] and Paula T. Hammond[†,‡,††,]*

[†]Koch Institute for Integrative Cancer Research, [‡]Department of Chemical Engineering, [††]Institute for Soldier Nanotechnologies, Massachusetts Institute of Technology, 500 Main Street, Cambridge, MA 02142, United States

[§]School of Materials Science and Engineering, [¶]Centre for Biomimetic Sensor Science, [∥]School of Chemical and Biomedical Engineering, Nanyang Technological University, 639798, Singapore

KEYWORDS self-assembly, nanomaterials, nanomedicine, polymer engineering, controlled delivery

ABSTRACT

Active targeting of nanoscale drug carriers can improve tumor-specific delivery; however, cellular heterogeneity both within and among tumor sites is a fundamental barrier to their

success. Here, we describe a tumor microenvironment-responsive layer-by-layer (LbL) polymer drug carrier that actively targets tumors based on two independent mechanisms: pH-dependent cellular uptake at hypoxic tumor pH and hyaluronan-directed targeting of cell-surface CD44 receptor, a well-characterized biomarker for breast and ovarian cancer stem cells. Hypoxic pH-induced structural reorganization of hyaluronan-LbL nanoparticles was a direct result of the nature of the LbL electrostatic complex, and led to targeted cellular delivery *in vitro* and *in vivo*, with effective tumor penetration and uptake. The nanoscale drug carriers selectively bound CD44 and diminished cancer cell migration *in vitro*, while co-localizing with the CD44 receptor *in vivo*. Multimodal targeting of LbL nanoparticles is a powerful strategy for tumor-specific cancer diagnostics and therapy that can be accomplished using a single bilayer of polyamine and hyaluronan that, when assembled, produce a dynamic and responsive cell-particle interface.

Introduction:

Nanoscale drug delivery is an attractive option for cancer therapeutics that exhibit poor pharmacokinetics,[1] dose-limiting toxicities, or chemical instability.[2] This strategy typically improves tumor-specific delivery through either size-dependent 'passive' targeting[3, 4] and/or 'active' targeting that can be ligand-directed [5] or stimuli-responsive.[6] While active targeting often augments tumor cell killing, its efficacy is intrinsically limited by cellular heterogeneity that exists both within and among tumors.[7-9] Genetic diversity within breast tumors, for example, is known to be associated with both tumor stage and subtype in breast carcinoma.[10] Similarly, diversity within the subclonal structure of esophageal lesions is known to predict progression to malignancy.[11] Following metastasis, as many as 24-38% of breast, lung, and melanoma cancer

patients exhibit differential expression of biomarkers that predicate treatment response (e.g. amplified *HER2*, mutant *EGFR*, and mutant *BRAF*, respectively).[12] Tumor heterogeneity is a fundamental challenge to the success of actively-targeted nanoscale drug delivery and vehicles capable of multimodal active targeting are urgently needed.

Layer-by-Layer (LbL) nanoparticles are an emerging class of self-assembled polymer drug carrier that addresses several challenges in the delivery of small molecule therapeutics and imaging agents.[13-21] These modular structures consist of (i) a functional nanoparticle core, (ii) a multilayered polyelectrolyte shell, and (iii) an exterior tumor-targeting stealth layer. The core consists of drug-loaded polymer nanoparticles,[22-25] liposomes,[26, 27] multimeric RNA,[28] or a range of organic/inorganic nanoscale materials and imaging agents (e.g. quantum dots,[20] silica,[29] gold,[20] hydroxyapatite,[30] or iron oxide[31]). The multilayered shell can include hierarchically-assembled polymers, proteins, small molecules, or nucleic acids that exhibit complementary charge/bonding interactions. In prior work, we demonstrated that LbL nanoparticle architectures can achieve long systemic circulation (elimination $t_{1/2} \sim 28$ h),[26] low off-target delivery (10-15 %ID/g liver),[20] active tumor targeting,[19] and can enhance the *in vivo* stability of therapeutic RNA for efficacious synergistic siRNA/drug combination therapy,[26, 28] or incorporate nanoparticle cores containing diagnostic imaging agents[23] and cytotoxic chemotherapeutics.[26, 27] Here, we engineer a novel LbL nanoparticle architecture that actively targets solid tumors through two independent mechanisms: selective binding to cell-surface CD44 receptor and acid-induced cellular delivery at hypoxic tumor pH. This approach allows for the creation of nanoparticles that respond to the tumor micro-environment in two unique ways, thus greatly enhancing targeting and uptake. Rather than employing nondegradable neutral polymers such as poly(ethylene glycol), synthetic ligand attachment, or complex linker chemistry, we accomplish an intrinsic responsive behavior

through the simple use of biologically-derived weak polyelectrolytes in a self-assembled thin film.

2D LbL films assembled from partially-ionized or 'weak' polyelectrolytes are well-known to exhibit dynamic structure and stability with respect to pH compared with their strong polyelectrolyte counterparts.[32-34] For example, dramatic shifts in adsorbed layer thickness, surface morphology, and effective ionic crosslink density have been observed due to thermodynamic trade-offs and weak Coulombic interactions between nearest-neighbor proton binding sites.[34] The hypoxic microenvironment of solid tumors also exhibit a narrow gradient in pH; poor blood perfusion and rapid metabolic consumption of oxygen results in a drop in pH from 7.4 (normoxic) to <6.6 in distances as short as 150 μm from the vessel wall,[35] providing an environment that can select for and host aggressive and metastatic cell phenotypes.[36] One of the challenges in nanoparticle design for cancer treatment is their infiltration and penetration through the stroma and into tumor tissues, and selective uptake of nanoparticles within the tumor tissue.

We hypothesized that LbL nanoparticle architectures incorporating functional biopolymers that, themselves, are weak polyelectrolytes, may achieve both receptor-targeting *and* pH-triggered engagement of and delivery to solid tumors without the need for ligand coupling chemistries, active proteins, or stealth layers that can introduce potential issues with compatibility, immune response, or blood half-life. To this end, we selected a weak polyamine, poly(L-lysine), which is a synthetic polypeptide from a natural amino acid, and a complementary weak polyacid, hyaluronan (HA), which is a native extracellular matrix polysaccharide, to serve as functional components of this dual-targeting LbL drug carrier. While both polyelectrolytes are biocompatible pharmaceutical excipients (e.g. benzylpenicilloyl polylysine), hyaluronan, also

known as hyaluronic acid or HA, is unique in that it also exhibits protein-repellent behavior and is an active component in many post-surgical adhesion barriers.[37] Importantly, hyaluronan is the endogenous ligand for cell-surface receptor CD44, a well-characterized biomarker for breast and ovarian carcinoma cells with tumor-initiating[38], drug-resistant,[39] and stem-like phenotype[40, 41] that can be used to target these tumors.[42-44] A unique capability introduced with LbL nanofilms containing hyaluronan is the potential to tune its charge interactions with an underlying polyamine to produce a dense and compact charged repulsive brush layer at blood pH that can convert to a swollen neutral layer that readily engages cells at hypoxic tissue pH.

RESULTS AND DISCUSSION

Dual-targeting hyaluronan-LbL architectures (**Figure 1**) consisting of only 2 layers, or 1 bilayer repeat, were assembled onto model drug carriers (fluorescent polystyrene nanoparticles) via sequential adsorption and centrifugation from solutions of aqueous hyaluronan and poly(L-lysine), as described previously.[20] **Figures 2a,b** illustrate the gradual increase in hydrodynamic size and corresponding shift in surface charge of the nanoparticles during the LbL assembly process, yielding particles 135±4 nm in hydrodynamic diameter and -33±1 mV in zeta potential (PDI 0.11±0.01). Transmission electron micrographs (**Figure 2c**) and cross-sectional 3D renderings of energy-filtered TEM images (EFTEM, **Figure 2d**) confirmed structural partitioning between the carbon-rich polystyrene nanoparticle core and the oxygen-rich LbL multilayered shell.

Hypoxia-mediated uptake:

We assessed pH-dependent cell binding/uptake of the hyaluronan-LbL nanoparticles by flow cytometry of Hep G2 human hepatocyte cells. **Figure 2e** illustrates a 2.4-fold increase in

nanoparticle-associated cellular fluorescence as extracellular pH is reduced from normoxic (7.4) to hypoxic pH (6.0). Interestingly, non-specific targeting of the hyaluronan-nanoparticles at pH 7.4 was 15-fold lower than that from a related acid-labile PEG-LbL architecture with a pH-sensitive iminobiotin linker previously designed in our group to release a PEG shielding layer and "unveil" positively charged surfaces (**Figure S1a**).[19] These findings are consistent with the notion that mucopolysaccharide-coated surfaces can exhibit antifouling behavior to prevent protein opsonization.[45] Hypoxia-specific delivery of the hyaluronan-LbL architecture (pH 6.0 v 7.4) was likewise improved 2.5-fold relative to the previous iminobiotin architecture (**Figure S1b**), indicating enhanced cellular delivery at pH values reflective of the hypoxic tumor microenvironment. Delivery of the hyaluronan-LbL nanoparticles into 3D tumor spheroids was also investigated by confocal fluorescence microscopy of Hep G2 hepatocyte and breast adenocarcinoma cell nodules. We observed both high tumor penetration (**Figure S2**) and hypoxic pH-responsive delivery (**Figure 2f**) of hyaluronan-LbL nanoparticles into 3D tumor spheroids, important properties necessary for efficient penetration throughout the often compacted tumor stroma.[46]

We next investigated pH-dependent structural changes in the hyaluronan-LbL architecture by transmission electron microscopy (TEM), photon correlation spectroscopy, laser Doppler electrophoresis, quartz crystal microbalance-dissipation (QCM-D), and contact angle measurements. Low electron dose TEM images of particles incubated in pH 7.4 and 6.0 buffer indicate significant (ca. 3.1-fold) swelling of the LbL polymer shell at hypoxic pH (**Figure 3a**), findings corroborated by DLS measurements that indicate a half maximal increase in hydrodynamic size at ca. pH 6.8 (**Figure 3b**). The hydrodynamic shell thickness increase agreed well with that observed by TEM, also swelling 3.1-fold from 24±8 nm at pH 7.4 to 74±15 nm at

pH 6.0. Zeta potential measurements (**Figure 3c**) show that pH-dependent swelling is also accompanied by a neutralization of stabilizing surface charge, which drops to an equilibrium value of approximately -3 mV at below ca. pH 7.06. QCM-D measurements of hyaluronan adsorption onto amine-modified Au (**Figure 3d**) likewise suggest a highly pH-dependent assembly process with half maximal frequency shift observed at ca. pH 6.91. Contact angle measurements from nanoparticles immobilized on silicon substrates (**Figure 3e**) similarly support hypoxic pH-induced rearrangements at the surface, as indicated by a statistically significant increase in contact angle, which corresponds to decreased apparent surface energy with decreasing pH. These pH-dependent changes in layer thickness, as well as QCM-D and contact angle measurements are consistent with prior reports of planar LbL film assemblies of weak polyacids and polyamines.[34, 47, 48]

Notably, the pKa of hyaluronic acid in solution is reported to be approximately 3.0 and that of poly(L-lysine) is about 10. A brush monolayer of HA alone, thus, would not be anticipated to undergo significant changes in charge at hypoxic pH. In contrast, polyelectrolyte multilayers create controlled complexes that can exhibit acid-base equilibria that are tuned by assembly pH and ionic strength.[32, 47] Multilayers of poly(allyl amine) hydrochloride and hyaluronic acid for example,[49] exhibit dynamic shifts in HA acid dissociation equilibrium, surface roughness, and multilayer swelling as a function of assembly pH. These changes are attributed to a reduction in the apparent acid and base character of the HA and PLL, respectively, due to charge compensation between partially ionized side chains of these 'weak' polyelectrolytes following pH-dependent adsorption, as well as assembly-induced secondary structure formation that disfavors proton exchange. Such polyelectrolyte assemblies exhibit a unique pKa that is characteristic of the resulting polyion blend and its assembly conditions. We hypothesize that

augmented cellular delivery of the nanoparticles, which is known to increase with increasing surface roughness and/or loss of anionic surface charge,[50] occurs as a result of the previously described pH-dependent structural changes. The swelling of the bilayer may further enhance cell uptake by modulating the effective modulus of the nanoparticle and enabling more significant engagement of the hyaluronic acid groups on the surface of the hydrated outer layer.

Having established hypoxic pH-responsive behavior *in vitro*, we also asked whether hyaluronan-LbL nanoparticles preferentially target tumor hypoxia *in vivo*. Indeed, immunofluorescence microscopy of excised tumor sections indicated a high degree of particle colocalization with hypoxia-inducible factor 1 α (HIF1α)[51] in MDA-MB-468 subcutaneous xenografts following i.v. tail vein injection in mice (72 h, **Figure 3f**). Together with the previous results, these data support that hyaluronan-LbL nanoparticles undergo significant structural changes over a narrow range in pH that is well-suited for hypoxic tumor targeting. This hypoxic pH-responsive behavior is accompanied by hydrodynamic swelling, a loss in stabilizing surface charge, and a decrease in apparent surface energy that correlates with augmented cellular delivery to both 2D and 3D cell cultures, as well as *in vivo* co- localization with hypoxia-inducible factor 1 α in murine tumor models of triple-negative breast carcinoma. The loss of negative charge and slight increase in hydrophobicity of these nanoparticles lead to a significantly increased non-specific uptake by tumor cells within the tumor microenvironment.

Role of CD44 Targeting:

Given that these LbL nanoparticles are surface-functionalized with hyaluronan, the endogenous ligand for cell-surface receptor CD44, we investigated receptor-specific interactions mediated by these particles in a panel of breast carcinoma cells reflecting the luminal, $HER2^+$,

and triple-negative (basal) molecular subtypes of the disease (**Figure 4a**). Note that the previous pH-dependent targeting experiments (above) were performed using a hepatocyte cell line that does not express the CD44 receptor.[52] Consistent with known expression profiles of basal-like breast carcinomas,[41] MDA-MB-231 and MDA-MB-468 cells express high levels of CD44 *in vitro*. Flow cytometry measurements of particle binding/uptake in these cells (pH 7.4) exhibited a fractional but significant contribution from CD44; this enhanced delivery was abrogated following siRNA-mediated silencing of the receptor (**Figure 4b*),*** demonstrating the dependence of this behavior on CD44 binding and subsequent uptake. Cell-surface labeling by CD44 antibodies was likewise significantly diminished following receptor blocking by hyaluronan-LbL nanoparticles (**Figure 4c*)***.

In view of the CD44 receptors' role in mediating cell adhesion interactions,[53] we further investigated the effects of hyaluronan-terminal nanoparticles on both 2D and 3D cell migration in a panel of breast carcinoma cells. Sublethal concentrations of hyaluronan-LbL nanoparticles significantly diminished cell migration in a 2D gap closure assay in a CD44 receptor-selective manner (**Figure 4d; Figure S3,4**). The particles similarly diminished 3D collagen gel transwell invasion – again in a receptor-selective manner – effects which could be recapitulated in part by increasing concentrations of free hyaluronan (**Figure 4e**).

We further investigated the role of CD44 *in vivo* using a mouse model; i.v.-administered hyaluronan-LbL nanoparticles accumulated in MDA-MB-468 breast carcinoma tumor xenografts ca. 4.0-fold greater than control nanoparticles of comparable size and charge that were conjugated with dextran sulfate in place of hyaluronan (**Figure 5a**). Approximately 6% of the initial dose (recovered fluorescence) co-localized with the tumors ex vivo, compared with ca.1.5% for the dextran sulfate LbL-coated control. Further, these nanoparticles colocalized with

the CD44 receptor in subcutaneous xenograft models of a Ras mutant non-small cell lung carcinoma (A549) following systemic i.v. administration, as observed in histology from tumor tissue 48 hours following nanoparticle administration (**Figure 5b***)*, consistent with the notion that hyaluronan-terminal LbL nanoparticles actively target CD44 receptor *in vitro* and *in vivo*. Of note is the significant penetration of nanoparticles through the surrounding stroma into the tumor tissue.

This improved tumor-targeting was accompanied by a 2-fold decrease in liver-specific accumulation, also a key issue for nanoparticle design (**Figure 5c,d**), again in support of the long blood-stream half-life and stability of the hyaluronan nanoparticles, and the effective steric and charge repulsion presented by the LbL bilayer at pH 7.4.

CONCLUSIONS

In summary, we describe a layer-by-layer (LbL) nanoparticle architecture capable of active tumor targeting through two unique mechanisms: hypoxic pH-responsive delivery and ligand-directed targeting of the cell-surface receptor CD44 that is overexpressed in many key forms of cancer. The former strategy exploits the dynamic structural stability of multilayered films of weak polyelectrolytes while the latter utilizes an endogenous polysaccharide, hyaluronan, to direct tissue-specific delivery to cells expressing CD44 receptor, a biomarker for breast and ovarian cancer stem-cells. We show that a singular hyaluronan/poly(L-lysine) bilayer adsorbed on a nanoparticle results in hypoxia-targeted cellular delivery *in vitro* and co-localization with hypoxia-inducible factor 1 α *in vivo*. Hyaluronan-LbL nanoparticles selectively bound CD44 *in vitro*, diminished cancer cell migration in a receptor-selective manner, and colocalized with CD44 receptor *in vivo*. Because these LbL nanoparticle systems are simple, provide a means of

modular design, and can provide enhanced blood half-life[20, 26] and enhanced tumor targeting, hyaluronan-LbL nanoparticles are promising candidates for targeted drug delivery to solid tumors for a number of significant cancer types. The ability to target multiple tumor cell populations without the use of additional drug carrier may circumvent resistance from selective pressure while improving safety and treatment outcomes from actively targeted nanomedicines.

MATERIALS AND METHODS

Layer-by-Layer (LbL) Assembly

Nanoparticle LbL assembly was performed as described previously [20] with minor modifications. Briefly, poly(L-lysine) HBr (PLL, 15-30 kDa; Sigma-Aldrich), hyaluronan (HA, 200 kDa; Lifecore), and dextran sulfate sodium salt (20 kDa; Sigma-Aldrich) were used as-received without further modification. All solutions were prepared in PBS (-Ca^{2+}/-Mg^{2+}) diluted 100-fold in ultrapure water, adjusted to pH 7.40, and sterile filtered (0.2 μm) immediately prior to use. 100 nm diameter carboxy-modified polystyrene latex nanospheres were diluted to 0.2 wt%. Nanospheres (2 mg) were added dropwise to a rapidly stirring 45 mL solution of PLL (500 μM) at RT and allowed to stir in dark for 1-2 h. The nanoparticles were recovered by centrifugation (1 h, 15000 rcf, RT) and diluted to 1 mL. 500 μL of the PLL-conjugated nanoparticles were added dropwise to a rapidly stirring 45 mL solution of HA (10 μM) previously chilled to 4 °C and allowed to stir in dark for 30 min at 4 °C. HA-conjugated nanoparticles were recovered by centrifugation (1 h, 15000 rcf, 4 °C) and stored in dark, as concentrates, at 4 °C within 1 week of use. 100 nm fluorescent carboxylate-modified polystyrene

nanospheres (Life Technologies; Blue 350/440, Red 580/605, Infrared 715/755; Sigma-Aldrich; Orange 481/644) were used as appropriate. Nanoparticle concentration was estimated based on fluorophore absorption λ_{max} and the stock nanoparticle molar concentration as:

$$[mol/L] = \frac{6C \times 10^{15}}{N_A \times \rho \times \pi \times \phi^3} \quad (1)$$

where C is concentration in $g \cdot mL^{-1}$, N_A is Avagadro's number 6.022×10^{23} mol^{-1}, ρ is density in $g \cdot mL^{-1}$ (1.05 for polystyrene), and ϕ is diameter in μm.

Structural Characterization

Photon correlation spectroscopy and laser Doppler electrophoresis measurements were performed using a Malvern Zetasizer Nano ZS90 particle analyser (λ=633 nm, material/dispersant RI 1.590/1.330). Transmission electron microscopy (TEM) was carried out using a JEOL 2100 FEG instrument. Energy-filtered TEM (EFTEM) was performed using a JEOL 2010F TEM equipped with a Gatan imaging filter operating at an accelerating voltage of 200 kV. Samples were prepared by dropcasting particle suspensions onto a TEM grid with a Quantifoil holey carbon support film. Elemental maps were generated at the K edges of carbon (284 eV) and oxygen (532 eV) by using the three window technique and applying the default parameters provided by the Gatan Digital Micrograph software for these elements. EFTEM images were rendered using the Interactive 3D Surface Plot plugin for ImageJ. Measurements were obtained from ultrapure water or following overnight incubation in phosphate buffered saline (PBS) solutions adjusted using HCl or NaOH. Contact angle measurements were conducted by the Sessile droplet method using a Rame-Hart Contact Angle Goniometer, pH-adjusted PBS buffer, and APTES-modified Si wafers. Quartz crystal microbalance-dissipation

(QCM-D) measurements were performed using a Q-Sense E4 instrument (Q-Sense AB, Göthenburg, Sweden), as described previously.[54] The measurement substrate was an amine-modified gold surface, which was prepared by incubating gold-coated sensor crystals (QSX301, Q-Sense AB) in 1 mM 11-amino-1-undecanethiol hydrochloride (Sigma-Aldrich). For QCM-D experiments, 10 mM Tris buffer with 150 mM NaCl (pH 7.5) was first injected in order to obtain a stable baseline, followed by addition of polyelectrolyte solutions (100 μl·min^{-1}) for 70 min and then static incubation for 20 min. Finally, a buffer wash was performed in the same pH condition and the final change in resonance frequency (Δf) was recorded ($\Delta f_{n=3}/n$ where n is the overtone number corresponding to a 5 MHz AT-cut piezoelectric crystal).

In Vitro Experiments

Cell culture. Hep G2, BT-474, MCF7, SK-BR-3, MDA-MB-231, MDA-MB-468, and A549 cells were obtained from ATCC. A549/Luc and MDA-MB-468/Luc cells were obtained from Cell Biolabs. Cells were subcultured in the supplier's recommended basal medium in a 5% CO_2 humidified atmosphere. All experiments were performed on cells passaged 12-24 h prior.

pH-dependent cellular delivery. Cells were passaged onto 12- or 96-well plates and incubated with 0.17 nM nanoparticle-spiked PBS (Ca^{2+}/Mg^{2+}) of appropriate pH for 3 h. Cell monolayers were washed with PBS, dissociated in 0.25% trypsin-EDTA, and redispersed in PBS containing 1% BSA prior to analysis using a BD LSR II flow cytometer (488 nm ex; 530/30 nm em).

Tumor spheroids. 3D tumor spheroids were prepared as described previously.[55] Briefly, cells were passaged onto 96-well round-bottom ultra-low attachment plates (Corning). After 48-72 h, cell spheroids were transferred onto 18 mm glass coverslips coated with Matrigel GFR (BD) and cell media was supplanted with 50 μL·mL^{-1} of Matrigel GFR. Growth media was removed after

48 h and tumor spheroids were washed with PBS (Ca^{2+}/Mg^{2+}) of appropriate pH and incubated for 3 h in PBS containing 0.17 nM nM LbL nanoparticles. Following incubation, cells were rinsed with PBS, fixed in freshly-prepared 3.7% formaldehyde (PBS, pH 7.4) for 15 min at RT, and permeablized with 0.1% Triton X-100 (PBS) for 5 min at RT. Coverslips were stained using PBS containing 0.66 μM Alexa Fluor 568 phalloidin (Life Technologies), 4 drops mL^{-1} NucBlue (DAPI; Life Technologies), and 1% BSA for 30 min at RT, then rinsed with PBS prior to mounting with Fluoromount (Sigma) onto no. 0 glass-bottom 35 mm MatTek dishes and imaging using a Nikon 1AR Ultra-Fast Spectral Scanning Confocal Microscope.

CD44-dependent cellular delivery. Cells were transfected with siRNA against human CD44 (SI00299705 FlexiTube siRNA Premix, Quiagen) for 72 h at 25 nM, after which cell monolayers (ca. 5×10^5 cells) were incubated with 0.17 nM nanoparticle-spiked PBS (Ca^{2+}/Mg^{2+}) for 3 h, washed with PBS, dissociated in 0.2% EDTA (PBS), pelleted, and labeled with 20 μL of FITC-anti-human CD44 (clone MEM-85; Life Technologies) for 30 min at 4 °C. Cells were recovered by centrifugation (5 min, 600 rcf), fixed in 500 uL of freshly prepared 3.7% paraformaldehyde, and analyzed using a BD LSR II flow cytometer (anti-CD44-FITC: 488 nm ex; 530/30 nm em; nanoparticles: 561 nm ex; 610/20 nm em).

Cell viability. Cells were passaged onto 96-well plates and incubated with nanoparticle-spiked basal medium for 24 h. Cellular ATP was quantified using CellTiter Glo (Promega).

Migration and invasion. Scratch-migration assays were performed on confluent 12-well plates using 0.17 nM nanoparticle-spiked complete basal medium and a 1 mL pipette tip. Cell monolayers were monitored using a 5x inverted objective Olympus optical microscope.

Collagen-transwell invasion was assessed at the concentrations indicated using a 96-well Boyden chamber (8 μm pores) and complete basal medium as a chemoattractant (CHEMICON Cell Invasion kit). Transwell invasion was quantified after 48 h using CelTiter Glo.

In Vivo Experiments

5×10^6 A549, MDA-MB-468, or MDA-MB-468/Luc cells (1:1 PBS:Matrigel) were injected subcutaneously into the hindflanks of nude mice (NCR nu/nu, Taconic). Tumors were allowed to form for 2-3 weeks. Nanoparticles (8.3×10^{12} NP·kg^{-1}, 5% glucose) were injected via the tail vein into tumor-bearing nude or immunocompetent mice (BALB/c, Taconic). Tumors were harvested after 48 or 72 h and processed by the Swanson Biotechnology Histology Core Facility. Briefly, tumors were formalin-fixed, paraffin-embedded, sectioned (5 μm), deparaffinized, antigen retrieved, and stained using DAPI, biotinylated hyaluronic acid binding protein (Calbiochem), anti-CD44-FITC (Life Technologies), and streptavidin-Alexa Fluor 546 (Life Technologies) or DAPI and anti-HIF1α-fluorescein (R&D Systems). Slides were mounted and imaged using a Nikon 1AR Ultra-Fast Spectral Scanning Confocal Microscope. Whole-animal imaging was performed using a Xenogen IVIS Imaging System (Caliper) with D-luciferin (150 mg kg^{-1} i.p., PerkinElmer) as a bioluminescent substrate. These experiments were approved by the Massachusetts Institute of Technology Committee on Animal Care (CAC).

FIGURES

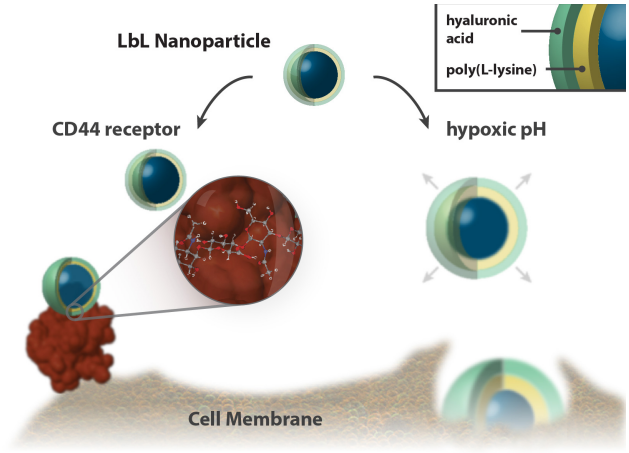

Figure 1. Hyaluronan Layer-by-Layer (LbL) nanoparticles actively target tumor hypoxia and cancer stem cell receptor CD44. Protein structure was rendered from biological assembly 1 of PDB ID 1UUH.

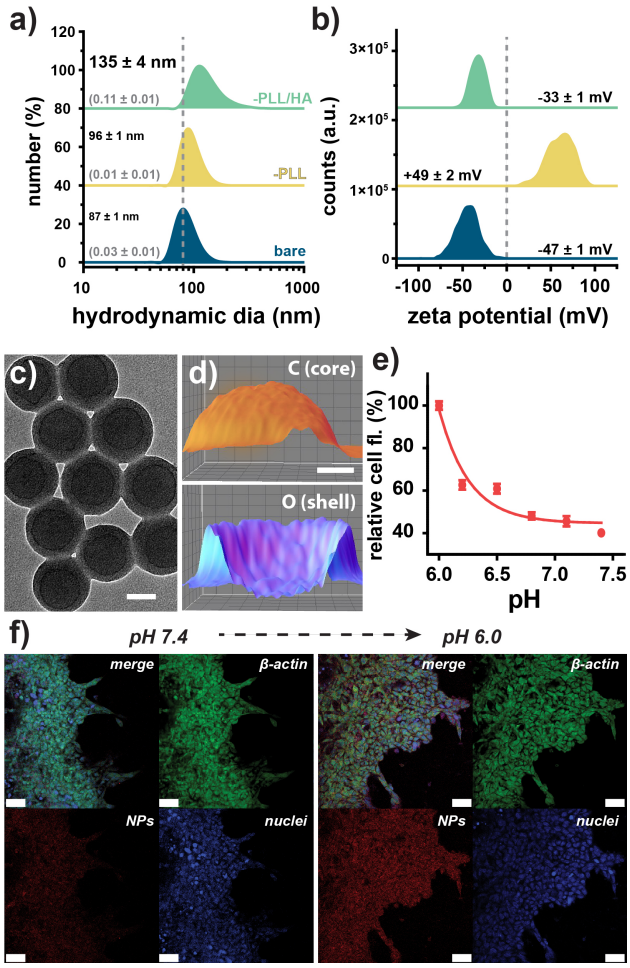

Figure 2. pH-responsive hyaluronan-LbL nanoparticles target hypoxic tumor pH *in vitro*. a) Increase in hydrodynamic size and (b) concomitant shift in surface charge during LbL assembly onto mock fluorescent drug carriers as measured by photon correlation spectroscopy and laser Doppler electrophoresis, respectively. c) Transmission electron microscopy (TEM) of the subsequent hyaluronan-LbL nanoparticle assemblies and (d) a cross-sectional elemental mapping reconstruction of an individual LbL nanoparticle as imaged by energy-filtered TEM (EFTEM). e) pH-dependent cellular delivery of hyaluronan-LbL nanoparticles to Hep G2 hepatocyte cells as measured by flow cytometry (t=3 h). f) Confocal fluorescence micrographs of hypoxic pH-augmented cellular delivery of hyaluronan-LbL nanoparticles (red) to 3D Hep G2 tumor spheroids. Measurements in (a,b) were obtained in deionized water. Values in parentheses in (a) represent polydispersity index. Error bars represent SD of three technical replicates. Scale bar is (c) 50 nm, (d) 20 nm, and (f) 20 μm.

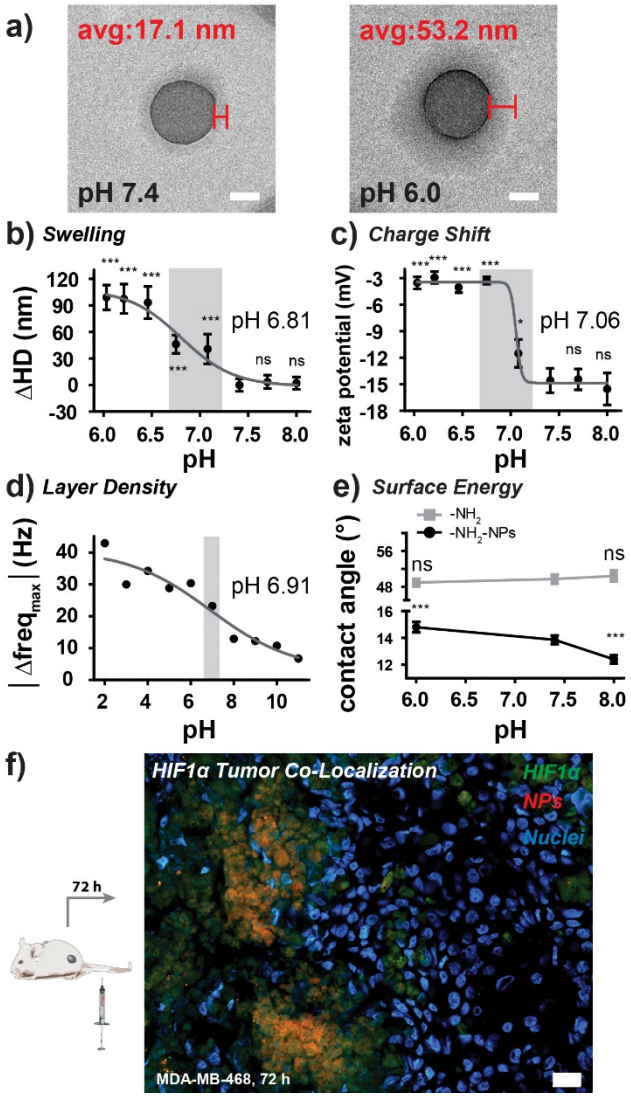

Figure 3. Hypoxic pH-induced structural reorganization of hyaluronan-LbL nanoparticles and *in vivo* hypoxic tumor-targeting. a) Low electron-dose TEM illustrating pH-dependent LbL bilayer swelling. b) pH-dependent hydrodynamic swelling and (c) loss of stabilizing surface charge as

measured by photon correlation spectroscopy and laser Doppler electrophoresis, respectively. d) Quartz crystal microbalance dissipation (QCM-D) tracking of pH-dependent hyaluronan adsorption onto amine-modified Au. e) Contact angle measurements of substrate-immobilized hyaluronan-LbL nanoparticles demonstrating hypoxic pH-dependent decreased surface energy at hypoxic pH. f) *In vivo* tumor co-localization of hyaluronan-LbL nanoparticles (red) with hypoxia-inducible factor 1 α (HIF1α, green) in subcutaneous triple-negative breast carcinoma tumor xenografts (i.v.). Measurements in (b,c) were obtained in phosphate buffered saline. Nominal hypoxic tumor pH ranges are shaded in (b-d). Error represents SD of three technical replicates. Scale bar is (a) 50 nm and (f) 10 μm.

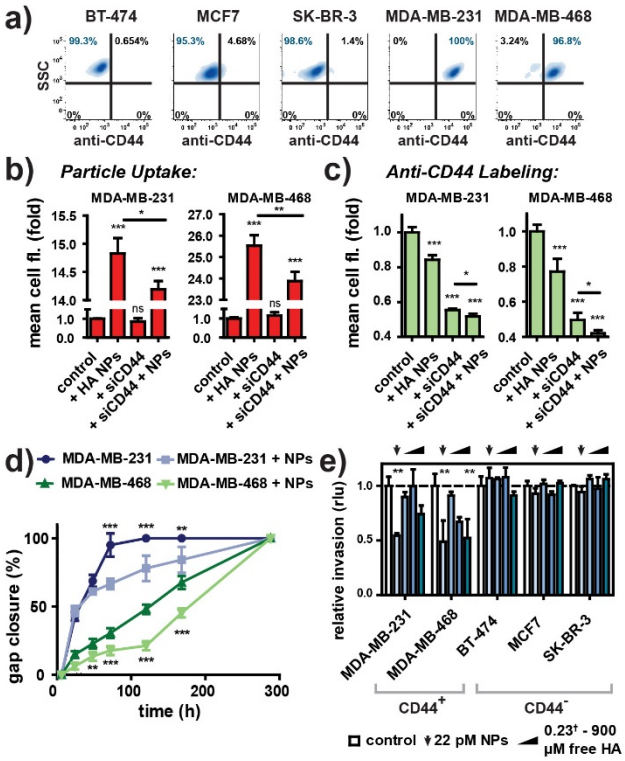

Figure 4. Hyaluronan-LbL nanoparticles target cancer stem cell receptor CD44 and selectively decrease *in vitro* migration/invasion. a) CD44 receptor expression in panel of breast carcinoma cells, as measured by antibody-labeling and flow cytometry. b) CD44-specific nanoparticle delivery is decreased following receptor knockdown triple-negative breast carcinoma cells as measured by flow cytometry. c) Hyaluronan-LbL nanoparticles and CD44 antibodies competitively bind cell-surface receptor CD44 in MDA-MB-231 and -468 breast carcinoma cells as measured by flow cytometry. d) Dual-targeting hyaluronan-LbL nanoparticles diminish both 2D cell migration and (e) 3D collagen gel transwell invasion in a CD44 receptor-selective manner (Fig. S3,4). Error represents SD of (b-d) three technical and (e) three biological replicates.† in (e) denotes LbL assembly buffer-equivalent concentrations of HA.

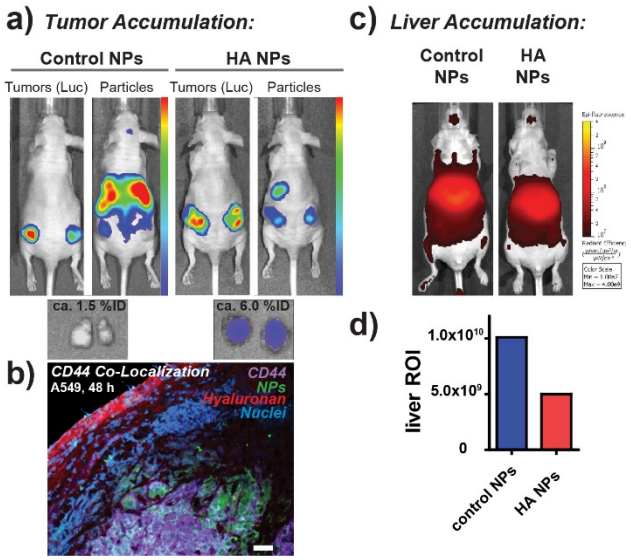

Figure 5. Polysaccharide-LbL nanoparticles target tumors *in vivo*. a) Tumor co-localization from hyaluronan-LbL nanoparticles compared with dextran sulfate-conjugated control nanoparticles, as imaged by whole-animal bioluminescence/fluorescence imaging (MDA-MB-468/Luc, 72 h). Inset: *ex vivo* analysis of integrated tumor-associated fluorescence. b) Co-localization of hyaluronan-LbL nanoparticles (green) with CD44 receptor (violet) in histological sections from A549 tumor xenografts following i.v. injection in tumor-bearing mice (48 h). c) Accumulation of hyaluronan-LbL nanoparticles and dextran sulfate control nanoparticles in the livers of immunocompetent (non-tumor bearing) mice following i.v. injection (48 h) as imaged by whole animal fluorescence. d) Region-of-interesting analysis of liver-specific accumulation in (c).Scale bar in (b) is 50 μm.

ASSOCIATED CONTENT

Supporting Information. Comparative nonspecific and hypoxic-pH specific cell delivery, nanoparticle penetration into 3D tumor spheroids, dose-dependent cell viability, and time-dependent 2D cell migration of CD44 negative breast carcinoma cells. This material is available free of charge via the Internet at http://pubs.acs.org.

AUTHOR INFORMATION

Corresponding Author

*hammond@mit.edu

ACKNOWLEDGMENT

The authors acknowledge generous support from Janssen Pharmaceuticals, Inc., the TRANSCEND partnership, and fellowship support from the NIH (ECD, Kirschstein NRSA 1F32EB017614-01), NSF (SWM), NSERC (KES, NSERC-PDF), and NHMRC (ZJD). This work was supported in part by the Koch Institute Support (core) Grant P30-CA14051 from the NCI, the MIT MRSEC Grant DMR-0819762 from the NSF, the National Research Foundation (NRF-NRFF2011-01), and technical assistance from the MIT Department of Comparative Medicine, Koch Institute Swanson Biotechnology Center, specifically the FACS, Peterson Nanotechnology core, ATWAI, and Tang Histology facilities. The authors are grateful to Officer Sean Collier for his caring service to the MIT community and for his sacrifice.

REFERENCES

1. Eliasof, S.; Lazarus, D.; Peters, C.; Case, R.; Cole, R.; Hwang, J.; Schluep, T.; Chao, J.; Lin, J.; Yen, Y.; Han, H.; Wiley, D.; Zuckerman, J.; Davis, M. Correlating preclinical animal studies

and human clinical trials of a multifunctional, polymeric nanoparticle. *Proc. Natl. Acad. Sci. U.S.A.* 2013, 110, 15127-15132.

2. Akinc, A.; Zumbuehl, A.; Goldberg, M.; Leshchiner, E. S.; Busini, V.; Hossain, N.; Bacallado, S. A.; Nguyen, D. N.; Fuller, J.; Alvarez, R.; Borodovsky, A.; Borland, T.; Constien, R.; de Fougerolles, A.; Dorkin, J. R.; Narayanannair Jayaprakash, K.; Jayaraman, M.; John, M.; Koteliansky, V.; Manoharan, M.; Nechev, L.; Qin, J.; Racie, T.; Raitcheva, D.; Rajeev, K. G.; Sah, D. W. Y.; Soutschek, J.; Toudjarska, I.; Vornlocher, H.-P.; Zimmermann, T. S.; Langer, R.; Anderson, D. G. A combinatorial library of lipid-like materials for delivery of RNAi therapeutics. *Nat. Biotech.* 2008, 26, 561-569.

3. Matsumura, Y.; Maeda, H. A New Concept for Macromolecular Therapeutics in Cancer Chemotherapy: Mechanism of Tumoritropic Accumulation of Proteins and the Antitumor Agent Smancs. *Cancer Res.* 1986, 46, 6387-6392.

4. Jain, R. K. Transport of Molecules in the Tumor Interstitium: A Review. *Cancer Res.* 1987, 47, 3039-3051.

5. Choi, C. H. J.; Alabi, C. A.; Webster, P.; Davis, M. E. Mechanism of active targeting in solid tumors with transferrin-containing gold nanoparticles. *Proc. Nat. Acad. Sci. U.S.A.* 2010, 107, 1235-1240.

6. Wong, C.; Stylianopoulos, T.; Cui, J.; Martin, J.; Chauhan, V. P.; Jiang, W.; Popović, Z.; Jain, R. K.; Bawendi, M. G.; Fukumura, D. Multistage nanoparticle delivery system for deep penetration into tumor tissue. *Proc. Natl. Acad. Sci. U.S.A.* 2011, 108, 2426-2431.

7. Vogelstein, B.; Papadopoulos, N.; Velculescu, V. E.; Zhou, S.; Diaz, L. A.; Kinzler, K. W. Cancer Genome Landscapes. *Science* 2013, 339, 1546-1558.

8. Marusyk, A.; Almendro, V.; Polyak, K. Intra-tumour heterogeneity: a looking glass for cancer? *Nat. Rev. Cancer* 2012, 12, 323-334.

9. Greaves, M.; Maley, C. C. Clonal evolution in cancer. *Nature* 2012, 481, 306-313.

10. Park, S. Y.; xF; nen, M.; Kim, H. J.; Michor, F.; Polyak, K. Cellular and genetic diversity in the progression of in situ human breast carcinomas to an invasive phenotype. *J. Clin. Invest.* 2010, 120, 636-644.

11. Maley, C. C.; Galipeau, P. C.; Finley, J. C.; Wongsurawat, V. J.; Li, X.; Sanchez, C. A.; Paulson, T. G.; Blount, P. L.; Risques, R.-A.; Rabinovitch, P. S.; Reid, B. J. Genetic clonal diversity predicts progression to esophageal adenocarcinoma. *Nat. Genet.* 2006, 38, 468-473.

12. Bedard, P. L.; Hansen, A. R.; Ratain, M. J.; Siu, L. L. Tumour heterogeneity in the clinic. *Nature* 2013, 501, 355-364.

13. Caruso, F.; Caruso, R. A.; Mohwald, H. Nanoengineering of inorganic and hybrid hollow spheres by colloidal templating. *Science* 1998, 282, 1111-1114.

14. Donath, E.; Sukhorukov, G. B.; Caruso, F.; Davis, S. A.; Möhwald, H. Novel hollow polymer shells by colloid templated assembly of polyelectrolytes. *Angew. Chem. Int. Ed.* 1998, 37, 2201-2205.

15. Shutava, T. G.; Balkundi, S. S.; Vangala, P.; Steffan, J. J.; Bigelow, R. L.; Cardelli, J. A.; O'Neal, D. P.; Lvov, Y. M. Layer-by-Layer-Coated Gelatin Nanoparticles as a Vehicle for Delivery of Natural Polyphenols. *ACS Nano* 2009, 3, 1877-1885.

16. Schneider, G.; Decher, G. From functional core/shell nanoparticles prepared via layer-by-layer deposition to empty nanospheres. *Nano Lett*. 2004.

17. Zahr, A.; de Villiers, M.; Pishko, M. Encapsulation of drug nanoparticles in self-assembled macromolecular nanoshells. *Langmuir* 2005, 21, 403-410.

18. Agarwal, A.; Lvov, Y.; Sawant, R.; Torchilin, V. Stable nanocolloids of poorly soluble drugs with high drug content prepared using the combination of sonication and layer-by-layer technology. *J. Controlled Release* 2008, 128, 255-260.

19. Poon, Z.; Chang, D.; Zhao, X.; Hammond, P. T. Layer-by-Layer Nanoparticles with a pH-Sheddable Layer for in Vivo Targeting of Tumor Hypoxia. *ACS Nano* 2011, 5, 4284-4292.

20. Poon, Z.; Lee, J. B.; Morton, S. W.; Hammond, P. T. Controlling in Vivo Stability and Biodistribution in Electrostatically Assembled Nanoparticles for Systemic Delivery. *Nano Lett*. 2011, 11, 2096-2103.

21. Hammond, P. T. Polyelectrolyte multilayered nanoparticles: using nanolayers for controlled and targeted systemic release. *Nanomedicine* 2012, 7, 619-622.

22. Morton, S.; Herlihy, K.; Shopsowitz, K.; Deng, Z.; Chu, K.; Bowerman, C.; Desimone, J.; Hammond, P. Scalable manufacture of built-to-order nanomedicine: spray-assisted layer-by-layer functionalization of PRINT nanoparticles. *Adv. Mater*. 2013, 25, 4707-4713.

23. Morton, S.; Poon, Z.; Hammond, P. The architecture and biological performance of drug-loaded LbL nanoparticles. *Biomaterials* 2013, 34, 5328-5335.

24. Sukhishvili, S. A. Responsive polymer films and capsules via layer-by-layer assembly. *Curr. Opin. Colloid Interface Sci.* 2005, 10.

25. Luo, R.; Neu, B.; Venkatraman, S. Surface functionalization of nanoparticles to control cell interactions and drug release. *Small* 2012, 8, 2585-2594.

26. Deng, Z. J.; Morton, S. W.; Ben-Akiva, E.; Dreaden, E. C.; Shopsowitz, K. E.; Hammond, P. T. Layer-by-Layer Nanoparticles for Systemic Codelivery of an Anticancer Drug and siRNA for Potential Triple-Negative Breast Cancer Treatment. *ACS Nano* 2013, 7, 9571-9584.

27. Morton, S. W.; Shah, N. J.; Quadir, M. A.; Deng, Z. J.; Poon, Z.; Hammond, P. T. Osteotropic Therapy via Targeted Layer-by-Layer Nanoparticles. *Adv. Healthc. Mater.* 2013, ASAP.

28. Lee, J. B.; Hong, J.; Bonner, D. K.; Poon, Z.; Hammond, P. T. Self-assembled RNA interference microsponges for efficient siRNA delivery. *Nat. Mater.* 2012, 11, 316-322.

29. Ye, C.; Drachuk, I.; Calabrese, R.; Dai, H.; Kaplan, D.; Tsukruk, V. Permeability and micromechanical properties of silk ionomer microcapsules. *Langmuir* 2012, 28, 12235-12244.

30. Tan, Y.; Mundargi, R.; Chen, M.; Lessig, J.; Neu, B.; Venkatraman, S.; Wong, T. Layer-by-Layer Nanoparticles as an Efficient siRNA Delivery Vehicle for SPARC Silencing. *Small (in press)* 2014.

31. Caruso, F.; Spasova, M.; Susha, A.; Giersig, M.; Caruso, R. A. Magnetic nanocomposite particles and hollow spheres constructed by a sequential layering approach. *Chem. Mater.* 2001, 13, 109-116.

32. Mendelsohn, J.; Barrett, C.; Chan, V.; Pal, A.; Mayes, A.; Rubner, M. Fabrication of microporous thin films from polyelectrolyte multilayers. *Langmuir* 2000, 16, 5017-5023.

33. Harris, J. J.; Bruening, M. L. Electrochemical and in situ ellipsometric investigation of the permeability and stability of layered polyelectrolyte films. *Langmuir* 2000, 16, 2006-2013.

34. Petrov, A. I.; Antipov, A. A.; Sukhorukov, G. B. Base-acid equilibria in polyelectrolyte systems: from weak polyelectrolytes to interpolyelectrolyte complexes and multilayered polyelectrolyte shells. *Macromolecules* 2003, 36, 10079-10086.

35. Jain, R. K.; Stylianopoulos, T. Delivering nanomedicine to solid tumors. *Nat. Rev. Clin. Oncol.* 2010, 7, 653-664.

36. De Bock, K.; Mazzone, M.; Carmeliet, P. Antiangiogenic therapy, hypoxia, and metastasis: risky liaisons, or not? *Nat. Rev. Clin. Oncol.* 2011, 8, 393-404.

37. Hashimoto, D.; Hirota, M.; Yagi, Y.; Baba, H. Hyaluronate carboxymethylcellulose-based bioresorbable membrane (Seprafilm) reduces adhesion under the incision to make unplanned re-laparotomy safer. *Surg. Today* 2012, 42, 863-867.

38. Al-Hajj, M.; Wicha, M.; Benito-Hernandez, A.; Morrison, S.; Clarke, M. Prospective identification of tumorigenic breast cancer cells. *Proc. Natl. Acad. Sci. U.S.A.* 2003, 100, 3983-3988.

39. Alvero, A. B.; Chen, R.; Fu, H.-H.; Montagna, M.; Schwartz, P. E.; Rutherford, T.; Silasi, D.-A.; Steffensen, K. D.; Waldstrom, M.; Visintin, I.; Mor, G. Molecular phenotyping of human ovarian cancer stem cells unravels the mechanisms for repair and chemoresistance. *Cell Cycle* 2009, 8, 158-166.

40. Zhang, S.; Balch, C.; Chan, M. W.; Lai, H.-C.; Matei, D.; Schilder, J. M.; Yan, P. S.; Huang, T. H.-M.; Nephew, K. P. Identification and Characterization of Ovarian Cancer-Initiating Cells from Primary Human Tumors. *Cancer Res*. 2008, 68, 4311-4320.

41. Ricardo, S.; Vieira, A.; Gerhard, R.; Leitão, D.; Pinto, R.; Cameselle-Teijeiro, J.; Milanezi, F.; Schmitt, F.; Paredes, J. Breast cancer stem cell markers CD44, CD24 and ALDH1: expression distribution within intrinsic molecular subtype. *J. Clin. Pathol*. 2011, 64, 937-946.

42. Choi, K.; Yoon, H.; Kim, J.-H.; Bae, S.; Park, R.-W.; Kang, Y.; Kim, I.-S.; Kwon, I.; Choi, K.; Jeong, S.; Kim, K.; Park, J. Smart nanocarrier based on PEGylated hyaluronic acid for cancer therapy. *ACS Nano* 2011, 5, 8591-8599.

43. Ganesh, S.; Iyer, A.; Gattacceca, F.; Morrissey, D.; Amiji, M. In vivo biodistribution of siRNA and cisplatin administered using CD44-targeted hyaluronic acid nanoparticles. *J. Controlled Release* 2013, 172, 699-706.

44. Cohen, K.; Emmanuel, R.; Kisin-Finfer, E.; Shabat, D.; Peer, D. Modulation of drug resistance in ovarian adenocarcinoma using chemotherapy entrapped in hyaluronan-grafted nanoparticle clusters. *ACS Nano* 2014, 8, 2183-2195.

45. Bauer, S.; Arpa-Sancet, M.; Finlay, J.; Callow, M.; Callow, J.; Rosenhahn, A. Adhesion of marine fouling organisms on hydrophilic and amphiphilic polysaccharides. *Langmuir* 2013, 29, 4039-4047.

46. Mueller, M.; Fusenig, N. Friends or foes - bipolar effects of the tumour stroma in cancer. *Nat. Rev. Cancer* 2004, 4, 839-849.

47. Shiratori, S. S.; Rubner, M. F. pH-Dependent Thickness Behavior of Sequentially Adsorbed Layers of Weak Polyelectrolytes. *Macromolecules* 2000, 33.

48. Burke, S.; Barrett, C. pH-responsive properties of multilayered poly(L-lysine)/hyaluronic acid surfaces. *Biomacromol.* 2003, 4, 1773-1783.

49. Burke, S. E.; Barrett, C. J. Swelling Behavior of Hyaluronic Acid/Polyallylamine Hydrochloride Multilayer Films. *Biomacromol.* 2005, 6, 1419-1428.

50. Nel, A. E.; Mädler, L.; Velegol, D.; Xia, T.; Hoek, E. M. V.; Somasundaran, P.; Klaessig, F.; Castranova, V.; Thompson, M. Understanding biophysicochemical interactions at the nano-bio interface. *Nat. Mater.* 2009, 8, 543-557.

51. Wilson, W.; Hay, M. Targeting hypoxia in cancer therapy. *Nat. Rev. Cancer* 2011, 11, 393-410.

52. Olaku, V.; Matzke, A.; Mitchell, C.; Hasenauer, S.; Sakkaravarthi, A.; Pace, G.; Ponta, H.; Orian-Rousseau, V. c-Met recruits ICAM-1 as a coreceptor to compensate for the loss of CD44 in Cd44 null mice. *Mol. Biol. Cell* 2011, 22, 2777-2786.

53. Zöller, M. CD44: can a cancer-initiating cell profit from an abundantly expressed molecule? *Nat. Rev. Cancer* 2011, 11, 254-267.

54. Cho, N.-J.; Frank, C.; Kasemo, B.; Höök, F. Quartz crystal microbalance with dissipation monitoring of supported lipid bilayers on various substrates. *Nat. Protoc.* 2010, 5, 1096-1106.

55. Vinci, M.; Gowan, S.; Boxall, F.; Patterson, L.; Zimmermann, M.; Court, W.; Lomas, C.; Mendiola, M.; Hardisson, D.; Eccles, S. Advances in establishment and analysis of three-dimensional tumor spheroid-based functional assays for target validation and drug evaluation. *BMC Biol.* 2012, 10, 29.

TABLE OF CONTENTS IMAGE